UNIVERSITY OF SALERNO

DOCTORAL THESIS

Rate of Radiative and Non-Radiative Processes in Electro-Optical Devices: a Theoretical Study

---

Author:
Dr. Anna LEO

Supervisor:
Prof. Andrea PELUSO

February 3, 2026

"Science cannot tell us a word about why music delights us, of why and how an old song can move us to tears."

Erwin Schrödinger

UNIVERSITY OF SALERNO

Abstract

Department or Chemistry and Biology

Doctor of Philosophy

Rate of Radiative and Non-Radiative Processes in Electro-Optical Devices: a Theoretical Study

by Dr. Anna LEO

Organic materials for optoelectronic applications are at the forefront of current scientific research, offering promising alternatives to traditional inorganic semiconductors. Because of their eco-friendliness, ease of fabrication, and broad chemical tunability make them attractive candidates; however, challenges such as limited stability, low efficiencies, and environmental sensitivity continue to limit their performance. Addressing these challenges requires a detailed understanding of the relationships between molecular structure, optoelectronic properties, and device performance.

Theoretical approaches provide a powerful route to this understanding by enabling the rational design of molecules and polymers prior to synthesis. In this thesis, a novel and accurate theoretical approach for treating internal conversion is introduced, combining computational tractability with physical rigor. This model allows quantitative predictions of the rate constants

of elementary radiative and non-radiative electronic transitions which take place in modern optoelectronic devices, allowing for analysing competitive de-excitation pathways, which could affect device efficiencies.

The predictive capability of this approach facilitates the design of materials with tailored photophysical and electronic properties. This is particularly relevant for next-generation optoelectronic devices, including OLEDs with improved quantum yields, organic solar cells with minimized recombination losses, and flexible or large-area molecular electronics. By linking theoretical insights directly to material optimization, this work provides a framework for the accelerated discovery and development of organic materials that combine efficiency, stability, and tunability in advanced optoelectronic technologies.

Acknowledgements

I would like to thank Professor Andrea Peluso for his trust, patience and constant encouragement. Thanks above all to his pure and free way of doing science which is for me an example and a source of admiration. Financial support of University of Salerno is gratefully acknowledged.

Contents

Abstract **v**

Acknowledgements **vii**

Introduction **3**

1 Calculation of Radiative and Non-Radiative Rate Constants from First Principles **11**

1.1 Vibronic states 12

1.2 Normal modes of vibrations 21

1.2.1 Time evolution of quantum states 25

1.3 The Generating Function Approach 29

1.3.1 Electronic coupling independent of nuclear coordinates 37

1.3.2 The case of non-adiabatic coupling terms 39

2 Electron Transfer Reactions **45**

2.1 Marcus' theory of ET 47

2.2 Quantum effects in classical ET theory 52

2.3 ET beyond Marcus theory: full quantum model . 55

2.4 Intramolecular ET in rigdly bridged donor-acceptor systems 62

2.4.1 Implicit modeling of solvent reorganization energy 73

3 Environmental Reorganization in Organic Materials 77
3.1 Theoretical formulation 79
3.2 THF solution with Naphthalene 84
3.2.1 Structural properties of THF 85
3.2.2 Electronic structure and energy level alignment 87
3.2.3 Redox potentials and solvent reorganization energy 90
3.3 Reorganization and disorder: linking solution and solid-state charge dynamics 98

4 Characterization of Excited-State Relaxation via IC and ISC 105
4.1 The photophysics of azulene 106
4.2 Intersystem crossing of xanthone 113

5 Computational Details 123
5.1 Computational details for Chapter 3 and Chapter 5 123
5.2 Computational details for Chapter 4 124

6 Concluding Remark 127

A First Order Time Dependent Perturbation Theory (TDPT) 131

B Gaussian Integrals 137

C Numerical calculation of $F(\Delta E, T)$ **143**

Bibliography **147**

To my sweet little daughters M. and G.

Introduction

Over the past fifty years, π-conjugated molecular systems have revolutionized the field of organic electronics. Their unique electronic structure, featuring delocalized π-electrons along conjugated backbones, enables efficient charge transport and tunable optical absorption and emission, making them ideally suited for flexible, lightweight, and cost-effective electronic devices.[45, 149, 115, 77, 86, 96, 84, 122, 116] Their favorable properties, among which the ease of fabrication, the chemical and structural versatility, and the mechanical flexibility, have made them attractive for a wide range of applications, as organic light-emitting diodes (OLEDs)[135, 176], which are now the essential components of high-efficiency color displays, organic field-effect transistors (OFETs)[133, 175], and low-cost, high-performance organic solar cells (OSCs).[173, 49]

While inorganic devices, such as silicon-based solar cells, transistors and LEDs, offer superior efficiency and stability, they typically require rigid substrates and complex fabrication processes. In contrast, π-conjugated materials are characterized by mechanical flexibility, lightweight construction, and compatibility with solution-based processing, making them unique for appealing applications, such as flexible displays, wearable electronics, and large-area OSCs.

Despite these advantages, π-conjugated devices face intrinsic challenges related to stability, charge mobility, and environmental sensitivity. Organic semiconductors generally exhibit lower charge mobilities compared to their inorganic counterparts,[174, 97] as their molecular and polymer building blocks interact primarily through non covalent forces,[155] which are significantly weaker than the covalent or ionic bonds found in inorganic materials. Consequently, the development of new organic materials with improved properties remains a central challenge in the field of organic electronics.

One of the great advantage which characterize molecular electronics is the possibility it offers of finely tuning molecular properties by acting on the chemical structures of the components, providing precise control over their electronic and optical properties.[26, 112] In this context, theoretical modeling has become an indispensable tool in this design process, enabling the prediction of device performance prior to synthesis. Methods such as density functional theory (DFT), time-dependent DFT (TD-DFT), and molecular dynamics (MD) simulations are widely applied to understand how molecular structure influences optical spectra, charge distribution, and packing morphology. These computational approaches guide the rational selection of donor–acceptor units, conjugation length, and substituents, significantly reducing trial-and-error experimentation. The integration of experimental studies with theoretical modeling has accelerated the development of high-performance optoelectronic devices and underscores the indispensable role

of computational studies in linking molecular design to technological application. For example, tailoring energy levels and molecular packing has yielded OLEDs with enhanced efficiency and operational stability, while optimizing donor-acceptor interfaces in OSCs has led to notable improvements in power conversion efficiency. Continued progress in computation and characterization is expected to further refine the rational design of π-conjugated materials, deepening our understanding and enabling next-generation optoelectronic technologies.

Although theoretical design has played an important role in the development of organic electronics, there are still aspects that have been largely overlooked. Indeed, most of the research efforts have been focused on the prediction of static electronic properties, neglecting the kinetics of all the elementary processes which take place in a technological device. Kinetic aspects are instead of paramount importance because often they determine the efficiency of the optoelectronic devices.

The need of incorporating kinetic aspects in the design and optimization of new chromophores is related to the fact that in an optoelectronic devices several competitive processes, both beneficial and detrimental, can occur. Upon photon absorption, an electron is promoted from one of the filled molecular orbital to an empty one generating an excited electronic state (S_n). This excited state rapidly relaxes through vibrational relaxation and internal conversion, reaching the lowest vibrational level of the first excited singlet state (S_1). From here, several deactivation pathways can occur:(i) the system can return to the ground state via the emission of a photon, a process known as a radiative

transition (fluorescence), (ii) it can return to the ground state dissipating the excitation energy non-radiatively, through internal conversion or vibrational relaxation, without photon emission, or (iii) it can transform into an excited state of triplet T_n through intersystem crossing and then return to the ground state via comparatively slower radiative (phosphorescence) or non radiative (intersystem crossing) processes. The T_n state has a longer lifetime compared to the singlet one because the transition to S_0 is spin forbidden. This longer lifetime can be important in some devices for allowing the system to evolve towards the desired direction.

The hierarchy of these transitions is summarized in the Jablonski diagram (Figure 1), where horizontal lines represent electronic and vibrational energy levels. Thicker lines correspond to electronic states, while thinner lines depict vibrational sublevels. Radiative transitions (fluorescence and phosphorescence) are shown with straight arrows, whereas curved arrows denote non-radiative processes such as internal conversion or intersystem crossing. Absorption is among the most rapid events and involves the lowest vibrational level of S_0 due to the Boltzmann distribution of molecules in that level at ordinary temperature.[65] The transition leads to a vibrationally excited level of an electronic excited state S_n determined by the Franck-Condon principle.[66] From here non radiative transitions, as internal conversion, are generally kinetically predominant, allowing to reach the lowest excited state S_1 in short time scales, from 10^{-14} to 10^{-11}s. S_1 can then decay via competitive pathways: S_1 can decay to S_0 by fluorescence within 10^{-9} to 10^{-7}s, or transform

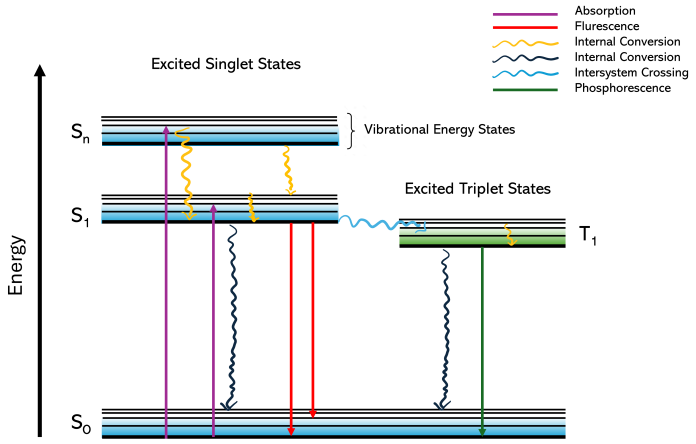

FIGURE 1: Jablonski energy diagram of electronic and vibrational energy levels of an excited molecule

in T_n by intersystem crossing, a process which take place in comparatively longer times, from 10^{-8} to 10^{-3}s. From T_n the system can reach T_1 via IC and returns to S_0 by phosphorescence on a time scale ranging from 10^{-4} to 10s.[126]

Because the relative rates of those elementary processes ultimately dictate device efficiency, kinetic aspects cannot be disregarded in the theoretical design and material optimization. In this thesis, time-dependent perturbation theory is used to develop methodologies and computational tools for evaluating kinetic constants associated with radiative and non-radiative transitions of elementary processes. The approach has been validated by comparing theoretical results with experimental time-resolved spectroscopic measurements for several selected prototypical molecular cases. The approach proposed and developed

here offers some advantages with respect to other methodologies, mainly based on the numerical solution of the time dependent Schrödinger equation, and of course some disadvantages.

The main advantage of the adopted physical approach is that it allows to include in computations the whole set of intramolecular degrees of freedom of the molecular systems, without posing limits to the number of basis function to be used in dynamical calculations. That is a key point because it is well know that the obtainment of reliable kinetic data requires the use of hugely large basis sets. The price one has to pay is the neglect of coherence effects, which usually lead to overestimate rates.

This PhD thesis has been also devoted to a deeper understanding of electron transfer reactions, both because they are ubiquitous in optoelctronic devices and because of their inherent importance in Chemistry. Among the theoretical approaches devoted to electron transfer, Marcus' theory is certainly among the most influential one. Originally formulated to describe electron transfer in solution,[105] it was later adapted to solid-state organic semiconductors. By incorporating the reorganization energy associated with nuclear relaxation during charge transfer, Marcus theory explains the rate dependence of charge mobility on the balance between activation energy and driving force. Although recent works have demonstrated its predictive power in describing transport in organic crystals and disordered systems,[142, 143, 12] Marcus' theory is a classical theory which suffers from the lack of important quantum mechanical effects like tunnelling.

Tunnelling effects are expected to be extremely important in optoelectronic devices, especially in charge transport processes. In this thesis an original generalization of Marcus' theory which allows for introducing tunnelling effects in the framework of "solvent" activated electron transfer will be discussed. The proposed multistep electron transfer model exploits the distinct time scales of nuclear and solvent motions, offering mechanistic insight into electron transfer phenomena. The model not only reproduces experimental observables but also uncovers novel mechanistic aspects that allow an advance in understanding of photochemical properties in donor–acceptor systems, providing predictive capabilities inaccessible to conventional models. Importantly, the model achieves these predictions at a relatively low computational cost, avoiding the need for more expensive computational approaches while maintaining high accuracy.

Chapter 1

Calculation of Radiative and Non-Radiative Rate Constants from First Principles

In this chapter the approach adopted in this thesis for evaluating rate constants of radiative and non-radiative processes from first principles electronic-structure calculations will be discussed in some depth. Starting from the factorization of the vibronic wavefunction into a product of electronic and vibrational functions, particular emphasis will be posed on how nuclear motion induces electronic transitions and relaxation processes, determining their rates. The Born-Oppenheimer approximation is introduced as central assumption that enables the solution of the molecular Schrödingher equation, providing the essential foundation for understanding and predicting molecular behavior from first principles. The chapter then examines the limitations of this approximation when non-adiabatic

effects become significant and introduce the vibronic coupling terms, describing their role in promoting transitions between electronic states. The time evolution of quantum states is then introduced for treating dynamical aspects of the different decay pathways, focusing particular attention on the approach based on the time dependent perturbation theory and the generating function method, which allows for reliable calculations of rate constants for both radiative and non-radiative transitions between electronic states, thus providing a connection of paramount importance between theory and experimental observations.

1.1 Vibronic states

Molecular properties can be obtained by resolution of the time-indipendent Schrödinger equation

$$\hat{\mathcal{H}}(\mathbf{q},\mathbf{Q})\Psi(\mathbf{q},\mathbf{Q}) = E\Psi(\mathbf{q},\mathbf{Q}) \tag{1.1}$$

where $\hat{\mathcal{H}}$ is the Hamiltonian operator, defined as the sum of kinetic energy $\hat{T}$ and potential energy $\hat{U}$ operators, $\Psi(\mathbf{q},\mathbf{Q})$ the wavefunction representing state of the system, E the total energy of the system, and $\mathbf{Q}$ and $\mathbf{q}$ denote the sets of nuclear and electronic coordinates, respectively. The molecular Hamiltonian includes the kinetic energy of both electrons, $\hat{T}_{el}$, and nuclei, $\hat{T}_{nu}$, and the potential energy $\hat{U}$ from electron-electron, electron-nucleus and nucleus-nucleus interactions. This is a

many-body problem that can not be solved exactly. To overcome this difficulty, approximations are necessary. By far, the Born-Oppenheimer (BO) approximation is the most important one: it states that, due to the large mass difference between electrons and nuclei and to the fact that both particles experience the same forces, the velocities of electrons are much higher than those of nuclei, with the result that electron motion instantaneously adapt to a change in nuclear positions. That assumption, often referred to as adiabatic separation of nuclear and electronic motions, allows to factorize the total molecular wavefunction $\Psi(\mathbf{q}, \mathbf{Q})$ into a product of an electronic $\phi(\mathbf{q}, \mathbf{Q})$ and nuclear $\chi(\mathbf{Q})$ terms,

$$\Psi(\mathbf{q}, \mathbf{Q}) = \phi(\mathbf{q}, \mathbf{Q})\chi(\mathbf{Q}). \tag{1.2}$$

Here, wavefunction factorization will be presented following the Born and Huang approach,[20] a very lucid procedure which was widely adopted in the past.

First, an electronic Hamiltonian is defined, combining together all the terms which depend on the electronic coordinates:

$$\hat{\mathcal{H}}_{el} = \hat{T}(\mathbf{q}) + \hat{U}(\mathbf{q}, \mathbf{Q}). \tag{1.3}$$

Here the nuclear coordinates are considered as parameters, necessary to define the force field in which electrons move. As usual, nuclear repulsions are also included in $U(\mathbf{q}, \mathbf{Q})$, even

though they do not depend on q. Solution of the time independent Schrödinger equation at fixed nuclei:

$$\hat{\mathcal{H}}_{el}(\mathbf{q},\mathbf{Q})\phi_n(\mathbf{q},\mathbf{Q}) = E_n(\mathbf{Q})\phi_n(\mathbf{q},\mathbf{Q}), \tag{1.4}$$

yields then the electronic wavefunction, which parametrically depend on nuclear coordinates. It is assumed that the Schrödinger equation above can be written and solved for any value of Q coordinates. The set of electronic wavefunctions which are eigenfunctions of $\hat{\mathcal{H}}_{el}$ form a complete set in the space q and can therefore be used to expand the wavefunction of the total Hamiltonian of eq. 1.1:

$$\Psi(\mathbf{q},\mathbf{Q}) = \sum_n \phi_n(\mathbf{q},\mathbf{Q})\chi_{nv}(\mathbf{Q}), \tag{1.5}$$

where $\chi_{nv}(\mathbf{Q})$ are at the moment considered as expansion coefficients. Substitution of expansion 1.5 into eq. 1.1 yields:

$$\left[\hat{\mathcal{H}}_{el} + \hat{T}(\mathbf{Q})\right] \sum_n \phi_n(\mathbf{q},\mathbf{Q})\chi_{nv}(\mathbf{Q}) = \epsilon_{nv} \sum_n \phi_n(\mathbf{q},\mathbf{Q})\chi_{nv}(\mathbf{Q}), \tag{1.6}$$

with ϵ_{nv} the total molecular energy, i.e. the exact eigenvalue of the full Hamiltonian. Making use of eq. 1.4, eq. 1.6 can be written as

$$\sum_n \Bigg(\left\{\phi_n(\mathbf{q},\mathbf{Q})\left[E_n(\mathbf{Q}) + T(\mathbf{Q})\right] + \left[T(\mathbf{Q})\phi_n(\mathbf{q},\mathbf{Q})\right]\right\}\chi_{nv}(\mathbf{Q}) - \frac{\hbar^2}{2m}\sum_k \left(\frac{\partial\phi_n(\mathbf{q},\mathbf{Q})}{\partial Q_k}\right)\left(\frac{\partial\chi_{nv}(\mathbf{Q})}{\partial Q_k}\right)\Bigg) = \epsilon_{nv}\sum_n \phi_n(\mathbf{q},\mathbf{Q})\chi_{nv}(\mathbf{Q}), \tag{1.7}$$

where it has been used the product rule:

$$\frac{\partial^2}{\partial Q_k^2}\Big(\phi_n\chi_n\Big) = \Big(\frac{\partial^2}{\partial Q_k^2}\phi_n\Big)\chi_n + 2\Big(\frac{\partial}{\partial Q_k}\phi_n\Big)\Big(\frac{\partial}{\partial Q_k}\chi_n\Big) + \phi_n\frac{\partial^2}{\partial Q_k^2}\chi_n, \tag{1.8}$$

Multiplying on the left by $\phi_m(\mathbf{q},\mathbf{Q})^*$, integrating over the electronic coordinates, and switching to the most convenient braket notation, the following set of coupled differential equations are obtained:

$$\begin{aligned}\Big[E_n(\mathbf{Q}) + T(\mathbf{Q}) + \langle n(\mathbf{q},\mathbf{Q})|\, T(\mathbf{Q})\, |n(\mathbf{q},\mathbf{Q})\rangle - \epsilon_{nv}\Big]\chi_{nv} \\ + \sum_{m\neq n}\Big[\,\langle m(\mathbf{q},\mathbf{Q})|\, T(\mathbf{Q})\, |n(\mathbf{q},\mathbf{Q})\rangle \\ -\hbar^2\sum_k \langle m(\mathbf{q},\mathbf{Q})|\, \frac{\partial}{\partial Q_k}\, |n(\mathbf{q},\mathbf{Q})\rangle\, \frac{\partial}{\partial Q_k}\Big]\chi_{nv}(\mathbf{q},\mathbf{Q}) = 0\end{aligned} \tag{1.9}$$

In the eq. above the matrix element $\langle\phi_n|\, \frac{\partial}{\partial Q_k}\, |\phi_n\rangle$ has been omitted, since the expectation value of the linear momentum operator vanishes for any bound state.

Eq. 1.9 consists of two parts, one involving a single electronic state, the other in which coupling terms among electronic states appears. When these latter terms are neglected, the so called nuclear Schrödinger equation for the n-th electronic state is obtained:

$$\left[E_n(\mathbf{Q}) + T(\mathbf{Q}) + \langle n(\mathbf{q},\mathbf{Q})|\, T(\mathbf{Q})\, |n(\mathbf{q},\mathbf{Q})\rangle - \epsilon_{nv}\right]\chi_{nv} = 0 \tag{1.10}$$

That approximation is known as adiabatic approximation; the

expansion coefficients of eq. 1.5 can thus be considered as the nuclear wavefunctions and therefore the total wavefunction can be written as a product of an electronic and nuclear wavefunction:

$$|nv(\mathbf{q},\mathbf{Q})\rangle = |\phi_n(\mathbf{q},\mathbf{Q})\rangle \otimes |\chi_{nv}(\mathbf{Q})\rangle \,. \tag{1.11}$$

Those product states are usually referred to as vibronic states and still play a fundamental role in understanding spectroscopic measurements, the kinetics of electronic transitions, and the mechanism of chemical reactions.

Indeed, over the years the adiabatic approximation has proven to be extremely reliable, especially for treating the ground electronic state. In that case the effects of the nuclear kinetic energy operator on the electronic wavefunction are negligibly small, even the term $\langle n(\mathbf{q},\mathbf{Q})| \, T(\mathbf{Q}) \, |n(\mathbf{q},\mathbf{Q})\rangle$, which is included in the adiabatic nuclear Hamiltonian, turned out to provide a very small corrections to vibronic energies.

When attention is focused on excited-state molecular processes—such as photoinduced reactions, internal conversion, intersystem crossing, and also some kind of electron transfer reactions—the close energetic proximity of the electronic states makes the terms neglected in the adiabatic approximation extremely important, because they induce transitions among electronic states. Under these conditions, the adiabatic BO approximation becomes inadequate for accurately describing the dynamics of molecular systems and computational approaches that explicitly account for these nonadiabatic couplings, namely the last two terms which have been neglected in eq. 1.9, are essential to accurately describe the dynamics of molecules in

their excited states.

In non adiabatic regime, the total wave function is represented as a superposition over multiple adiabatic vibronic states $|nk(\mathbf{q},\mathbf{Q})\rangle$ of eq. 1.11:

$$\Psi(t) = \sum_{nk} C_{nk}(t)\,|nk\rangle\,. \tag{1.12}$$

The expansion coefficients $C_{nk}(t)$, which describe the time evolution of the system, can be calculated by solving the time dependent Schrödinger equation, see below, employing the full non-adiabatic Hamiltonian, i.e. by including the effects of the nuclear kinetic energy on the basis electronic states.

The action of the nuclear kinetic Hamiltonian on the electronic basis states leads, in mass weighted coordinates (see below), to the following terms:

$$\begin{aligned} &\langle\phi_n|\,\hat{T}_{nu}\,|\phi_m\rangle \\ &= -\frac{\hbar^2}{2}\sum_k \Big(\langle\phi_n|\,\frac{\partial^2}{\partial Q_k^2}\,|\phi_m\rangle + 2\,\langle\phi_n|\,\frac{\partial}{\partial Q_k}\,|\phi_m\rangle\,\frac{\partial}{\partial Q_k} + \frac{\partial^2}{\partial Q_k^2}\Big) \end{aligned} \tag{1.13}$$

which can be further rewritten:

$$\langle\phi_n|\,\hat{T}_{nu}\,|\phi_m\rangle = -\frac{\hbar^2}{2}\sum_k \Big(G_{nm}^{(k)} - 2F_{nm}^{(k)}\frac{\partial}{\partial Q_k}\Big) + \frac{\partial^2}{\partial Q_k^2} \tag{1.14}$$

where

$$G_{nm}^{(k)} = \sum_k \langle\phi_n|\,\frac{\partial^2}{\partial Q_k^2}\,|\phi_m\rangle \tag{1.15}$$

and

$$F_{nm}^{(k)} = \langle \phi_n | \frac{\partial}{\partial Q_k} | \phi_m \rangle \tag{1.16}$$

The last term of eq. 1.13 is just the k-th component of $\hat{T}_{nu}$ of the nuclear Schrödinger equation, cf. eq. 1.10, while

$$\Gamma_{nm}^{(k)} = \frac{\hbar^2}{2}\left(G_{nm}^{(k)} + 2F_{nm}^{(k)}\frac{\partial}{\partial Q_k}\right) \tag{1.17}$$

is the k-th component of the non-adiabatic coupling terms which have to be considered in excited states dynamics.

For $n \neq m$ and for non degenerate electronic energies, i.e. $E_n(Q) \neq E_m(Q)$ the Hellmann-Feynman theorem[55, 43] can be used to obtain an alternative expression for $F_{nm}^{(k)}$. The Hellman-Feynman theorem relates how the energy of a system changes with respect to a parameter to the expectation value of the derivative of the Hamiltonian. If $\hat{\mathcal{H}}(\lambda)$ is a Hamiltonian that depends smoothly on a parameter λ and $|\psi(\lambda)\rangle$ is an eigenstate, then the derivative of the energy with respect to λ is:

$$\frac{dE_\lambda}{d\lambda} = \langle \psi(\lambda) | \frac{\partial \hat{\mathcal{H}}_\lambda}{\partial \lambda} | \psi(\lambda) \rangle . \tag{1.18}$$

Taking the derivative with respect to Q_k of

$$\langle \phi_n | \hat{\mathcal{H}}_{el} | \phi_m \rangle = E_{el,nm}\delta_{nm} \tag{1.19}$$

that is:

$$\begin{aligned}\left(\frac{\partial}{\partial Q_k}\langle\phi_n|\right)\hat{\mathcal{H}}_{el}|\phi_m\rangle + \langle\phi_n|\left(\frac{\partial\hat{\mathcal{H}}_{el}}{\partial Q_k}|\phi_m\rangle\right) \\ + \langle\phi_n|\hat{\mathcal{H}}_{el}\left(\frac{\partial}{\partial Q_k}|\phi_m\rangle\right) = \frac{i}{\hbar}F_{k,nm}(E_{el,n}-E_{el,m}) \\ + \langle\phi_n|\left(\frac{\partial\hat{\mathcal{H}}_{el}}{\partial Q_k}|\phi_m\rangle\right) = \\ = \frac{\partial E_{el,n}}{\partial Q_k}\delta_{nm}\end{aligned} \tag{1.20}$$

Since $n \neq m$, the righthand side of the above equation is zero, thus :

$$F_{k,nm} = i\hbar\frac{\langle\phi_n|\left(\partial\hat{\mathcal{H}}_{el}/\partial Q_k\right)|\phi_m\rangle}{E_{el,n}-E_{el,m}} \tag{1.21}$$

given that $E_{el,n} \neq E_{el,m}$.

Eq. 1.21 allows for an alternative evaluation of derivative couplings, for Q values at which the two electronic states are non-degenerate.

Non adiabatic couplings among electronic states describe how fast the electronic wavefunctions changes as the nuclei move. They cause the nuclear wavepacket to evolve not on a single potential energy surface (PES), but hopping between different electronic states. In that way it is possible to follow the decay pathway of an excited molecule and use theoretical calculation to interpret time dependent spectroscopical measurements. To properly describe these nonadiabatic transitions, it is necessary to adopt theoretical frameworks that go beyond the BO approximation.

Over the past decades, a range of computational methodologies have been developed to explicitly incorporate nonadiabatic effects. Trajectory Surface Hopping (TSH)[158] is among the most widely used methods due to its relatively low computational cost and conceptual simplicity. It treats nuclear motion classically while allowing probabilistic hops between electronic states, guided by nonadiabatic coupling vectors. Although widely used, especially because it can be more easily applied to large systems than other full quantum mechanical approaches, TSH lacks a rigorous quantum mechanical foundation, which prevents from a consistent treatment of coherent effects. In contrast, Ab Initio Multiple Spawning (AIMS)[17] provides a more accurate quantum description of the nuclear wavepacket by representing it as a superposition of trajectory-guided basis functions that can be adaptively spawned in regions of strong nonadiabatic interaction. This method captures interference and decoherence effects more faithfully than TSH, but at the cost of significantly greater computational demands and complexity in basis function management. The Multi-Configuration Time-Dependent Hartree (MCTDH)[109] method offers a fully quantum mechanical treatment of both nuclear and electronic dynamics by expanding the total wavefunction in time-dependent, variationally optimized basis sets. MCTDH achieves high accuracy and is especially powerful for systems with a small number of strongly coupled vibrational modes; however, its application is limited by computational scaling, making it impractical for large polyatomic systems.

In this thesis the time dependent perturbation theory will

be used. This approach neglects quantum coherence effects, providing rate constants for elementary transition between electronic states rather than time dependent populations, but it has the advantage of being a full quantum mechanical approach which allows for tunneling effects, which often play the predominant role in the kinetics of elementary transitions between two electronic states. Furthermore, it treats all the nuclear degrees of freedom on the same ground, without posing limitations on the size of basis set.

1.2 Normal modes of vibrations

Another point of considerable importance is the choice of nuclear coordinates. Because the interest is focused on the calculation of rate constants among electronic states, which usually have different equilibrium geometries, and since tunneling crucially depends on the difference between the initial and final equilibrium geometries, it will be necessary to employ in computations nuclear coordinates which allows to easily calculate effective displacements among points of the Q space, without including translational and rotational movements.

Translational motion describes the movement of the molecule as a whole, while rotational motion refers to its rigid rotation around its center of mass. Neither of these motions alters the internal geometry of the molecule. Mathematically, the three different kinds of nuclear motions can be separated each other under certain approximations. Separability arises from the

structure of the molecular Hamiltonian and the fact that translational and rotational coordinates can be removed from the internal degrees of freedom through appropriate coordinate transformations.

Normal coordinates are just the result of a coordinate transformation which allows to separate the center-of-mass motion and overall rotations from the internal motion of the molecule, under the condition that nuclear motion is treated in the harmonic approximation.

Let $\mathbf{x}$ be the $3N$ component vector of the Cartesian coordinate of a N atom molecule and let $\mathbf{x}_0$ the vector of the equilibrium coordinates.

It is convenient to define a new set of mass weighted displacement coordinates:

$$\mathbf{q} = \mathbf{M}^{1/2}(\mathbf{x} - \mathbf{x}_0) \tag{1.22}$$

where $\mathbf{M}$ is the $3N$ matrix of atomic masses. In the previous paragraph it has been shown that in the BO approximation the motion of nuclei take place in the force field created by the electronic motion. Since the functional dependence of E_{el} on the nuclear cooridnates is not known, it is customary to expand $E_{el}(\overrightarrow{q})$ in Taylor series around the equilibrium geometry q_0. For small displacements from the equilibrium coordinate the series can be truncated after a few terms. In the harmonic approximation the expansion is truncated to the second order:

$$2E_{el} = 2E_{el,0} + 2\sum_i \left(\frac{\partial E_{el}}{\partial q_i}\right)_{q_0} q_i + \sum_{i,j} \left(\frac{\partial^2 E_{el}}{\partial q_i \partial q_j}\right)_{q_0} q_i q_j \tag{1.23}$$

$$i, j = 1, ...3N$$

where $E_{el,0}$ is the energy of the equilibrium configuration, which can be set to zero. Considering that:

$$\left(\frac{\partial E_{el}}{\partial q_i}\right)_{q_0} = 0 \tag{1.24}$$

the nuclear Hamiltonian $\hat{\mathcal{H}}_{nu}$ is:

$$\hat{\mathcal{H}}_{nu} = \hat{T}_{nu} + \frac{1}{2}\sum_{i,j} F_{ij} q_i q_j \tag{1.25}$$

with

$$F_{ij} = \left(\frac{\partial^2 E_{el}}{\partial q_i \partial q_j}\right)_{q_0} \tag{1.26}$$

the element of the Hessian matrix, and

$$\hat{T}_{nu} = \frac{1}{2}\sum_{i,j} \dot{q}_i \dot{q}_j \tag{1.27}$$

the kinetic energy, where the dot indicates time derivative.

It is now possible to introduce a new set of coordinates that makes both the kinetic and the potential energy (eq. 1.25) diagonal, thus decoupling the vibrational motion. Let pose

$$\mathbf{Q} = \mathbf{L}^{-1}\mathbf{q} \tag{1.28}$$

substituting in eq. 1.25, the kinetic and potential energy assumes the form:

$$2\hat{T}_{nu} = \dot{\mathbf{Q}}^{\dagger}\mathbf{L}^{\dagger}\mathbf{L}\dot{\mathbf{Q}}, \qquad 2\hat{U} = \mathbf{Q}^{\dagger}\mathbf{L}^{\dagger}\mathbf{F}\mathbf{L}\mathbf{Q} \tag{1.29}$$

The requirement that both **T** and **U** are diagonal is satisfied if:

$$\mathbf{L}^{\dagger} = \mathbf{L}^{-1} \tag{1.30}$$

and

$$\mathbf{L}^{\dagger}\mathbf{F}\mathbf{L} = \mathbf{\Lambda} \tag{1.31}$$

where $\mathbf{\Lambda}$ is a diagonal matrix whose elements are the vibrational frequencies $\lambda_k = 4\pi^2 c_0^2 \nu_k^2$.

The two equations above define the normal mode transformation matrix **L** as the unitary transformation which diagonalizes the Hessian matrix.

If the force constant matrix **f** is build up using coordinates which satisfy the Sayvetz conditions, for instance from internal coordinates via the **B** matrix,[29] its diagonalization will provide six (five for linear molecule) zero eigenvalues whose eigenvectors correspond to translations and rotations and $N_{vib} = 3N - 6$ normal coordinates which correspond to genuine vibrational modes.

Since the normal coordinates constitute a set of N_{vib} indipendent variables, the vibrational Hamiltonian $\hat{\mathcal{H}}_{nu}$ for a molecule in terms of the normal coordinates Q_k can be written as a sum of uncoupled harmonic oscillators each corresponding to a normal mode of vibration :

$$\hat{\mathcal{H}}_{nu} = -\frac{\hbar^2}{2}\sum_k \frac{\partial^2}{\partial Q_k^2} - \frac{1}{2}\sum_k \lambda_k Q_k^2 \tag{1.32}$$

and the nuclear wavefunction X can be written as the product of N_{vib} indipendent function $\chi_k(Q_k)$, each of which is a function

of a single coordinate Q_k

$$|X\rangle = \prod_k |\chi_k\rangle \tag{1.33}$$

1.2.1 Time evolution of quantum states

Understanting the time evolution of quantum states under the influence of external or internal time-dependent interactions is central to the description of dynamical processes in molecular and condensed-phase systems. The dynamics of a system is governed by the time dependent Schrödinger equation

$$i\hbar \frac{\partial}{\partial t} |\Psi(t)\rangle = \hat{\mathcal{H}} |\Psi(t)\rangle \tag{1.34}$$

where $|\Psi\rangle$ is the time dependent wavefunction of the system and $\hat{\mathcal{H}}$ is the Hamiltonian, which may explicity depend on time. In many pratical applications, $\hat{\mathcal{H}}$ can be conveniently expressed as the sum of a time-indipendent term $\hat{\mathcal{H}}^0$, whose eigenstates are analitically or numerically known by solving :

$$\hat{\mathcal{H}}^0 |\psi_n^0\rangle = E_n^0 |\psi_n^0\rangle , \tag{1.35}$$

and a time-dependent perturbation $\hat{\mathcal{H}}'(t)$:

$$\hat{\mathcal{H}} = \hat{\mathcal{H}}^0 + \hat{\mathcal{H}}'(t) \tag{1.36}$$

According to the superposition principle the time dependent wavefunction can be expressed as linear combination of eigenfunctions:

$$|\Psi(t)\rangle = \sum_{j=1}^{+\infty} c_j(t)\,|\psi_j^0(t)\rangle \tag{1.37}$$

where $c_j(t)$ are the probability amplitude that the system is in the eigenstate $|\psi_j^0\rangle$ after a time t, and time dependence of the eigenfunctions $|\psi_j^0(t)\rangle$ is

$$|\psi_j^0(t)\rangle = e^{-E_j t/\hbar}\,|\psi_j^0\rangle \tag{1.38}$$

In the case the Hamiltonian is not a function of time, as in most of cases of interest, eq. 1.37 can be in principle easily solved when the eigenstates of the whole Hamiltonian matrix are known. However, in practice the size of the vibronic space of interest is so large to prevent any attempt of direct diagonalization of $\hat{\mathcal{H}}$. The different methodologies which have been developed in last fifty years for solving eq. 1.37 are just different ways of addressing this formidable problem.

Another technique, which does not make use of the eigenvectors of the full $\hat{\mathcal{H}}$, is the time dependent perturbation theory, which is summarized in Appendix A. At the first order of time dependent perturbation theory, the probability amplitude for the system in $|\psi_i\rangle$ to be in $|\psi_f\rangle$ after a time t, from the first order time dependent perturbation theory, is:

$$c_f(t) = \frac{\langle\psi_f^0|\,\hat{\mathcal{H}}'\,|\psi_i^0\rangle}{\hbar\omega_{fi}}\left(1 - e^{i\omega_{fi}t}\right) \tag{1.39}$$

with ω_{fi} the angular frequency :

$$\omega_{fi} = \frac{E_f^0 - E_i^0}{\hbar}, \tag{1.40}$$

and the probability of transition $P_{f \longleftarrow i}$

$$P_{f \longleftarrow i} = |c_f(t)|^2 \tag{1.41}$$

The population of the vibrational states within each initial electronic states is governed by the Boltzmann factor $e^{(-E_{iv}/\beta)}$ where $\beta = 1/(k_B T)$ and k_B is the Boltzmann constant. In the case of polyatomic molecules, especially when the energy difference between the inital and final state is large, a vibrational manifold of final vibronic states approaching to a continuum is available and therefore one has to account for all the states which the system can jump to: the probability of any vibronic transition must be summed over all possible final states. This is done by integrating the transition probability with the density of state $\rho(E)$ as weights :

$$P_{f \longleftarrow i} = \int |c_f(t)|^2 \rho(E_{fi}) dE_{fi} \tag{1.42}$$

As demonstrated in Appendix A, the transition rate K is:

$$K_{f \longleftarrow i} = \frac{\partial P_{f \longleftarrow i}}{\partial t} = \frac{2\pi}{\hbar} |\hat{\mathcal{H}}'_{fi}|^2 \rho(E_{fi}) = \frac{2\pi}{\hbar} F(\Delta E, T) \tag{1.43}$$

a very important result which is known as Fermi's Golden Rule (FGR). In radiative transitions, such as absorption, fluorescence,

phosphorescence, the perturbation $\hat{\mathcal{H}}'$ arises from the interaction between the molecule and the electromagnetic field. Within the electric dipole approximation, this interaction is expressed as :

$$\hat{\mathcal{H}}' = -\hat{\boldsymbol{\mu}} \cdot \mathbf{E}(t) \tag{1.44}$$

where $\hat{\boldsymbol{\mu}}$ is the electric dipole moment operator and $\mathbf{E}(t)$ is the time-dependent electric field vector. Within the BO approximation, the Franck-Condon principle assumes that electronic transitions occur much faster than nuclear motion, allowing nuclear positions to be considered fixed during the electronic transition. Formally the Franck-Condon principle allows to integrate first over the electronic coordinates and then on the nuclear ones. If the first integration over the electronic coordinates yields a scalar, i.e. a quantity independent on nuclear coordinates, then the matrix element in eq. 1.39 for a transition between the initial and final molecular states turns out to be factorized into an electronic and a vibrational component:

$$\langle \psi_f | \hat{\mathcal{H}}' | \psi_i \rangle = \langle \phi_f | \hat{\mathcal{H}}' | \phi_i \rangle \langle \chi_f | \chi_i \rangle \tag{1.45}$$

In the case of radiative transitions, cfr. eq. 1.44, the electrical dipole moment operator is certainly a function of nuclear coordinates, but often its dependence on Q is neglected. That is called the Condon approximation, a term which has been often used in other context to indicate the independence of nuclear coordinates of some electronic term.

The nuclear overlap $\langle \chi_f | \chi_i \rangle$ is called the Franck-Condon integral and plays a central role in vibronic spectroscopy as well

as in the study of radiationless transitions,[145, 75] including the whole class of redox reactions.[102, 121, 21, 23]

In the context of molecular excited-state dynamics, the perturbation $\hat{\mathcal{H}}'$ can originate not only from light-matter interaction but also from couplings induced by nuclear motion and by magnetic or relativistic effects, which in first approximation have been neglected in the electronic Hamiltonian.

As it will be shown in the next section all these processes can be treated within the framework of FGR approach. For FGR to be valid, however, it is necessary that: (i) the perturbation should be small compared to the energy difference between the two states involving in the transition; (ii) there should be a continuum of final states; (iii) the time should be short enough that the perturbation could be considered weak, but long enough to observe the transition.

1.3 The Generating Function Approach

In the 1955, Kubo and Toyozawa[76] applied the generating function method to discuss radiative and non radiative transitions on a general model of lattice vibration comparable to real crystals. They carried out a purely quantum mechanical treatment of the reaction rate, in which the density matrices play a central role. The rate of transition could be accurately determined because of the inclusion of the whole set of vibrational states that the system may occupy. In this section the approach will be analysed in great details, both in the case the Condon approximation is invoked and in the case the dependence on

the nuclear coordinates is preserved, a case for which a novel expression of the rate in terms of the initial and final sets of normal coordinates of the system is presented.

Let m and n two electronic states, and let μ and ν represent the vibrational states associated with each electronic state, from the first order time dependent perturbation theory, the kinetic constant K of the vibronic transition between initial i and final f state is:

$$K_{f\longleftarrow i} = \frac{2\pi}{\hbar}\sum_{\mu}\sum_{\nu}|\hat{\mathcal{H}}'_{n\nu,m\mu}|^2 w_{m\mu}(T)\delta(E-\Delta E_{mn}+E_{n\nu}-E_{m\mu}) = \frac{2\pi}{\hbar}F(\bar{E},T) \tag{1.46}$$

where $w_{m\mu}$ is the vibrational partition function of initial state,[1]

$$w_{m\mu} = \prod_{\mu}\frac{e^{-\beta E_{m\mu}/2}}{1-e^{-\beta E_{m\mu}}} \tag{1.47}$$

$$w_{m\mu} = 1/\det(2\sinh(\beta E_m/2)) = \mathrm{Tr}\rho_m(\beta) \tag{1.48}$$

The infinite double summation appearing in Eqn 1.46 obviously poses problems; it is therefore advantageous to consider the Laplace transform of $F(\bar{E},T)$:

$$f(\lambda) = \int_{-\infty}^{+\infty} F(\bar{E},T)e^{-\lambda\bar{E}}d\bar{E} \tag{1.49}$$

[1]Note that $E_{n\nu}$ and $E_{m\mu}$ have to be referred to a common zero; if each vibronic energy is referred to its own electronic energy a term $\Delta E = E_n - E_m$ appears in the expression above, where E_m is the electronic energy.

with $\bar{E} = E - E_{mn}$. From the properties of Dirac's δ function it can be easily shown that:

$$\begin{aligned} f(\lambda) = 1/\mathrm{Tr}\rho_m(\beta) \sum_{\mu}\sum_{\nu} |\langle n\nu|\,\hat{\mathcal{H}}'\,|m\mu\rangle|^2 e^{-\lambda(E_{n\nu}-E_{m\mu})} e^{-\beta E_{m\mu}} \\ = 1/\mathrm{Tr}\rho_m(\beta) \sum_{\mu}\sum_{\nu} \langle m\mu|\,\hat{\mathcal{H}}'\,|n\nu\rangle\, e^{-\lambda E_{n\nu}} \\ \langle n\nu|\,\hat{\mathcal{H}}' e^{-(\beta-\lambda)E_{m\mu}} \sum_{w} |mw\rangle\,\langle mw|m\mu\rangle \\ = 1/\mathrm{Tr}\rho_m(\beta) \sum_{\nu} \langle m\mu|\,\hat{\mathcal{H}}'\,|n\nu\rangle\, e^{-\lambda E_{n\nu}} \\ \langle n\nu|\,\hat{\mathcal{H}}' \sum_{\mu} |m\mu\rangle\, e^{-(\beta-\lambda)E_{m\mu}}\,\langle m\mu|m\mu\rangle \end{aligned} \tag{1.50}$$

By introducing the Born-Oppenheimer approximation and integrating over the electronic coordinates:

$$\begin{aligned} f(\lambda) = \sum_{\mu} \langle m\mu|\,\hat{\mathcal{H}}'_{m,n}\rho_n(\lambda)\hat{\mathcal{H}}'_{nm}\rho_m(\beta-\lambda)\,|m\mu\rangle\,/\mathrm{Tr}\rho_m(\beta) \\ = \mathrm{Tr}\hat{\mathcal{H}}'_{mn}\rho_n(\lambda)\hat{\mathcal{H}}'_{nm}\rho_m(\beta-\lambda)/\mathrm{Tr}\rho_m(\beta) \end{aligned} \tag{1.51}$$

where:

$$\rho_n(\lambda) = \sum_{\nu n} |\nu n\rangle\, e^{-\lambda E_{\nu n}}\,\langle \nu n| \tag{1.52}$$

$$\rho_m(\beta-\lambda) = \sum_{\mu m} |\mu m\rangle\, e^{-(\beta-\lambda)E_{\mu m}}\,\langle \mu m| \tag{1.53}$$

and the orthogonality of the basis state, i.e. $\langle mw|m\mu\rangle = \delta_{mw,m\mu}$ has been used wherever necessary. Eq 1.51 no longer contains intractable summations; the trace still appearing can be easily

evaluated in the normal coordinate representation:

$$
\begin{aligned}
f(\lambda) &= \int\int d\mathbf{Q}d\mathbf{Q}' \sum_{\mu} \langle \mu_m|\mathbf{Q}\rangle \\
\times \langle \mathbf{Q}| \hat{\mathcal{H}}'_{mn}\rho_n(\lambda)\hat{\mathcal{H}}'_{nm}\rho_m(\beta-\lambda) |\mathbf{Q}'\rangle \langle \mathbf{Q}'|\mu_m\rangle \,/\mathrm{Tr}\rho_m(\beta) \\
&= \int\int d\mathbf{Q}d\mathbf{Q}' \langle \mathbf{Q}| \hat{\mathcal{H}}'_{mn}\rho_n(\lambda)\hat{\mathcal{H}}'_{nm}\rho_m(\beta-\lambda) |\mathbf{Q}'\rangle \\
&\qquad \times \sum_{\mu} \langle \mathbf{Q}'|\mu_m\rangle \langle \mu_m|\mathbf{Q}\rangle \,/\mathrm{Tr}\rho_m(\beta) \qquad (1.54) \\
&= \int\int d\mathbf{Q}d\mathbf{Q}' \langle \mathbf{Q}| \hat{\mathcal{H}}'_{mn}\rho_n(\lambda)\hat{\mathcal{H}}'_{nm}\rho_m(\beta-\lambda) |\mathbf{Q}'\rangle \\
&\qquad \times \langle \mathbf{Q}'|\mathbf{Q}\rangle \,/\mathrm{Tr}\rho_m(\beta) \\
&= \int d\mathbf{Q} \langle \mathbf{Q}| \hat{\mathcal{H}}'_{mn}\rho_n(\lambda)\hat{\mathcal{H}}'_{nm}\rho_m(\beta-\lambda) |\mathbf{Q}\rangle \,/\mathrm{Tr}\rho_m(\beta)
\end{aligned}
$$

where the resolution of identity:

$$
\mathbf{I} = \int d\mathbf{Q}' |\mathbf{Q}'\rangle \langle \mathbf{Q}'| \qquad\qquad I = \sum_{\mu} |\mu_m\rangle \langle \mu_m| \qquad (1.55)
$$

has been used wherever necessary.

In order to evaluate $\rho_m(\beta-\lambda)$ and $\rho_n(\lambda)$ in the normal coordinate representation, the harmonic approximation for nuclear motions is used together with the well known formula for the density matrix of the one dimensional harmonic oscillator with frequency ω and unit mass:

$$
\begin{aligned}
\langle q| \rho(\lambda) |\bar{q}\rangle &= (2\pi\hbar \sinh(\beta\hbar\omega)/\omega)^{-1/2} \\
&\times \exp[-(\omega/4\hbar)\tanh(\beta\hbar\omega/2)(q+\bar{q})^2 \qquad (1.56) \\
&\quad -(\omega/4\hbar)\coth(\beta\hbar\omega/2)(q-\bar{q})^2]
\end{aligned}
$$

The density matrix for a system consisting of N harmonic oscillators is obtained by simply taking the product of eq. 1.56 over all the normal modes, which in tensor formalism is:[2]

$$\begin{aligned}\langle \mathbf{Q}| \rho_m(\beta-\lambda) |\bar{\mathbf{Q}}\rangle = [\det(2\pi\hbar\mathbf{\Omega}_m^{-1}\sinh((\beta-\lambda)\hbar\mathbf{\Omega}_m))]^{-1/2} \\ \times \exp[-1/4(\mathbf{Q}+\bar{\mathbf{Q}})^{\dagger}(\hbar^{-1}\mathbf{\Omega}_m)\tanh[(\beta-\lambda)\hbar\mathbf{\Omega}_m/2](\mathbf{Q}+\bar{\mathbf{Q}}) \\ -1/4(\mathbf{Q}-\bar{\mathbf{Q}})^{\dagger}(\hbar^{-1}\mathbf{\Omega}_m)\coth[(\beta-\lambda)\hbar\mathbf{\Omega}_m/2](\mathbf{Q}-\bar{\mathbf{Q}})]\end{aligned} \tag{1.57}$$

where $\mathbf{\Omega}_m$ is the diagonal matrix of the vibrational frequencies of $|m\rangle$. A similar expression holds for any electronic state $|n\rangle$, it is sufficient to replace $\mathbf{Q}_m$ and $\mathbf{\Omega}_m$ with their counterparts $\mathbf{Q}_n$ and $\mathbf{\Omega}_n$.

The expression for $f(\lambda)$ in eq. 1.54 makes use of both ρ_m and ρ_n. It is therefore necessary to evaluate the coordinate representation of the density matrix of an electronic state in the normal modes coordinates of a different electronic state. Of course, the normal modes of different electronic states, i.e. $\mathbf{Q}_m$ and $\mathbf{Q}_n$, are not independent variables, rather they are related by Duschinski transformation:

$$\mathbf{Q}_n = \mathbf{J}\mathbf{Q}_m + \mathbf{K} \tag{1.58}$$

where $\mathbf{J}$ is called the rotation or the Duschinski matrix and $\mathbf{K}$ is the displacement vector, which accounts for the change of the atomic equilibrium positions of the electronic state $|n\rangle$ with respect to those of $|m\rangle$. Let $\mathbf{X}$ be the set of mass weighted

[2]Note that the equilibrium position does not appear in the expression below because normal modes are already displacement coordinates.

Cartesian coordinates in term of which the normal modes of all the electronic states are defined:

$$\mathbf{Q_1} = \mathbf{L_1^{-1}}(\mathbf{X} - \mathbf{X_1^0}), \qquad \mathbf{Q_2} = \mathbf{L_2^{-1}}(\mathbf{X} - \mathbf{X_2^0}) \tag{1.59}$$

From eq. 1.59:

$$\mathbf{L_1}\mathbf{Q_1} + \mathbf{X_1^0} = \mathbf{L_2}\mathbf{Q_2} + \mathbf{X_2^0} \qquad \mathbf{Q_1} = \mathbf{L_1^\dagger}\mathbf{L_2}\mathbf{Q_2} + \mathbf{L_1^\dagger}(\mathbf{X_2^0} - \mathbf{X_1^0}) \tag{1.60}$$

Comparison of eq. 1.59 and 1.60 with 1.58 yields:

$$\mathbf{J} = \mathbf{L_1^\dagger}\mathbf{L_2}, \qquad \mathbf{K} = \mathbf{L_1^\dagger}(\mathbf{X_2^0} - \mathbf{X_1^0}) \tag{1.61}$$

In order to obtain the expression of the density matrix in the coordinate representation expressed in term of the normal modes of a different electronic state, that is $\rho_n(Q_m, \bar{Q}_m, T)$, it is sufficient to start from Mehler's expression in terms of normal coordinates of the electronic state $|n\rangle$,

$$\begin{aligned}
&\langle \mathbf{Q}_m | \, e^{-\lambda H_n} \, | \bar{\mathbf{Q}}_m \rangle \\
&= \int d\mathbf{Q}_n d\bar{\mathbf{Q}}_n \, \langle \mathbf{Q}_m | \mathbf{Q}_n \rangle \, \langle \mathbf{Q}_n | \, e^{-\lambda H_n} \, | \bar{\mathbf{Q}}_n \rangle \, \langle \overline{\mathbf{Q}}_n | \overline{\mathbf{Q}}_m \rangle \\
&= A_n(\lambda) \int d\mathbf{Q}_n d\bar{\mathbf{Q}}_n \delta(\mathbf{Q}_m - \mathbf{Q}_n) \delta(\bar{\mathbf{Q}}_m - \bar{\mathbf{Q}}_n) \\
\times \exp\Big[&- \frac{1}{4} (\bar{\mathbf{Q}}_n + \mathbf{Q}_n)^\dagger \hbar^{-1} \mathbf{\Omega}_n \tanh(\lambda \hbar \mathbf{\Omega}_n / 2) (\bar{\mathbf{Q}}_n + \mathbf{Q}_n) \\
&- \frac{1}{4} (\mathbf{Q}_n - \overline{\mathbf{Q}}_n)^\dagger \hbar^{-1} \mathbf{\Omega}_n \coth(\lambda \hbar \mathbf{\Omega}_n / 2) (\bar{\mathbf{Q}}_n - \mathbf{Q}_n) \Big],
\end{aligned} \tag{1.62}$$

and project over the normal modes of the other state:

$$\begin{aligned}\langle \mathbf{Q}_m |\, e^{-\lambda H_n}\, |\bar{\mathbf{Q}}_m\rangle = A_n(\lambda) \exp\Big[-\frac{1}{4}\left(\mathbf{J}\left(\bar{\mathbf{Q}}_m + \mathbf{Q}_m\right) + 2\mathbf{K}\right)^{\dagger} \\ \times \frac{\mathbf{\Omega}_n}{\hbar} \tanh(\lambda\hbar\mathbf{\Omega}_n/2)\left(\mathbf{J}\left(\bar{\mathbf{Q}}_m + \mathbf{Q}_m\right) + 2\mathbf{K}\right) \\ -\frac{1}{4}\left(\mathbf{J}\left(\mathbf{Q}_m - \overline{\mathbf{Q}}_m\right)\right)^{\dagger} \frac{\mathbf{\Omega}_n}{\hbar} \coth(\lambda\hbar\mathbf{\Omega}_n/2)\left(\mathbf{J}\left(\mathbf{Q}_m - \overline{\mathbf{Q}}_m\right)\right)\Big]\end{aligned} \tag{1.63}$$

with:

$$A_n(\lambda) = [\det(2\pi\hbar\mathbf{\Omega}_n^{-1}\sinh(\lambda\hbar\mathbf{\Omega}_n))]^{-1/2} \tag{1.64}$$

Let

$$\mathbf{T}_n(\lambda) = \mathbf{J}^{\dagger}\frac{\mathbf{\Omega}_n}{\hbar}\tanh(\lambda\hbar\mathbf{\Omega}_n/2)\mathbf{J} \tag{1.65}$$

$$\mathbf{C}_n(\lambda) = \mathbf{J}^{\dagger}\frac{\mathbf{\Omega}_n}{\hbar}\coth(\lambda\mathbf{\Omega}_n/2)\mathbf{J}, \tag{1.66}$$

$$\mathbf{\Delta} = -\mathbf{J}^{-1}\mathbf{K} \tag{1.67}$$

$\rho_n(Q_m, \bar{Q}_m, T)$ finally is:

$$\begin{aligned}\langle \mathbf{Q}_m |\, e^{-\lambda H_n}\, |\bar{\mathbf{Q}}_m\rangle = A_n(\lambda)\times \\ \exp\Big[-\frac{1}{4}\left(\mathbf{Q}_m + \bar{\mathbf{Q}}_m - 2\mathbf{\Delta}\right)^{\dagger}\mathbf{T}_n(\lambda)\left(\mathbf{Q}_m + \bar{\mathbf{Q}}_m - 2\mathbf{\Delta}\right) \\ -\frac{1}{4}\left(\mathbf{Q}_m - \overline{\mathbf{Q}}_m\right)^{\dagger}\mathbf{C}_n(\lambda)\left(\mathbf{Q}_m - \overline{\mathbf{Q}}_m\right)\Big]\end{aligned} \tag{1.68}$$

Let us now recast eq. 1.54 as follows:

$$f(\lambda) = 1/\mathrm{Tr}\rho_m(\beta) \int_{-\infty}^{+\infty} \int\int\int d\mathbf{Q} d\mathbf{Q}' d\bar{\mathbf{Q}} d\bar{\mathbf{Q}}' \langle \mathbf{Q}| \hat{\mathcal{H}}'_{mn} |\mathbf{Q}'\rangle \langle \mathbf{Q}'| \rho_n(\lambda) |\bar{\mathbf{Q}}'\rangle \langle \bar{\mathbf{Q}}'| \hat{\mathcal{H}}'_{nm} |\bar{\mathbf{Q}}\rangle \langle \bar{\mathbf{Q}}| \rho_m(\beta - \lambda) |\mathbf{Q}\rangle . \tag{1.69}$$

Substituting eq. 1.48, 1.57 and 1.68 in 1.69 the following equation for $f(\lambda)$ in terms of normal modes of the initial electronic state is obtained:

$$\begin{aligned} f(\lambda) = A_m(\beta-\lambda)A_n(\lambda)W(\beta) \times \int d\mathbf{Q} d\bar{\mathbf{Q}} d\mathbf{Q}' d\bar{\mathbf{Q}}' \\ \times \langle \bar{\mathbf{Q}}'| \hat{\mathcal{H}}'_{mn} |\bar{\mathbf{Q}}\rangle \times \exp\left[-1/4(\mathbf{Q}+\bar{\mathbf{Q}}-2\Delta)^\dagger \mathbf{T}_n(\lambda)(\mathbf{Q}+\bar{\mathbf{Q}}-2\Delta)\right] \\ \times \exp\left[-1/4(\mathbf{Q}-\bar{\mathbf{Q}})^\dagger \mathbf{C}_n(\lambda)(\mathbf{Q}-\bar{\mathbf{Q}})\right] \\ \times \langle \mathbf{Q}| \hat{\mathcal{H}}'_{nm} |\mathbf{Q}'\rangle \exp\left[-1/4(\mathbf{Q}'+\bar{\mathbf{Q}}')^\dagger \mathbf{T}_m(\beta-\lambda)(\mathbf{Q}'+\bar{\mathbf{Q}}')\right] \\ \times \exp\left[-1/4(\mathbf{Q}'-\bar{\mathbf{Q}}')^\dagger \mathbf{C}_m(\beta-\lambda)(\mathbf{Q}'-\bar{\mathbf{Q}}')\right] \end{aligned} \tag{1.70}$$

where:

$$W(\beta) = [\det(2\sinh(\hbar\boldsymbol{\Omega}_m\beta/2)]^{-2} \tag{1.71}$$

$$\mathbf{T}_m(\gamma) = \frac{\boldsymbol{\Omega}_m}{\hbar}\tanh(\gamma\hbar\boldsymbol{\Omega}_m/2) \tag{1.72}$$

$$\mathbf{C}_m(\gamma) = \frac{\boldsymbol{\Omega}_m}{\hbar}\coth(\gamma\hbar\boldsymbol{\Omega}_m/2) \tag{1.73}$$

with $\gamma = \beta - \lambda$.

1.3.1 Electronic coupling independent of nuclear coordinates

When $\hat{\mathcal{H}}'_{mn}$ is independent of nuclear coordinates:

$$\langle \mathbf{Q}| \, \hat{\mathcal{H}}'_{mn} \, |\mathbf{Q}'\rangle = \hat{\mathcal{H}}'_{mn} \, \langle \mathbf{Q}|\mathbf{Q}'\rangle = \hat{\mathcal{H}}'_{mn}\delta(\mathbf{Q}-\mathbf{Q}') \tag{1.74}$$

which means that only terms different from zero are those for which $\mathbf{Q} = \mathbf{Q}'$. Similarly, for $\langle \overline{\mathbf{Q}}| \, \hat{\mathcal{H}}'_{mn} \, |\overline{\mathbf{Q}'}\rangle$, the only terms different from zero are those for which $\overline{\mathbf{Q}} = \overline{\mathbf{Q}'}$. Setting therefore $\mathbf{Q} = \mathbf{Q}'$ and $\overline{\mathbf{Q}} = \overline{\mathbf{Q}'}$, the integration over $\mathbf{Q}'$ and $\overline{\mathbf{Q}'}$ yields :

$$\begin{aligned} f(\lambda) = |\hat{\mathcal{H}}'_{mn}|^2\theta \int\int d\mathbf{Q}d\overline{\mathbf{Q}} \\ \times \exp\Big[-\frac{1}{4}(\mathbf{Q}+\overline{\mathbf{Q}}-2\Delta)^\dagger \mathbf{T}_n(\mathbf{Q}+\overline{\mathbf{Q}}-2\Delta) \\ -\frac{1}{4}(\mathbf{Q}-\overline{\mathbf{Q}})^\dagger \mathbf{C}_n(\mathbf{Q}-\overline{\mathbf{Q}})\Big] \\ \times \exp\Big[-\frac{1}{4}(\mathbf{Q}+\overline{\mathbf{Q}})^\dagger \mathbf{T}_m(\mathbf{Q}+\overline{\mathbf{Q}}) - \frac{1}{4}(\mathbf{Q}-\overline{\mathbf{Q}})^\dagger \mathbf{C}_m(\mathbf{Q}-\overline{\mathbf{Q}})\Big] \end{aligned} \tag{1.75}$$

with

$$\begin{aligned} \theta = \{\det[4\pi^2\hbar^2(2\sinh(\beta\hbar\mathbf{\Omega}_m/2))^{-2}\mathbf{\Omega}_m^{-1} \\ \times \sinh((\beta-\lambda)\hbar\mathbf{\Omega}_m)\mathbf{\Omega}_n^{-1}\sinh(-\lambda\hbar\mathbf{\Omega}_n)]\}^{-1/2} \end{aligned} \tag{1.76}$$

The integration can be easily performed with a change of variables :

$$\mathbf{u} = \frac{\mathbf{Q}+\overline{\mathbf{Q}}}{2} \qquad\qquad \mathbf{v} = \frac{\mathbf{Q}-\overline{\mathbf{Q}}}{2} \tag{1.77}$$

$$\begin{pmatrix} \mathbf{Q} \\ \overline{\mathbf{Q}} \end{pmatrix} = \begin{pmatrix} \mathbf{I} & \mathbf{I} \\ \mathbf{I} & -\mathbf{I} \end{pmatrix} \begin{pmatrix} \mathbf{u} \\ \mathbf{v} \end{pmatrix} \tag{1.78}$$

where $\mathbf{I}$ is the unit matrix of size N_{vib}.

$$\begin{aligned} f(\lambda) = |\hat{\mathcal{H}}'_{mn}|^2 2^{N_{vib}} \theta \int \int d\mathbf{u} d\mathbf{v} \\ \exp\Big[-(\mathbf{u}-\Delta)^\dagger \mathbf{T}_n (\mathbf{u}-\Delta) - \mathbf{v}^\dagger \mathbf{C}_n \mathbf{v} \Big] \\ \times \exp\Big[-\mathbf{u}^\dagger \mathbf{T}_m \mathbf{u} - \mathbf{v}^\dagger \mathbf{C}_m \mathbf{v} \Big] \end{aligned} \tag{1.79}$$

where $2^{N_{vib}}$ is the Jacobian of transformation.

The two exponentials in the integral above are two Gaussian densities so their product is also a Gaussian density. Setting

$$\mathbf{m} = (\mathbf{T}_m + \mathbf{T}_n)^{-1} \mathbf{T}_n \Delta, \tag{1.80}$$

$$\begin{aligned} f(\lambda) = |\hat{\mathcal{H}}'_{mn}|^2 2^n \theta \exp[-\Delta^\dagger \mathbf{T}_n \Delta + \mathbf{m}^\dagger (\mathbf{T}_m + \mathbf{T}_n)^{-1} \mathbf{m}] \\ \times \int d\mathbf{u} \exp\Big[-(\mathbf{u}-\mathbf{m})^\dagger (\mathbf{T}_m + \mathbf{T}_n)(\mathbf{u}-\mathbf{m}) \Big] \\ \times \int d\mathbf{v} \exp\Big[-\mathbf{v}^\dagger (\mathbf{C}_m + \mathbf{C}_n) \mathbf{v} \Big]. \end{aligned} \tag{1.81}$$

After carrying out the integration over $\mathbf{u}$ and $\mathbf{v}$, the resulting expression is obtained:

$$f(\lambda) = |\hat{\mathcal{H}}'_{mn}|^2 \Theta \exp[-\Delta^\dagger \mathbf{T}_n (\mathbf{T}_m + \mathbf{T}_n)^{-1} \mathbf{T}_m \Delta] \tag{1.82}$$

with

$$\Theta = 2^{N_{vib}} \theta \Big(\frac{\det(\mathbf{T}_m + \mathbf{T}_n)}{\pi^{N_{vib}}} \Big)^{-1/2} \Big(\frac{\det(\mathbf{C}_m + \mathbf{C}_n)}{\pi^{N_{vib}}} \Big)^{-1/2} \tag{1.83}$$

The procedure and details of the Gaussian integration are provided in Appendix B.

In this formulation, it is assumed a Q-independent perturbative term $\hat{\mathcal{H}}'$.

1.3.2 The case of non-adiabatic coupling terms

Here, the case in which $\hat{\mathcal{H}}'$ is constituted by those terms arising from the action of the nuclear kinetic operator on the electronic wavefunction is considered. In this case $\hat{\mathcal{H}}'$ reflects non-adiabatic coupling between the two electronic states mediated by nuclear motion and explicitly depends on nuclear coordinates. The total Hamiltonian is :

$$\hat{\mathcal{H}} = \sum E^0_{m\mu} \left|m\mu\right\rangle \left\langle m\mu\right| + \sum \hat{\mathcal{H}}'_{m\mu,n\nu} \left|m\mu\right\rangle \left\langle n\nu\right| + c.c \qquad (1.84)$$

where only the terms involving the first derivative of the electronic wavefunction with respect to the vibrational coordinates are retained, while their dependence on the nuclear coordinates is neglected. In eq. 1.84 the summations run over the whole set of vibronic states, $E^0_{m\mu}$'s are the energies of the basis states, and

$$\hat{\mathcal{H}}'_{mn} = \sum_i \left(\left\langle m\right| \frac{i\hbar\partial}{\partial Q_{mi}} \left|n\right\rangle \right)_{Q^0_{mi}} \left\langle m\mu\right| \frac{i\hbar\partial}{\partial Q_{mi}} \left|n\nu\right\rangle \qquad (1.85)$$

or, in tensor formalism :

$$\hat{\mathcal{H}}'_{mn} = -i\mathbf{S}^{\dagger}\partial/\partial\mathbf{Q}_m \qquad (1.86)$$

where

$$S_j = -i\hbar \sum_j \left(\langle m| \frac{\partial}{\partial Q_{mj}} |n\rangle \right)_{Q^0_{mi}} \tag{1.87}$$

In the equations above, and hereafter, the vibrational indices μ and ν are suppressed, so that $\hat{\mathcal{H}}'_{m\mu,n\nu}$ is written as $\hat{\mathcal{H}}'_{mn}$.

With the nuclear kinetic energy operator as perturbative term, the eq. 1.54 is given by the product of two probability amplitudes:

$$f(\lambda) = \int\int d\mathbf{Q} d\overline{\mathbf{Q}} \\ \langle \mathbf{Q}| \hat{\mathcal{H}}'_{mn} \rho_n(\lambda) |\overline{\mathbf{Q}}\rangle \langle \overline{\mathbf{Q}}| \hat{\mathcal{H}}'_{nm} \rho_m(\beta - \lambda) |\mathbf{Q}\rangle / \mathrm{Tr}\rho_m(\beta) \tag{1.88}$$

where

$$\begin{aligned} \langle \mathbf{Q}| \hat{\mathcal{H}}'_{mn} \rho_n(\lambda) |\overline{\mathbf{Q}}\rangle &= \int d\mathbf{Q}' \langle \mathbf{Q}| \hat{\mathcal{H}}'_{mn} |\mathbf{Q}'\rangle \langle \mathbf{Q}'| \rho_n(\lambda) |\overline{\mathbf{Q}}\rangle \\ &= -\mathbf{S}^\dagger \int d\mathbf{Q}' \frac{\partial}{\partial \mathbf{Q}} \delta(\mathbf{Q} - \mathbf{Q}') \rho_n(\mathbf{Q}', \overline{\mathbf{Q}}, \lambda) \\ &= -\mathbf{S}^\dagger \frac{\partial}{\partial \mathbf{Q}} \rho_n(\mathbf{Q}, \overline{\mathbf{Q}}, \lambda) \end{aligned} \tag{1.89}$$

Similarly:

$$\begin{aligned} &\langle \overline{\mathbf{Q}}| \hat{\mathcal{H}}'_{nm} \rho_m(\beta - \lambda) |\mathbf{Q}\rangle = \\ &\int d\overline{\mathbf{Q}'} \langle \overline{\mathbf{Q}}| \hat{\mathcal{H}}'_{nm} |\overline{\mathbf{Q}'}\rangle \langle \overline{\mathbf{Q}'}| \rho_m(\beta - \lambda) |\mathbf{Q}\rangle \\ &= \frac{\partial}{\partial \overline{\mathbf{Q}}^\dagger} \rho_m(\mathbf{Q}, \overline{\mathbf{Q}}, (\beta - \lambda)) \mathbf{S} \end{aligned} \tag{1.90}$$

where the Hermiticity condition of $\hat{\mathcal{H}}$ has been employed.

The derivatives in eq. 1.89 and 1.90 can be easily evaluated noted that for a multivariate Gaussian distribution $p(\mathbf{x})$ with mean $\boldsymbol{\alpha}$ and covariance $\boldsymbol{\Sigma}$:

$$\frac{\partial p(\mathbf{x})}{\partial \mathbf{x}} = -p(\mathbf{x})\boldsymbol{\Sigma}^{-1}(\mathbf{x}-\boldsymbol{\alpha}) \tag{1.91}$$

Thus,

$$\begin{aligned} f(\lambda) = -2^{N_{vib}}\theta \exp[-\Delta^{\dagger}\mathbf{T}_n(\mathbf{T}_m+\mathbf{T}_n)^{-1}\mathbf{T}_m\Delta]\mathbf{S}^{\dagger}\Big(\int\int d\mathbf{u}d\mathbf{v} \\ \exp[-(\mathbf{u}-\mathbf{m})^{\dagger}(\mathbf{T}_m+\mathbf{T}_n)(\mathbf{u}-\mathbf{m}) - \mathbf{v}^{\dagger}(\mathbf{C}_m+\mathbf{C}_n)\mathbf{v}] \\ \times[\mathbf{T}_n(\mathbf{u}-\Delta)\mathbf{u}^{\dagger}\mathbf{T}_m - \mathbf{C}_n\mathbf{v}\mathbf{v}^{\dagger}\mathbf{C}_m]\Big)\mathbf{S} \end{aligned} \tag{1.92}$$

where it has been used the same change of variables as in eq. 1.77.[3]

The evaluation of the above integral can be carried out considering that the arguments of the exponential function are scalar quantities, thus the exponential of a sum can be written as the product of exponentials without concerns regarding the commutation of matrices.

[3] $\mathbf{T}_m$ and $\mathbf{C}_m$ are symmetric matrices, i.e. $\mathbf{T}_m^{\dagger} = \mathbf{T}_m$ and $\mathbf{C}_m^{\dagger} = \mathbf{C}_m$, thus the dagger symbol is omitted in the equation.

Hence:

$$\begin{aligned} f(\lambda) = -2^{N_{vib}}\theta \exp[-\Delta^{\dagger}\mathbf{T}_n\mathbf{A}^{-1}\mathbf{T}_m\Delta] \\ \times\mathbf{S}^{\dagger}\Big(\int d\mathbf{u}\exp[-(\mathbf{u}-\mathbf{m})^{\dagger}\mathbf{A}(\mathbf{u}-\mathbf{m})] \\ \times\int d\mathbf{v}\exp[-\mathbf{v}^{\dagger}\mathbf{B}\mathbf{v}][-\mathbf{C}_n\mathbf{v}\mathbf{v}^{\dagger}\mathbf{C}_m] \\ +\int d\mathbf{v}\exp[-\mathbf{v}^{\dagger}\mathbf{B}\mathbf{v}] \\ \times\int d\mathbf{u}\exp[-(\mathbf{u}-\mathbf{m})^{\dagger}\mathbf{A}(\mathbf{u}-\mathbf{m})][\mathbf{T}_n(\mathbf{u}-\Delta)\mathbf{u}^{\dagger}\mathbf{T}_m]\Big)\mathbf{S} \end{aligned} \tag{1.93}$$

with $\mathbf{A} = (\mathbf{T}_m + \mathbf{T}_n)$ and $\mathbf{B} = (\mathbf{C}_m + \mathbf{C}_n)$.
For the sake of simplicity, the two double integrals are considered separately; their explicit forms are defined below as I_a and I_b:

$$\begin{aligned} I_a = \int d\mathbf{u}\exp[-(\mathbf{u}-\mathbf{m})^{\dagger}\mathbf{A}(\mathbf{u}-\mathbf{m})] \\ \times\int d\mathbf{v}\exp[-\mathbf{v}^{\dagger}\mathbf{B}\mathbf{v}][-\mathbf{C}_n\mathbf{v}\mathbf{v}^{\dagger}\mathbf{C}_m] \end{aligned} \tag{1.94}$$

$$\begin{aligned} I_b = \int d\mathbf{v}\exp[-\mathbf{v}^{\dagger}\mathbf{B}\mathbf{v}] \\ \times\int d\mathbf{u}\exp[-(\mathbf{u}-\mathbf{m})^{\dagger}\mathbf{A}(\mathbf{u}-\mathbf{m})][\mathbf{T}_n(\mathbf{u}-\Delta)\mathbf{u}^{\dagger}\mathbf{T}_m] \end{aligned} \tag{1.95}$$

The evaluation of I_a is straightforward, since (see Appendix B):

$$\int \mathbf{x}\mathbf{x}^{\dagger}\exp[-\mathbf{x}^{\dagger}\mathbf{D}\mathbf{x}]d\mathbf{x} = \frac{1}{2}\pi^{N_{vib}/2}(\det\mathbf{D})^{-1/2}\mathbf{D}^{-1}; \tag{1.96}$$

thus:

$$I_a = \pi^{N_{vib}}(\det\mathbf{A})^{-1/2}(\det\mathbf{B})^{-1/2}\Big(-\frac{1}{2}\mathbf{C}_n\mathbf{B}^{-1}\mathbf{C}_m\Big) \tag{1.97}$$

The evaluation of I_b requires a change of variable. Let:

$$\mathbf{y} = \mathbf{u} - \mathbf{m} \qquad \mathbf{u} - \Delta = \mathbf{y} + (\mathbf{m} - \Delta) \tag{1.98}$$

Eq 1.95 is rewritten as:

$$\begin{aligned} I_b &= \int d\mathbf{v} \exp[-\mathbf{v}^\dagger \mathbf{B} \mathbf{v}] \\ &\times \int d\mathbf{y} \exp[-\mathbf{y}^\dagger \mathbf{A} \mathbf{y}][\mathbf{T}_n(\mathbf{y} + (\mathbf{m} - \Delta))(\mathbf{y} + \mathbf{m})^\dagger \mathbf{T}_m] \\ &= \int d\mathbf{v} \exp[-\mathbf{v}^\dagger \mathbf{B} \mathbf{v}] \\ &\times \int d\mathbf{y} \exp[-\mathbf{y}^\dagger \mathbf{A} \mathbf{y}][\mathbf{T}_n \mathbf{y}\mathbf{y}^\dagger \mathbf{T}_m + \mathbf{T}_n(\mathbf{m} - \Delta)\mathbf{m}^\dagger \mathbf{T}_m] \end{aligned} \tag{1.99}$$

whose integration leads to:

$$I_b = \pi^{N_{vib}} (\det \mathbf{A})^{-1/2} (\det \mathbf{B})^{-1/2} \left[\frac{1}{2} \mathbf{T}_n \mathbf{A}^{-1} \mathbf{T}_m + \mathbf{T}_n (\mathbf{m} - \Delta) \mathbf{m}^\dagger \mathbf{T}_m \right] \tag{1.100}$$

Given that

$$f(\lambda) = -2^{N_{vib}} \theta \exp[-\Delta^\dagger \mathbf{T}_n \mathbf{A}^{-1} \mathbf{T}_m \Delta] \mathbf{S}^\dagger (I_a + I_b) \mathbf{S} \tag{1.101}$$

substituting eq. 1.97 and 1.100 in eq. 1.101 the following equation of $f(\lambda)$ is obtained:

$$\begin{aligned} f(\lambda) &= \Theta \exp[-\Delta^\dagger \mathbf{T}_n \mathbf{A}^{-1} \mathbf{T}_m \Delta] \\ &\times \left(\mathbf{S}^\dagger \frac{1}{2} \left(\mathbf{C}_n \mathbf{B}^{-1} \mathbf{C}_m - \mathbf{T}_n \mathbf{A}^{-1} \mathbf{T}_m \right) \mathbf{S} \right. \\ &\left. + \mathbf{S}^\dagger \left(\mathbf{T}_n \mathbf{A}^{-1} \mathbf{T}_m \Delta \Delta^\dagger \mathbf{T}_n \mathbf{A}^{-1} \mathbf{T}_m \right) \mathbf{S} \right) \end{aligned} \tag{1.102}$$

with Θ defined in eq. 1.83.

By explicitly factorizing the non-adiabatic coupling operator arising from the action of the nuclear kinetic energy on the electronic wavefunctions, the electronic-nuclear interaction is decomposed into two distinct contributions. These correspond to a first-order derivative (momentum) coupling term and a second-order scalar coupling term, both explicitly dependent on nuclear coordinates and mediated by nuclear motion. Unlike conventional treatments, in which these contributions are either combined, approximated, or introduced phenomenologically, the present approach derives both terms systematically from first principles, preserving their distinct physical origins and roles in mediating electronic transitions.

The above treatment of the coupling terms, is novel and represents the hearth of this PhD dissertation. The treatment is completely general and can be applied to any case of non-radiative transition between two electronic states.

Chapter 2

Electron Transfer Reactions

Elementary electron transfer (ET) reactions are fundamental chemical processes in which no bond is formed or broken but an electron moves between a donor and an acceptor species. In its general form an ET can be represented as :

$$D + A \longrightarrow D^{+} + A^{-}$$

where D is the donor and A is the acceptor. They are ubiquitous in nature and technology, playing essential roles in a wide range of biological, chemical and physical phenomena, including photosynthesis, electrocatalysis, and molecular electronics. In the context of optoelectronic devices, such as OLEDs, OFETs, and OSCs, ET is the fundamental process which control device performances. crucial for charge separation, transport, and recombination.

A thorough understanding of the chemico-physical factors which control the kinetics of elementary ET processes, is essential for the rational design of efficient optoelectronic materials.[148, 83, 81] Theoretical studies offer deep insight into the mechanistic aspects governing ET, understanding reaction

rate in terms of driving forces, reorganization energies, and activation barriers. Among the most important contributions to the theory of ET reactions, there are the semi-classical models in which the ET reactions are described using classical nuclear motion and quantum electronic transitions, [105, 103] and their extension to include the quantized vibrational modes for high-frequency intramolecular vibrations.[69, 39, 92]

In the next sections will be described the two theoretical framework commonly used to describe ET reaction, the semi-classical Marcus' theory and the quantum mechanical treatment of Bixon and Jortner.[18, 68] Finally, it will be presented a simple generalization of Marcus theory that allows describing the ET reactions in solution through a multistep mechanism,[87, 79, 90, 91, 85] in which also the rates of solvent stabilization of a nonequilibrium charge distribution play an important role. In contrast to the standard Marcus and Bixon–Jortner formulations, which treat solvent and intramolecular nuclear motions within a single effective reaction coordinate, the present approach is based on an explicit adiabatic separation between solvent and intramolecular degrees of freedom. This separation allows the ET process to be described as a sequence of elementary steps, in which electronic transitions are coupled to both intramolecular nuclear dynamics and the rates of solvent stabilization of a nonequilibrium charge distribution. Within this framework, tunneling effects in solution are treated by explicitly including the full set of intramolecular nuclear coordinates of the redox pair. The theory naturally accounts for changes in equilibrium nuclear positions and vibrational frequencies upon electronic

transition, as well as for the effects arising from normal-mode mixing, thereby extending conventional treatments of nuclear tunneling in ET reactions.[23, 76, 88] Then, the model will be applied to a set of ET reactions in rigidly spaced donor-bridge-acceptor systems, for which ET rates and, in some cases, their temperature dependence have been experimentally determined in solvents of different polarity.[33] It will be shown that the results obtained reproduce quantitatively the experimental observations testifying the accurancy and vesatility of the proposed model and offering a mechanistically very clear picture of ET process in donor-acceptor systems.

2.1 Marcus' theory of ET

Marcus theory provides a fundamental description of how electrons are transferred between molecules in chemical and biological systems, emphasizing the interplay between electronic and nuclear dynamics. It identifies that the rate of an ET reaction is governed not only by the electronic interaction between the donor and acceptor species but also by how the surrounding molecular and solvent environment reorganizes in response to the change in charge distribution. When an electron moves from one molecule to another, the elecronic transition occurs almost instantaneously, yet the heavier nuclei of both molecules, and solvent respond much more slowly. Before the transfer can proceed efficiently, the nuclear configuration must adjust to a geometry where the energies of the reactant and product states

coincide. This rearrangement of the environmental gives rise to an activation barrier controlling the rate of the ET process.

Marcus formulated the problem by using potential energy surfaces and statistical mechanics to construct a physically transparent representation of the ET reaction. He demonstrated that if a change in the electronic charge distribution induces a proportional change in the solvent polarization (linear response approximation), then the many-dimensional free energy surfaces of reactants and products can be reduced to two harmonic parabolas defined along a single reaction coordinate x. For a self-exchange reaction, the free energies of the close-contact reactants (R) and products (P) appear as intersecting parabolic curves (Figure 2.1). Nuclear distortions of the system, comprising both solute and solvent, are described by identical force constants, and the minima of the parabolas are separated by $(2\lambda/f)^{1/2}$, where f is the reduced force constant for the parabolas and λ the vertical difference between the energies of the reactants and products at the reactant minimum for an ET reaction with zero standard free energy change. Introducing a dimensionless coordinate $X = x/a_0$ with x the reaction coordinate, and a_0 the separation of the minima, which varies from 0 to 1 during the reaction, the free energy gap between parabolas can be written as:

$$G_R - G_P = 2\lambda X - (\lambda + \Delta G^0), \tag{2.1}$$

At the transition state for the reaction where the parabolas intersect, $G_R = G_P$ and $X = (1 + \Delta G^0/\lambda)/2$ where ΔG^0 is the

standard free energy change for ET.

To compute these free energy curves rigorously, Marcus[104] and later Warshel and coworkers [62, 70] defined a reaction coordinate Q in the many-dimensional coordinate space defined by the configurations of the reactants, the products, and the surrounding medium. This coordinate Q represents the potential energy difference between the reactants plus the surrounding medium and the products plus the surrounding medium.

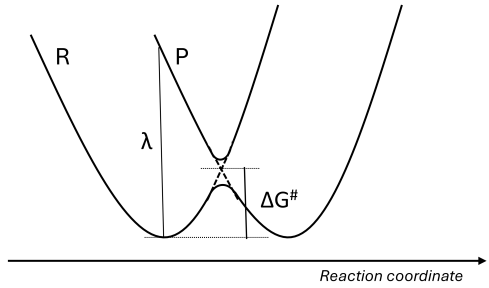

FIGURE 2.1: Free energy curves for the close-contact reactants (R) and close-contact products (P) of a self-exchange reaction plotted against the reaction coordinate. Adapted from Ref. [154]

Marcus expressed the rate constant for bimolecular ET as:

$$k = A \exp(-\Delta G^{\#}/RT) \tag{2.2}$$

where A is equal to the vibrational partition function Z multiplied by a correction for the electrostatic work required to bring the separated reactants together, and $\Delta G^{\#}$ is the free energy of activation for the ET with the two reactants in contact which,

under the intersecting parabola model, is given by:

$$\Delta G^{\#} = \frac{(\Delta G^0 + \lambda)^2}{4\lambda} \tag{2.3}$$

The reorganization energy λ is composed of solvational λ_s and intramolecular λ_i components,

$$\lambda = \lambda_s + \lambda_i \tag{2.4}$$

and represents the cost of distorting the nuclear coordinates of both the inner coordination sphere (bond lengths, angles) and the outer solvent shell from their equilibrium positions in the reactant state to those appropriate for the product, without transferring the electron itself.

Marcus combines this thermodynamic picture with a non adiabatic rate expression based on FGR, yielding the rate constant for ET:

$$k_{ET} = \frac{2\pi}{\hbar}|V|^2 \frac{1}{\sqrt{4\pi\lambda k_B T}} \exp\Big(-\frac{(\Delta G^0 + \lambda)^2}{4\lambda k_B T}\Big) \tag{2.5}$$

with V the electronic coupling between the donor and acceptor states, which quantifies the strength of their electronic interaction and determines the probability of tunneling of the electron. The pre-exponential term arises from classical nuclear fluctuations and includes the quantum-mechanical transition probability and the statistical distribution of the solvent, while the activation barrier $(\Delta G^0 + \lambda)^2/(4\lambda)$ enters the Arrhenius-like exponential factor expressing the probability that the system

will reach the nuclear configuration at which ET can occur.

The Marcus expression (eq. 2.5) predicts a characteristic dependence of the ET rate on the reaction free energy. In the so-called normal region, where the driving force ΔG^0 is moderately negative, increasing the exergonicity lowers the activation barrier, leading to an increase in k_{ET}. However, once the driving force exceeds the reorganization energy ($\Delta G^0 < -\lambda$), the barried begins to rise again, leading to a decrease in rate despite the reaction being more exergonic. This counterintuitive regime, known as the inverted region, constitutes the central and most profound result of Marcus theory. Its existence, confirmed by numerous experiments, overturned the prevailing belief that ET rates always increase with exergonicity.

Physically, Marcus theory provides a bridge between thermodynamics and kinetics: the parameters ΔG^0 and λ describe equilibrium energetic landscapes, while V and T determine how rapidly the system can traverse them. The theory successfully rationalizes the influence of solvent polarity, temperature, and molecular structure on ET rates. Its assumptions, however, impose certain limits. Due to the classical approach used to describe nuclear motion, Marcus' rate equation often fails to accurately capture the temperature dependence observed in ET rates leading a significant discrepancies in the calculated rate constants. In system where nuclear motions exhibit strong quantum effects, where solvent dynamics are non-linear, or where high-frequency vibrational modes play a major role, the classical assumption of Marcus theory break down. As a result, the theoretical rate constants obtained from the Marcus expression

can either overestimate or underestimate experimental values of many orders of magnitude,[107] especially at low temperatures or in regimes dominated by quantum nuclear tunneling. There are notable exceptions where this discrepancy is resolved by including the temperature dependence of both the reorganization energy and the reaction free energy.[168] However, this limitation creates challenges for gaining a deeper understanding of key mechanistic details in various processes, such as charge transport in organic semiconductors, where tunneling likely plays a significant role.

Despite the limitations, Marcus theory remains the cornerstone of modern ET kinetics. It offers both a clear conceptual picture and a relatively simple predictive formula that connects molecular structure, energetics, and reactivity.

2.2 Quantum effects in classical ET theory

As discussed in the previous section, Marcus theory is a classical model assuming harmonic potential surfaces and thermal activation over the reorganization barrier. One of the limitation is the classical treatment of all nuclear modes, which is valid when all relevant vibrations are low-frequency. In the classical limit, i.e. when $\hbar\omega_s << k_B T$, with ω_s the characteristic frequency of solvent modes, the rate constant expression (eq. 2.5) has the usual Arrhenius-type temperature dependence. However, a

weak temperature dependence was documented for the primary ET process in the reaction center of some photosynthetic bacteria[44, 71] being also ubiquitous for other ET processes in the reaction center.[72] Furthermore, a weak temperature dependence of ET rates in polar solvents was also documented for some bridged compounds.[94, 95] Such a regime is achieved when nuclear tunneling becomes dominant.[58] It was noted that intramolecular high-frequency vibrational modes, such as C-C or C-H stretches, are not thermally accessible at room temperature, and so necessitate a quantized treatment. These quantum effects not only modify free energy relationships for ET[111, 110] but also exert a dramatic effect on the temperature dependence of ET rates.

Accordingly, Jortner and Bixon[68, 18, 19] extends the Marcus theory by incorporating quantized intramolecular vibrational modes on top of the classical solvent reorganization. The high-fequency quantum modes are represented by a single (average) vibrational mode ω with $\hbar\omega >> k_B T$, and an electron-vibrational coupling $S = \Delta_c^2/2$ with Δ_c the change in the equilibrium configuration for this mode expressed in units of the root-mean-square displacement at the zero-point energy.

The high-frequency intramolecular vibrational excitations of the donor and acceptor centers provide a multitude of parallel channel involving vibrational excitations of these modes, which are induced by ET. The expression of k_{ET} is modified to the form:

$$k_{ET} = A \exp(-S_c) \sum_{n=0}^{\infty} \frac{S_c^n}{n!} \exp\left[- \frac{(\Delta G + n\hbar\omega + \lambda_s)^2}{4\lambda_s k_B T} \right] \quad (2.6)$$

$$A = (2\pi\lambda_s k_B T)^{-1/2} \tag{2.7}$$

with n the indexes of the number of vibrational quantum excited in the ET process. Each term in the summation corresponds to a specific vibronic transition, with the Gaussian factor describing activation over the classical solvent reorganization barrier.

The high-frequency modes modify the ET dynamics by (i) reducing the effective free energy gap in the inverted region ($\Delta G < -\lambda_s$),[110, 33] and (ii) reducing the average activation energy in the inverted region.[94, 69]

Several conclusions can be drawn about the role of high-frequency vibrational excitations in ET within the inverted region. Even weak electron-vibrational coupling S can substantially alter the temperature dependence of ET rates.[19] In polar solvents with large λ_s, ET becomes pratically activationless for moderate S whereas in low λ_s environments such as protein media or nonpolar solvents, nearly activationless ET can occur for weaker coupling S over a broad range of $-\Delta G/\lambda_s$.

In summary, the quantum-mechanical extension of Marcus theory incorporates high-frequency vibrational modes and nuclear tunneling extending the region of activationless behavior and corrects the classical model's failure to reproduce the experimentally observed non-Arrhenius temperature dependence of ET rates. This quantum treatment also provides a more accurate description of the rate behavior in the strongly exergonic regime, where classical Marcus theory predicts a rate with many order of magnitude different from the experimental observations.

Nonetheless, this formalism still relies on simplifying assumptions, such as discrete mode coupling, weak electronic

coupling, and the neglect of full vibrational relaxation dynamics. Moreover, it lacks a systematic procedure for evaluating solvent reorganization energies and for selecting the relevant high-frequency vibrational modes, limiting its predictive capability. Addressing these limitations remains a key challenge, highlighting the need for a unified framework that integrates classical concept with a full quantum-mechanical treatment of nuclear motion in ET.

The following section presents a detailed formalism in which the quantum-mechanical treatment of ET is extended to incorporate the full vibrational relaxation dynamics of the nuclear environment. This extension allows for a more rigorous and comprehensive description of ET processes, providing a predictive approach that not only reproduces the experimental temperature dependence of ET in both polar and non polar environments but also provides rate predictions consistent with experimental values even in strongly exergonic regimes.

2.3 ET beyond Marcus theory: full quantum model

Although various important studies have extended Marcus' theory,[92, 39, 69, 18, 177, 151] a full treatment that incorporates the entire heat bath originated by the intramolecular motions of the redox pair has not yet been applied to systems where polar solvents are likely to play a significant role. The inclusion of the whole set of intramolecular modes of the redox pair

was the crucial factor which allowed to reproduce the atypical temperature dependence of ET from bacteriopheophytin anions to primary ubiquinone in bacterial reaction centers.[23, 138, 71]

Modeling ET as a multistep kinetic process establishes a framework suitable for incorporating quantum tunneling effects involving the complete set of nuclear coordinates. This approach is based on the assumption that the elementary ET step inherently proceeds via tunneling and its rate can be reliably computed via first-order time-dependent perturbation theory provided that solvent dynamics are decoupled from the internal nuclear motions of the redox pair.

The multistep character of the kinetic process originates from this adiabatic separation of solvent and nuclear motions. Initially, solvent reorganization proceeds with the intramolceular coordinates effectively fixed, driving the donor-acceptor pair toward a configuration in which ET becomes energetically accessible. Once the solvent-controlled configuration is established, a subsequent adjustment of nuclear coordinates at fixed solvent configuration promotes the ET process. The constraint of fixed (or frozen) solvent coordinates during this step reduces the effective free energy change associated with the reaction, thereby facilitating the ET. In this framework, solvent motions establish the resonant condition, whereas nuclear motions ultimately governs the transfer step under a reduced effective driving force.

Let us denote by Q a generalized coordinate which represent the collective motion of the solvent and by $\mathbf{q}$ the vector of intramolecular coordinates. Following Marcus' assumptions that

the potential energy surfaces of the initial and final states are quadratic diagonal functions in Q and $\mathbf{q}$, the potential energy for initial and final states can be written as:

$$V_i(\mathbf{q}, Q) = \frac{1}{2}\mathbf{q}^{\dagger} a \mathbf{q} + \frac{1}{2} K Q^2 \tag{2.8}$$

$$V_f(\mathbf{q}, Q) = \frac{1}{2}(\mathbf{q} - \mathbf{q}_{0f})^{\dagger} b (\mathbf{q} - \mathbf{q}_{0f}) + \frac{1}{2} K (Q - Q_{0f})^2 + \Delta G^0_{fi} \tag{2.9}$$

where $\mathbf{q}_{0f}$ and Q_{0f} denote the position of the minima in the final state, the quantities $\frac{1}{2}\mathbf{q}^{\dagger}_{0f} b \mathbf{q}_{0f}$ and $\frac{1}{2} K Q^2_{0f}$ represent the intramolecular reorganization energy, λ_i, and the solvent reorganization energy, λ_s, respectively, and ΔG^0_{fi} is the standard free energy change. From eq. 2.9 it is easily seen that if ET occurs by tunneling at Q=0 the effective free energy change is:

$$\Delta G^0_{eff} = \Delta G^0_{fi} + \lambda_s. \tag{2.10}$$

Eq. 2.10 encloses a fundamental aspect of the proposed model: for strongly exothermic ET processes and/or for low solvent stabilization energy, initial and final states are in vibronic resonance and ET can occur by tunneling at frozen solvent coordinates.

In contrast, when the solvent stabilization energy is larger than the free energy change of the ET, the activation of tunneling requires environmental nuclear motion.

For solvent activated ET, the activation energy is found by imposing the condition $V_i(Q_c, \mathbf{q}) = V_f(Q_c, \mathbf{q})$ at $\mathbf{q} = 0$. That is:

$$\frac{1}{2}\mathrm{K}\mathrm{Q}_c^2 = \lambda_i + \frac{1}{2}\mathrm{K}(\mathrm{Q}_c - \mathrm{Q}_{0f})^2 + \Delta G^0_{fi} \tag{2.11}$$

$$\mathrm{Q}_c = \frac{\Delta G^0_{eff} + \lambda_i}{\mathrm{K}\mathrm{Q}_0}, \tag{2.12}$$

and

$$\Delta G^{\#} = \frac{1}{2}\mathrm{K}\mathrm{Q}_c^2 = \frac{(\Delta G^0_{eff} + \lambda_i)^2}{4\lambda_s} \tag{2.13}$$

Noteworthy, $\Delta G^{\#}$ is higher than in Marcus' theory, because of the assumption that only solvent coordinates are involved in the activation step.

The multistep mechanism is shown in Scheme 1, where $\mathrm{D}^-\mathrm{A}$ and DA^- denote the initial and final states, respectively, and $\{\ \mathrm{D}^-\mathrm{A}\}^*$ and $\{\ \mathrm{DA}^-\}^*$ denote the ensembles of transient structures in vibronic resonance with each other.

Scheme 1. Multistep Kinetic Machanism of ET

$$\mathrm{D}^-\mathrm{A} \underset{k_{\mathrm{dact}}}{\overset{k_{\mathrm{act}}}{\rightleftharpoons}} \{\mathrm{D}^-\mathrm{A}\}^* \underset{k_{\mathrm{ET}}}{\overset{k_{\mathrm{ET}}}{\rightleftharpoons}} \{\mathrm{DA}^-\}^* \underset{k_{\mathrm{act}}}{\overset{k_{\mathrm{dact}}}{\rightleftharpoons}} \mathrm{DA}^-$$

Step 1 is an activation step which brings the donor and acceptor species into electronic degeneracy; it is assumed that its rate constant has the usual Arrhenius dependence on temperature :

$$k_{act} = k_0 \exp\left(-\frac{\Delta G^{\#}}{k_B T}\right) \tag{2.14}$$

where k_0 is a transmission coefficient. Backward step 1 and forward step 3 involve the solvent response to a solute non-equilibrium charge distribution. These processes have been thoroughly investigated using time-dependent spectroscopic techniques, and their rates have been measured experimentally.[146, 101]. The relationship between k_0 and k_{dact} is governed by the principle of microscopic reversibility, which must hold for the activation step. This principle applies even though equilibrium or steady-state conditions are not assumed, as it arises from the fundamental mechanical symmetry of the equations of motion under time reversal.[99, 78] According to the principle of microscopic reversibility, the following relationship holds between k_{act} and k_{dact} , averaged across all the possible paths bringing degenerate reactants into degenerate products:[99]

$$k_{act} = k_{dact} \frac{g_{act}}{g_{eq}} \exp\left(-\frac{\Delta G^{\#}}{k_B T}\right), \tag{2.15}$$

where g_{act} and g_{eq} are the total degeneracies of the activated and the equilibrium states. The above condition implies:

$$k_0 = k_{dact} \frac{g_{act}}{g_{eq}}. \tag{2.16}$$

Since the degeneracy factors g_i cannot be easily estimated, k_0 is the only solvent dependent adjustable parameters to be fixed by comparison with experimental rates.

Step 2 is the elementary ET process under resonant conditions ($\Delta E = 0$), whose rate can be reliably calculated by FGR as

shown in Chapter 1. Recall the eq. 1.46 :

$$K_{f\longleftarrow i} = \frac{2\pi}{\hbar} F(\Delta E, T) = \frac{2\pi}{\hbar} \sum_{\mu} \sum_{\nu} |\hat{\mathcal{H}}'_{n\nu,m\mu}|^2 w_{m\mu}(T) \delta(E_{n,\nu} - E_{m,\mu} - \Delta E_{n\nu,m\mu}) \tag{2.17}$$

By making the reasonable assumption that the dependence of the electronic coupling elements on vibrational coordinates can be neglected, $F(\Delta E, T)$ simplifies to :

$$F(\Delta E, T) = |V_{fi}|^2 \rho(\Delta E, T) \tag{2.18}$$

where $\rho(\Delta E_{fi}, T)$ is the Franck-Condon weighted density of states of the elementary $|i\rangle \rightarrow |f\rangle$ transition averaged over a thermal equilibrium distribution of initial vibrational states.

In the case of ET between two weakly interacting molecules, assuming that the vibrational motions at each molecular site during the ET are independent, the distribution $\rho(\Delta E, T)$ for the ET process $D^- + A \rightarrow D + A^-$ can be obtained by the convolution of the ρs of the two redox half reactions $D^- \rightarrow e^- + D$ and $A + e^- \rightarrow A^-$:

$$\rho(\Delta E, T) = \int_{-\infty}^{\infty} dE \mathcal{D}(E) \mathcal{A}(\Delta E - E). \tag{2.19}$$

In the equation above, $\mathcal{D}(E)$ and $\mathcal{A}(E)$ are the spectral distributions of the photoelectronic spectrum of the donor and the attachment spectrum of the acceptor.[58, 22] Both $\mathcal{D}(E)$ and $\mathcal{A}(E)$ are experimentally accessible quantities,[128, 166, 30] and both can also be reliably obtained by first principle calculations.[114,

136, 123, 23, 22]

An important conclusion emerging from the preceding analysis is that, within the solvent-stabilization picture, ET always occurs at frozen solvent coordinates; however, whether or not the reaction requires activation depends on the accessibility of this solvent configuration.

In the activationless regime, the ET rate is obtained directly from FGR (eq. 1.46). In this case, the rate exhibits negligible temperature dependece, since the FCWD depends predominantly on intramolecular vibrational modes with characteristic frequencies much larger than $k_B T$. As a result, their thermal population remains essentially constant over typical experimental temperature ranges. Consequently, changes in temperature do not significantly modify the FCWD, and the ET rate remains effectively invariant.

In contrast, when the system requires an activation step to reach the solvent-frozen configuration at which ET can occur, the overall kinetics become inherently multistep. Although the elementary ET event is still described by FGR, the overall rate constant must be derived from the coupled system of differential equations corresponding the multistep reaction scheme. In this regime, the rate-determining step is usually the solvent-driven activation process. Because this activation step follows Arrhenius behavior, its temperature dependence dominates the overall kinetics, imparting an Arrhenius-like temperature dependence to the ET rate. Thus, any observed temperature dependence originates from the thermally activated solvent reorganization preceding the electronic transition, rather than

from the ET step itself.

Before applying the proposed kinetic model, it is essential to establish whether ET requires solvent activation, a conclusion that critically depends on the accurate determination of λ_s, see eq. 2.10. This parameter is pivotal to the model, as it governs the role of solvent dynamics in modulating the ET process. Several approaches are available for estimating this quantity as the Born-Onsager model,[105] molecular dynamics simulations,[167, 120] the non equilibrium polarizable continuum model[147] and microscopic theory of solvent response.[168]

2.4 Intramolecular ET in rigdly bridged donor-acceptor systems

The multistep kinetic model presented in the previous section is applied to the calculation of the rates of intramolecular ET reactions in donor (D) and acceptor (A) systems rigidly spaced by androstane molecule in three solvents, iso-octane, tetrahydrofuran (THF), and dibutylether (DBE) for which experimental measurements are available.[33, 110] The chemical structures of D, the biphenyl radical anion, and the five A molecules investigated are depicted in Figure 2.2. The energies of initial D^-A and final DA^- states have been computed at DFT level using the continuum polarizable medium (PCM) approach for evaluating the contribution of solvent polarization. The results for iso-octane, THF, and DBE are presented in Table 2.1. As shown in Figure 2.3, calculated electronic energy difference for

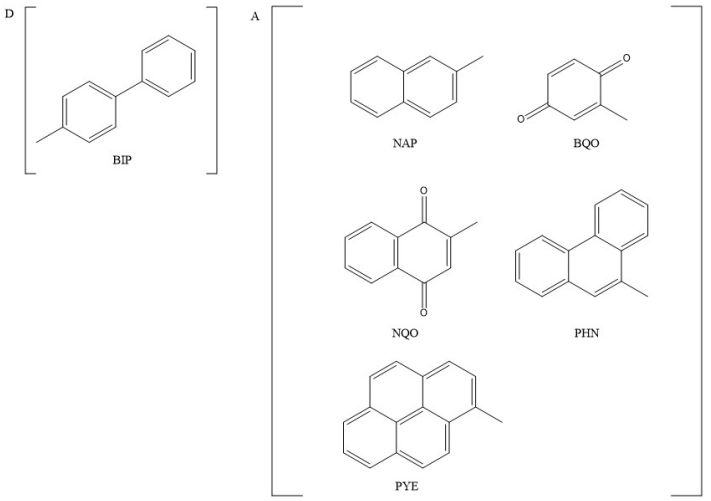

FIGURE 2.2: Donor and acceptors group: BIP=1,1-biphenyl, BQO=2-benzoquinonyl, NAP=2-naphthyl, NQO=2-naphtoquinonyl, PHN=9-phenanthryl, PYE=1-pyrenyl. Donor and acceptor groups are bridged through the Androstane molecule.

ET from D to each A are in good agreement with the experimental free energies (ΔG^0). Throughout this section, ΔE_{fi} values are treated as free energies, assuming negligible intramolecular vibrational entropy, [153] while solvent entropy contributions are incorporated via λ_s.

When both the solvent (Q) and the molecular ($\mathbf{q}$) nuclear coordinates are in their equilibrium conditions, all ET reactions are exothermic. In the proposed kinetic model, however, the ET step occurs at a fixed solvent configuration, either at Q_{0i} corresponding to the equilibrium solvent coordinate of the initial

state, where

$$\Delta G^0_{eff} = \Delta G^0_{fi} + \lambda_s. \tag{2.20}$$

or at Q_c, the point where the potential energy surfaces of the initial and final states intersect while intramolecular coordinates remain fixed at their initial equilibrium values. Accordingly, λ_s is determined first, as it dictates whether the ET involves solvent activation. Taking advantage of available experimental ET rates at different ΔG, λ_s is directly determined from the rate constants of the highly exothermic BIP–BQO and BIP–NQO pairs, using the electronic coupling elements reported in Ref. [120] assuming—easily verified a posteriori—that these ET processes do not require solvent activation. From eqs 2.17 and 2.18, in THF the observed rate constant for the BIP-BQO pair is reproduced with two different value of ΔG^0_{fi}, one corresponding to $\Delta G^0_{eff} = 720$ cm^{-1} and the other to 12310 cm^{-1}. The latter is disregarded because it would lead to vanishingly small ET rates for all of the other acceptors ($\lambda_s \simeq 2.1$ eV), the former is physically sound and leads to $\Delta G^0_{eff} = -1.53$ eV and $\lambda_s = 0.86$ eV. The same procedure for BIP-NQO pair leads to $\lambda_s = 0.63$ eV. With the limitation that λ_s does not depend on the specific acceptor,[120] averages between the λ_s of the two exothermic pairs yields for THF $\lambda_s = 0.75$ eV. The same procedure for DBE solvent leads to an averaged $\lambda_s = 0.53$ eV.

The estimated solvent reorganization energies are in good agreement with those reported by Parson from quantum mechanics/molecular dynamics (QMMD) simulations,[120] and closely match the values obtained by Closs and coworkers, who

fitted experimental data in THF using a Marcus-type rate expression with a single high-frequency quantum mode.[33]

Table 2.1: Standard free energy changes for ET in each BIP-br-A pair in iso-octane, THF and DBE; all energies are in eV.

	ISO-OCTANE	**THF**			**DBE**		
A	$\Delta G^0_{fi} = \Delta G^0_{eff}$	ΔG^0_{fi}	ΔG^0_{eff}	$\Delta G^{\#}$	ΔG^0_{fi}	ΔG^0_{eff}	$\Delta G^{\#}$
BQO	-2.4	-2.4	-1.6	-	-2.4	-1.8	-
NAP	0.0	-0.03	+0.7	+0.2	0.0	+0.6	+0.2
NQO	-2.1	-2.1	-1.3	-	-2.1	-1.6	-
PHN	-0.2	-0.1	+0.6	+0.2	-0.1	+0.5	+0.2
PYE	-0.6	-0.5	+0.3	+0.04	-0.6	+0.03	+0.01

For the nonpolar iso-octane solvent, the above procedure yields λ_s's vanishingly small for all redox pairs, as it occurs in photosynthetic reaction centers,[21] so that in iso-octane, $\Delta G^0_{eff} = \Delta G^0_{fi}$. Under these conditions, ET proceeds without requiring thermally activated solvent reorganization, and the ET event is effectively activationless. Consequently, the rate for each D–A pair is computed directly using FGR, with the ET dynamics independent of solvent-induced activation barriers.

All the calculated rate constants in iso-octane are reported in Table 2.2, together with experimental ones. For NQO, the calculated ET rate significantly disagrees with the experimental value, but, as already noted in previous papers,[33, 120, 94] this strongly exergonic ET process could also involve an electronically excited state. Indeed, if the ET rate is evaluated at ΔG^0_{fi} corresponding to the first excited states of NQO anion, obtained

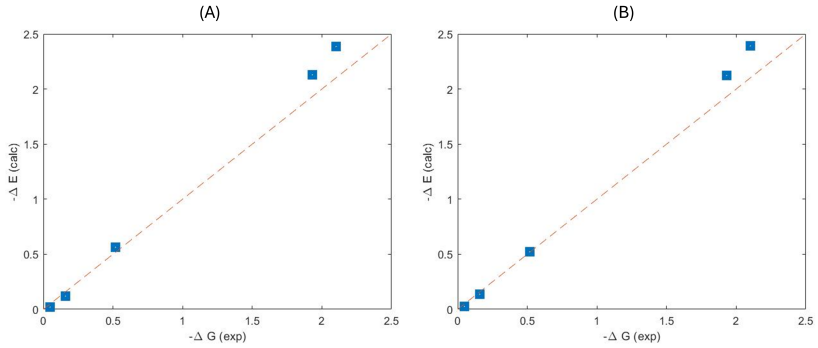

FIGURE 2.3: Calculated energy differences for ET from BIP^- to NAP, PHN, PYE, NQO and BQO (in order of increasingly negative ΔE) against experimental ΔG values in DBE (A) and THF (B). All energies in eV

by TDDFT computations, keeping fixed the electronic coupling element, a reasonable agreement with the experimental value is found, see Table 2.2.

According to TDDFT results, also ET from BIP to BQO could involve the first electronically excited state of BQO, but in this case better agreement with the experimental rate is obtained for ET into the ground state, see Table 2.2.

For the A/D systems studied in THF and DBE, the effective free energy change ΔG^0_{eff}, varies across cases highlighting the combined influence of reaction energetics and solvent reorganization. In particuolar, for the BQO and NQO acceptors, $\Delta G^0_{eff} < 0$ in both solvents, reflecting strongly exergonic reactions that proceed without any activation, and the corresponding ET rates follow directly from the FGR expression. For the

remaing three acceptor groups, the solvent reorganization energy exceeding the intrinsic driving force ($\Delta G^0_{eff} > 0$), requiring activation. The ET rates are therefore obtained using Pauli's master equation approach, by solving the differential equations associated with the kinetic scheme presented above. The kinetic constants k_{act} and k_{ET} are calculated from eqs 2.14 and 2.18 with $\Delta G^{\#}$ from eq. 2.13, while k_{deact} is taken from time-resolved spectroscopic measurements : $k_{deact} = 7 \times 10^{11} s^{-1}$ in THF and $8 \times 10^{10} s^{-1}$ in DBE. [146]

Table 2.2: Experimental and calculated ET rate constants for each BIP-br-A pair in iso-octane, THF and DBE. All constants are in s^{-1}.

	ISO-OCTANE		**THF**		**DBE**	
A	Exp	Theo	Exp	Theo	Exp	Theo
BQO	3.6±0.8e+06	5.4e+06 1.0e+08[a]	2.5±0.3e+08	1.4e+08	3e+07	1.9e+07
NAP	1.5±0.5e+09	2.6e+09	1.5±0.5e+06	2.6e+06	2e+07	3.4e+07
NQO	>2e+09	2.9e+06 4.4e+09[a]	3.8±1e+08	8.3e+08	2e+08	2.9e+08
PHN	>2e+09	1.9e+09	1.25±0.2e+07	1.3e+07	4e+08	5.5e+07
PYE	>2e+09	1.3e+10	1.5±0.5e+09	2.9e+09	-	6.4e+09

Notes: [a] corresponding to ET into the first excited state of A.

Each elementary ET step that occurs at electronic degeneracy is intrinsically fast ($k_{ET} \sim 2.0\,x10^9\ s^{-1}$). However, increasing the activation barrier slows the effective rate of the overall process. For the NAP and PHN acceptors, the activation rate and the elementary ET rate are of the same order of magnitude ($\sim 10^9\ s^{-1}$), whereas the relaxation of the activated product is significantly

faster ($\sim 10^{11}$ s^{-1}). Under these conditions, population analysis (see Figure 2.7) shows no detectable accumulation of either intermediate $\{D^{-}A\}^{*}$ or $\{DA^{-}\}^{*}$. Once activation occurs, the system undergoes ET and then relaxes essentially irreversibly. Thus, despite the ET being intrinsically fast, the activation step is rate determining because all subsequent processes proceed rapidly and without significant back reaction on the observed timescale. The fast relaxation funnels the system directly to the final DA^{-} state.

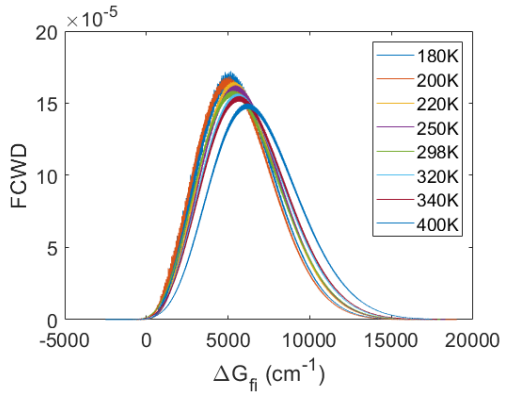

FIGURE 2.4: FCWDs of BIP-BQO pair at different values of T.

By contrast, the PYE acceptor exhibits a different kinetic regime. Here, activation is much faster ($\sim 10^{12}$ s^{-1}) than the ET step ($\sim 10^{9}$ s^{-1}), and the relaxation rate ($\sim 10^{11}$ s^{-1}). As a result, the intermediate $\{D^{-}A\}^{*}$ accumulates to observable levels because activation quickly populates this state but ET cannot deplete is at the same rate. Meanwhile, $\{DA^{-}\}^{*}$ does

not accumulate because its relaxation is still very fast. Consequently, for PYE, the elementary ET step is the rate determining step.

Calculated ET rate constants in THF and DBE are summarized in Table 2.2 together with the corresponding experimental values, and are also illustrated in Figure 2.5, where both theoretical and experimental rates are plotted as a function of the driving force (ΔG^0) of the ET reactions.

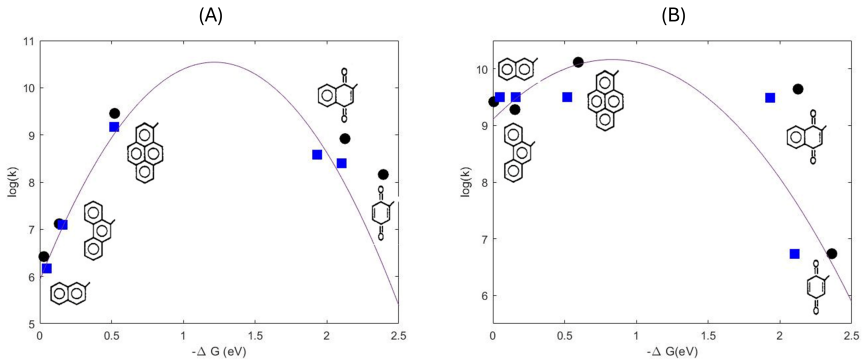

FIGURE 2.5: Calculated (black circles) and experimental (blue squares) ET rate constants in (A) THF and (B) iso-octane for each DA pair.

The theoretical data confirmed the experimental characteristic trend: as ΔG^0 decreases, the ET rates initially increase, reaching a maximum, and then decline in the so-called Marcus inverted region, where further decreases in ΔG^0 lead to slower ET rates.

Taken together, these results demonstrate that the kinetic model successfully captures both mechanistic regimes. By explicitly accounting for activation, forward and backward ET,

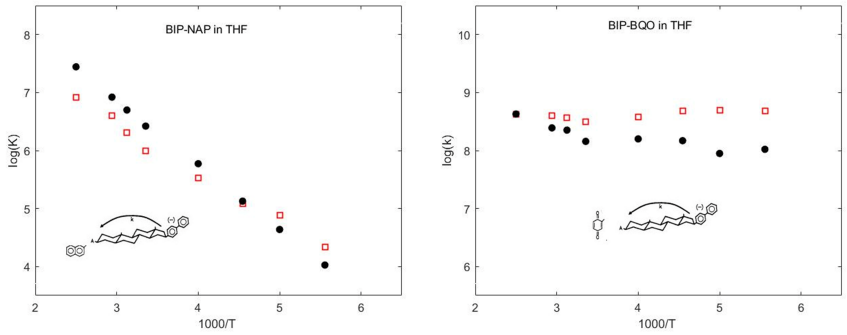

FIGURE 2.6: Calculated (black circles) and experimental (red empty squares) temperature-dependence of ET rate constant from BIP^- to BQO (right) and NAP (left) in THF. The dependence of dielectric constant on temperature, has been neglected.

and rapid relaxation within a unified scheme, the model reproduce the distinct population dynamics associated with either an activation-limited or ET-limited process. The fact that a single kinetic scheme robustly accounts for these distinct limiting behaviors underscores its predictive reliability and confirms that the relative magnitudes of k_{act}, k_{ET}, and k_{dact} fully determine the mechanistic outcome across the series of acceptors.

The temperature dependence of ET rates serves as a decisive criterion for distinguishing between tunneling and activation-controlled mechanisms; consequently, its analysis is essential for validating the proposed models. Given that only for two acceptors, BQO and NAP in THF, experimental data are available,[94, 95] the temperature dependence of ET have been calculated. In the BIP/BQO pair, where $\Delta G^0_{eff} < 0$, ET proceeds without

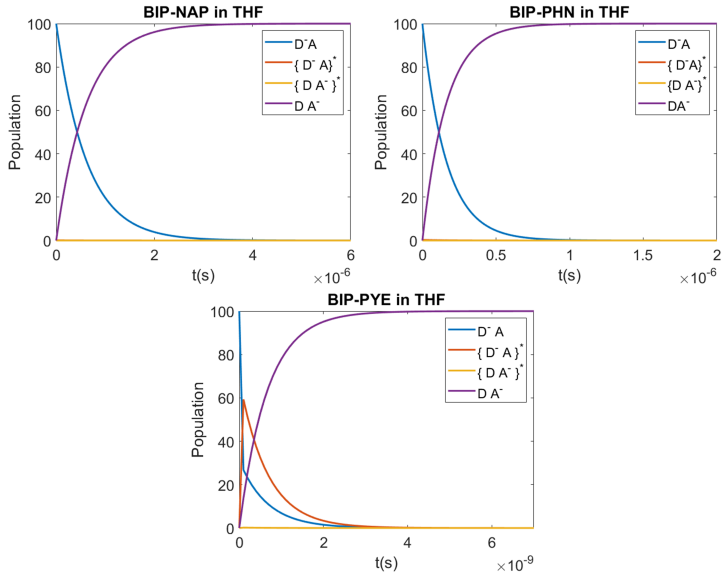

FIGURE 2.7: Population analysis of the multistep ET process for the NAP, PHN, and PYE acceptors.

solvent activation, whereas in the BIP/NAP pair, solvent reorganization is required to enable ET.

The calculated temperature-dependent rates (Figure 2.6) clearly demonstrate the fundamental difference between these processes: ET from BIP to NAP exhibits a pronounced Arrhenius-type behavior, with the rate constant varying by more than four orders of magnitude between 180 and 400 K. In contrast, ET from BIP to BQO occurs predominantly through tunneling, and owing to the weak temperature dependence of $F(\Delta E, T)$, the

rate is essentially temperature independent (Figure. 2.4).

2.4.1 Implicit modeling of solvent reorganization energy

The direct experimental determination of the solvent reorganization energy (λ_s) is challenging, and only a few indirect approaches are available. These include the analysis of charge-transfer absorption bands, photoelectron and electron attachment spectra, dynamic Stokes shifts, or the fitting of emission spectra using Marcus theory. While internal reorganization energies can be accurately obtained from quantum mechanical (QM) calculations, the computational estimation of λ_s remains more difficult.

Accurate modeling of the external reorganization energy is particularly important for understanding ET in condensed phases. Neglecting or poorly approximating this term can lead to significant discrepancies between theoretical predictions and experimental data, as well as to misinterpretations of the solvent's role in the ET process and of the temperature dependence of the reaction. To overcome these challenges, several computational methods have been proposed, most of which rely on an implicit representation of the solvent. Among these, the widely used polarizable continuum model (PCM)[157] and Marcus' non-equilibrium formalism[105] describe the solvent as a continuous dielectric medium containing a cavity in which the solute is placed. These continuum models typically provide reasonable estimates for highly polar solvents and ionic liquids, often in qualitative agreement with MD simulations that treat the solvent molecules explicitly.

In the preceding section, the solvent reorganization energy (λ_s) in THF was estimated directly from the experimental rate constants of the highly exothermic BIP–BQO and BIP–NQO donor–acceptor pairs (Figure 2.2), together with the electronic coupling elements reported in Ref. [120]. This procedure yields λ_s values that are nearly independent of the acceptor's chemical nature. Although this approximation provides satisfactory results for the investigated donor–acceptor pairs, it may not be reliable for other systems. Moreover, this methodology limits the applicability of the model to cases where λ_s can be derived from experimental measurements, thereby reducing its predictive capability. Here are presented the results obtained in

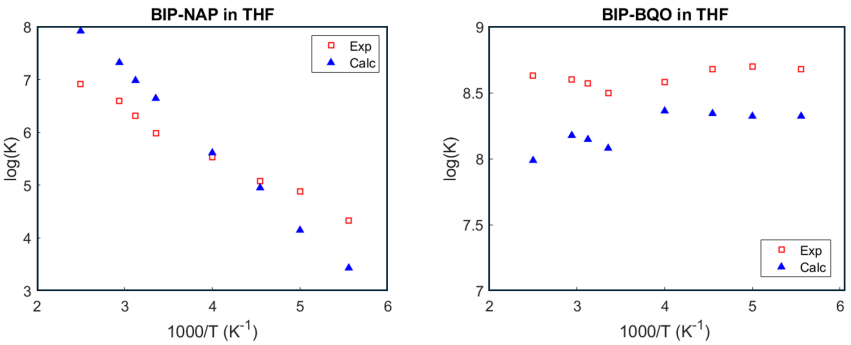

FIGURE 2.8: Experimental (red squares) and calculated (blu triangles) temperature dependence of rate constat for BIP-NAP (left) and BIP-BQO (right) pairs in THF.

personal research (Ref. [91]) in which the solvent reorganization energy, λ_s, is computed using an implicit solvent model based on Marcus' non-equilibrium formalism.[105, 91]In this approach, the solvent is represented as a continuous polarizable

medium characterized by its macroscopic dielectric properties, allowing the solvent response to be included without explicit modeling of individual solvent molecules. Within this framework, the solvent reorganization energy is expressed as:

$$\lambda_s = (ne)^2\Big(\frac{1}{2r_A} + \frac{1}{2r_D} - \frac{1}{R}\Big)\Big(\frac{1}{\epsilon_\infty} - \frac{1}{\epsilon_0}\Big), \tag{2.21}$$

where n denotes the number of electrons exchanged, e is the elementary charge, r_A and r_D are the radii of cavity accommodating the donor and acceptor, respectively, R the intermolecular distance, ϵ_∞ and ϵ_0 the high-frequency and static dielectric constants of the solvent, respectively. Using the solvent energies computed here, the rate constants for all A/D pairs discussed previously are calculated, restricting the analysis to THF as the solvent. As shown in Table 2.3, the computed rate constants differ from the experimental values by a factor of approximately 2–3, while correctly reproducing the order of magnitude in all cases. These results further corroborate the validity of the proposed model and demonstrate that the theoretical approach presented in Section 2.3 can provide a reliable estimation of ET rates beyond systems for which λ_s can be directly inferred from experiment. Figure 2.8 reports the temperature dependence of ET for the two acceptors with available experimental data, BQO and NAP. As noted previously, ET from BIP to NAP is strongly temperature dependent due to solvent-activated motion, while ET to BQO occurs primarily by tunneling and is nearly temperature independent. In this analysis, the temperature dependence of the THF dielectric constant, expressed as

Table 2.3: Calculated equilibrium energy changes (ΔG^0_{fi}), reorganization energies (λ_s), activation free energy ($\Delta G^{\#}$), and rate constants (k) for ET of each BIP-A pair. All energies are in eV.

Acceptor	ΔG^0_{fi}	λ_s Equation 2.21	$\Delta G^{\#}$	$k(\mathrm{s}^{-1})$ Theo	Exp
BQO	-2.4	0.78	-	1.2×10^8	$(2.5\pm0.3)\times 10^8$
NAP	-0.03	0.74	0.2	4.4×10^6	$(1.5\pm0.5)\times10^6$
NQO	-2.1	0.73	-	6.7×10^8	$(3.8\pm1)\times10^8$
PHN	-0.1	0.71	0.2	1.3×10^7	$(1.2\pm0.2)\times10^7$
PYE	-0.5	0.66	0.01	4.0×10^9	$(1.5\pm0.5)\times10^9$

$\epsilon_0(T) = -1.50 + 2650/T$ over the range -78 to 30 °C,[108] is taken into account. As $\epsilon(T)$ increases with temperature, the solvent reorganization energy also increases. However, since ET to BQO proceeds via tunneling, the larger λ_s values have only a mild effect, slightly increasing the Franck–Condon weighted density of states without significantly altering the rate.

Overall, the trends in temperature dependence observed in the previous section are confirmed using the λ_s values computed via Marcus' non-equilibrium formalism, demonstrating that the same qualitative behavior is preserved with this computational approach. To gain deeper insight into the microscopic origin of solvent effects, the next chapter focuses on the calculation of λ_s using an explicit solvent model.

Chapter 3

Environmental Reorganization in Organic Materials

In the preceding chapter, the solvent reorganization energy (λ_s) was evaluated using continuous models, based on Marcus' non-equilibrium formalism. Noteworthy, such continuous models successfully reproduce the general temperature dependent trends observed in ET processes, even though they rely on a macroscopic description of the solvent, which inherently neglect its molecular nature. Consequently, local structural rearrangements of solvent molecules around the solute are not captured, despite their possible influence on λ_s. Indeed, the limit of dielectric continuum models have been extensively highlighted in theoretical and simulation studies.[67, 5, 13] Jen and Warshel showed that both strongly and weakly coupled vibronic modes must be considered to accurately describe the solvent bath, in agreement with MD simulations showing that the main contributions to the external reorganization energy (λ_s) arise from

rearrangements within the first and second solvation shells.

The accuracy of implicit models is further compromised in weakly polar environments. Experimental estimates of λ_s in nonpolar liquids have yielded values significantly larger than those predicted by continuum approaches,[57] and recent MD-based investigations indicate that implicit methods systematically underestimate λ_s in apolar organic systems.[172] These discrepancies arise from the neglect of specific solute–solvent interactions and dynamic polarization effects, highlighting the necessity of explicit or hybrid computational strategies for a realistic description of solvent reorganization in ET processes.

This chapter focuses on our efforts of implementing a reliable methodology for explicitly modeling the solvent reorganization energy. Being interested both in ET in solution and in the solid phase, both molecular solutions and organic crystals will be considered. The study of solvent reorganization in molecular solutions and the analysis of thermal disorder in organic crystals are closely related, as both phenomena originate from fluctuations in the surrounding environment that influence the electronic structure of the system. Two cases will be considered in detail: naphthalene in liquid THF and naphthalene and pentacene in the solid state. In the case of naphthalene dissolved in liquid THF, solvent reorganization governs the stabilization and redistribution of charge following ET, contributing to the overall reorganization energy of the redox process. In crystalline naphthalene and pentacene, analogous effects arise from thermal motions of the lattice, which induce dynamic fluctuations in site energies and intermolecular couplings. These thermal

perturbations act as the solid-state counterpart of solvent reorganization, modulating the degree of charge localization and affecting carrier mobility.

By examining both regimes within a consistent theoretical framework, it should be possible to provide a unified understanding of environmental reorganization. This perspective highlights how electronic energy levels and charge transport properties are shaped not only by intrinsic molecular structure but also by the dynamic response of the surrounding medium, be it liquid or solid.

3.1 Theoretical formulation

There are two possible ways for explicitly modeling solvation of a molecular species: semiclassical model based on molecular dynamics calculations on a very large number of molecules and quantum mechanical calculations besed on a limited number of solvent molecules, but employing more realistic potentials. The former approach mainly suffer of the use of empirical force fields, which, in many cases, have been derived for neutral molecules and are therefore unsuited to treating systems in which the molecular species can have several oxidation states and variable charges. The latter approach is mainly limited to the use of a few solvent molecules, whereas electrostatic effects, especially in the case in which molecular species carry a net charge, are known to be characterized by a long range behavior, which requires the use in simulations of a very large number of explicit solvent molecules. Even though long range behavior

is reasonably accounted for, effects due to size truncation can dramatically affect the reliability of such explicit solvent calculations. For instance, in protic solvents it can occurs that the number of hydrogen bonds formed among solvent molecules is not conserved, thus causing significative errors in the evaluation of solvation-dependent properties.

Herein, we will consider a novel approach, which, to the best of our knowledge, has been scarcely used before to the evaluation of solvent effects on redox species.[4, 3]

We will use solid state computational methodologies for simulating bulk solvents and include solute by resorting to the supercell method. That approach has been widely used for investigating defects in solids. In Figure 3.1 the stick and ball representation of the cubic supercell employed to simulate liquid THF is reported. The integration of the supercell approach with molecular dynamics calculations thus allows a reliable description of the bulk properties of the solvent, together with the possibility of performing an extensive sampling of nuclear configurations of the solute-solvent interactions, necessary to include entropic effects.

Within the grand-canonical formulation of solutes in solution, the formation energy of a solute X with charge q and coordinates R_q is given by:[156, 8, 165]

$$G_f^q[X, R_q] = G^q[X, R_q] - G[bulk] - \sum n_i \mu_i + q(\epsilon_v + \mu) + E_{corr}(q, R_q), \tag{3.1}$$

where $G^q[X, R_q]$ and $G[bulk]$ are the free energies of the defective and pristine systems, μ_i the chemical potential of the i-th added/subtracted species, ϵ_v the valence band maximum

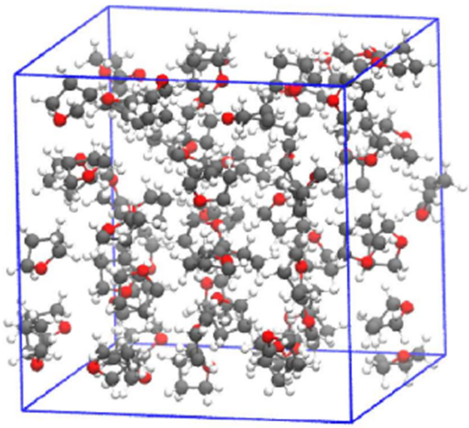

FIGURE 3.1: Stick and Ball representation of the cubit supercell of liquid THF (C atoms in gray, O in red, and H in white).

(VBM) of solvent, μ the chemical electron potential referred to ϵ_v , and $E_{corr}(q, R_q)$ is an electrostatic finite-size correction accounting for the spurious interactions due to the presence of a charged periodic supercell (See the Computational Details in Chapter 5). The redox potential associated with the following half-reaction:

$$X(Y) + e^- \rightarrow X^-(Y) \tag{3.2}$$

is defined as:[8, 11]

$$E^0(X/X^-,\ Y \text{ vs. vacuum}) = \Delta G_{red} - E_{corr}(-1, R_{-1}) \tag{3.3}$$

where:

$$\Delta G_{\text{red}} = G(-1, R_{-1}) - G(0, R_0) \tag{3.4}$$

and X and Y are the solute and the solvent respectively. In eq.

3.3, $\Delta G_{red} = G(-1, R_{-1}) - G(0, R_0)$ is the free energy difference between the anion and the neutral solute in their respective equilibrium structures R_q. This term is first referred to $\epsilon_V(T)$ and then aligned with respect to the vacuum level via the potential offset. $E_{corr}(-1, R_{-1})$ is a term included to correct the electrostatic finite-size error, typical of DFT calculations including a solute/defect with charge q and coordinates R_q in a periodic supercell (cf. Refs. [10] for details on the correction). ΔG_{red} is here calculated employing thermodynamic integration of vertical energy gaps:[46]

$$\Delta G_{red} = \int_{-1}^{0} \langle \Delta E \rangle_q dq, \tag{3.5}$$

where $\langle \Delta E \rangle_q$ is the vertical energy gap between neutral and negatively charged solute in the condensed phase. This is calculated on the structural configurations from the MD simulations at charge q:

$$\langle \Delta E \rangle_q = E(-1, R_q) - E(0, R_q) \tag{3.6}$$

Thermodynamic integration is a conceptual simple numerical technique which allows to evaluate free energy differences between two state of a system. The physical problem to be handled is the inclusion of entropic contribution, which cannot be numerically calculated. Indeed, while internal energy differences can be computed without conceptual difficulty, the case of free energy difference, defined in statistical thermodynamics as $F = k_B T \ln Z$, poses difficulties because one should analyze a very large number of configurations to numerically evaluate the partition funtion Z of the system. The trick is thus that of

evaluating infinitesimal energy difference changes and then integrate such .contributions over a convenient path connecting the two states.

To account for deviations from the linear Marcus regime typically encountered for redox potentials in solution,[8, 32] a three-point approximation to the thermodynamic integral is used. In particular, it is considered the neutral solute ($q = 0$), its anion ($q = -1$) as well as a fictitious system in which a fractional charge of 0.5 e^- is imposed on solute X. All the vertical energy gaps are again averaged over calculations on top of 100 MD configurations equally spaced in time (one each 10 ps).

The vertical electron affinity of X, $VEA(X,Y)$, and the vertical detachment energy of X^-, $VDE(XP^-,Y)$, are defined, respectively, as follows:

$$VEA(X,Y) = \langle \Delta E \rangle_0 + E_{corr}(-1, R_0), \tag{3.7}$$

$$VDE(X^-,Y) = \langle \Delta E \rangle_{-1} - E_{corr}(0, R_{-1}) + E_{corr}(-1, R_{-1}). \tag{3.8}$$

In eqs 3.7 and 3.8, $E_{corr}(-1, R_0)$ is an electrostatic finite-size term necessary to correct the total energy of the negatively charged periodic supercell upon vertical injection of an electron into the neutral system (R_0), while $E_{corr}(0, R_{-1})$ is the correction to the energy of the neutral system formed when vertically detaching an e^- from the anion (R_{-1}) in the periodic cell (see Ref. [42] and Section S1 of Ref.[10] for details).

At this point, the two total reorganization energies, one

associated with the reduction of X, $\lambda(red)$, and another to the oxidation of X^-, $\lambda(ox)$, are defined as :

$$\lambda(red) = E^0(X/X^-,\ Y) - VEA(X,\ Y) \tag{3.9}$$

$$\lambda(ox) = VDE(X^-,\ Y) - E^0(X/X^-,\ Y). \tag{3.10}$$

Since $\lambda = \lambda_{int} + \lambda_{ext}$, the respective solvent reorganization energies (λ_{ext}s) can be estimated , noted λ_{int}s.

3.2 THF solution with Naphthalene

THF is selected as a representative weakly polar solvent, exhibiting properties that differ from both highly polar and apolar media,[16, 24, 25] making it a suitable system for benchmarking computational methodologies for λ_s. Furthermore, THF has been extensively employed in experimental studies of ET reactions. Naphthalene is chosen as the solute to investigate solvent reorganization associated with its reduction to NAP^- and the reverse oxidation process. The NAP/NAP^- redox couple has been thoroughly characterized in both experimental and theoretical ET studies, including recent liquid jet photoemission spectroscopy measurements[113] that provide a reliable reference for validation.

3.2.1 Structural properties of THF

The structural and electronic properties of THF are investigated through classical MD simulations employing a quantum-mechanics-derived force field.[51, 118, 28] Detailed simulation conditions and parameters, together with the functional and basis set construct for the DFT calculations are provided in the Computational Details (Chapter 5).

To validate the computational adapted protocol, the oxygen-oxygen radial distribution function, $g_{OO}(r)$, obtained from the MD simulations is compared with the experimental data in Figure 3.2(a) in which the pronounced peak at 4.6 Å is accurately reproduced by the model.

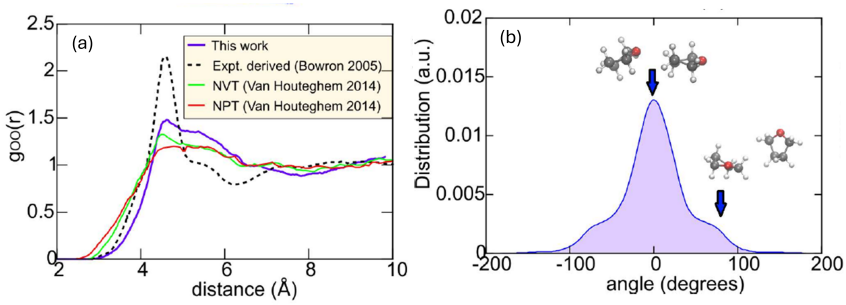

FIGURE 3.2: (a) Oxygen-Oxygen radial distribution function for liquid THF from the present MD simulation, compared with previous experimental and computational studies. (b) Distribution of angles formed by the molecular planes of firstneighbours THF pairs, using oxygen atoms as reference points.

THF exhibits two conformers energetically separated by an exiguous difference. The twisted conformer with C_s symmetry

is found to be more stable of the envelope structure displaying C_2 symmetry by only a few meV.[131, 50, 119]

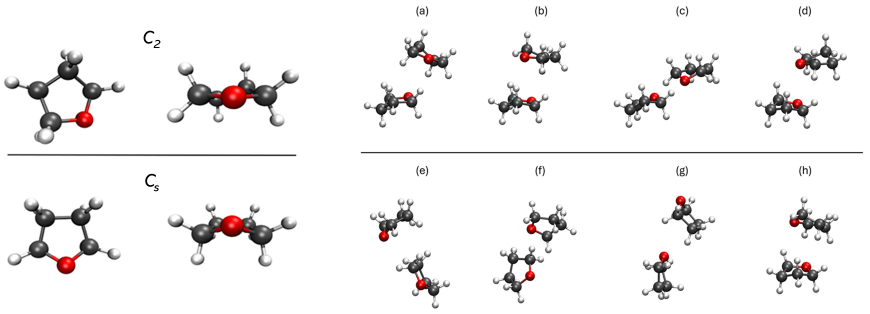

FIGURE 3.3: Stick&ball representation of C_2 and C_S THF conformers and THF dimers from Ref.[100]

To further evaluate the computational protocol, described in details in the Computational Details (Chapter 5), the energy difference between different structural configuration of THF dimers (Figure 3.3) are computed and compared with those reported in Ref. [100]. As reported in Table 3.1 van der Waals (vdW) are fundamental to distinguish the different dimer structures. When the pure functional (KC) is employed, all configurations are nearly iso-energetic over 0.021 eV. Inclusion of vdW interactions increases the energy spread to approximately 0.1 eV, with the most stable configurations corresponding to molecules lying in the same plane or stacked on top of each other with O atoms an apposite positions, whereas stragged or nearly perpendicular arrangements are slightly less favorable.

The relative orientation of THF molecules is further characterized by the calculated angular distribution between the

Table 3.1: Total energies of the different THF dimers, referred to that of the a configuration. All values are given in eV

Dimer	KC	KC+ vdW	Ref. [100]
a	0.0	0.0	0.0
b	0.000	0.079	0.003
c	0.002	0.080	0.004
d	0.004	0.082	0.006
e	0.005	0.084	0.014
f	0.006	0.087	0.056
g	0.013	0.093	0.071
h	0.021	0.100	0.082

molecular planes of interacting pairs, using oxygen atoms as reference points. The distribution, illustrated in Figure 3.2(b), exhibit a peak at 0°, indicating a preference for parallel molecular alignment with additional shoulders at approximately ± 74° correspond to near-perpendicular arrangements, consistent with DFT calculations shown in Table 3.1. These results collectively confirm that the computational protocol reliably reproduces both the structural and intermolecular interaction features of THF.

3.2.2 Electronic structure and energy level alignment

The electronic structure of THF and the alignment of its energy levels relative to vacuum were investigated by examining the THF/vacuum interface. The analysis of the potential profile

across the interface (ΔV_{int}) reveals a clear potential offset of ΔV_{int} = 3.73 eV between the bulk-like region of the liquid and the vacuum, providing a direct reference for the absolute energy levels of the system. This alignment allows the determination of valence and conduction band edges at room temperature, ensuring that the calculated energy levels reflect the intrinsic electronic structure of the liquid.

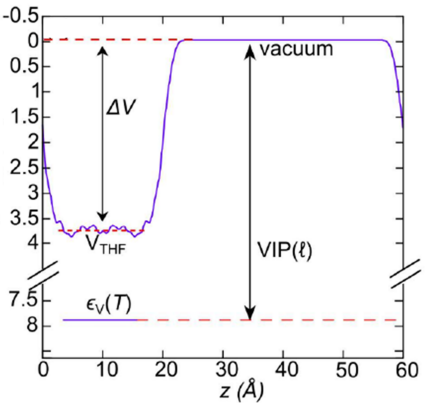

FIGURE 3.4: Schematic representation of the alignment at the liquid THF/vacuum interface for the valence band edge.

The averaged electronic density of states (e-DOS) illustrated in Figure 3.5 shows that the vertical ionization potential (VIP) is 7.94 eV below the vacuum level, consistent with experimental measurements ($\sim$ 7.8 eV).[113] The vertical electron affinity (VEA) is found at 1.43 eV above vacuum, indicating that THF does not readily accommodate an extra electron, as expected for saturated organic molecules.[152] These values provide insight into the stability of electronic states in the liquid and the energetic cost of electron addition or removal.

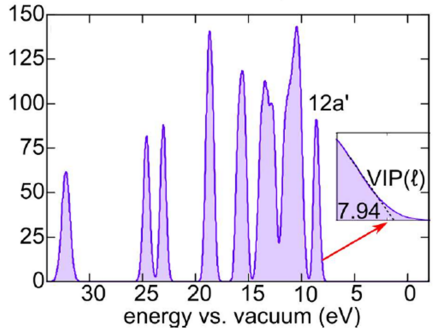

FIGURE 3.5: Averaged electronic density of states calculated for liquid THF. Energies are referred to the vacuum level. The peak associated with the 12a′ molecular orbital of THF is highlighted in the inset in which it is shown the linear extrapolation employed to evaluate the vertical ionization potential of liquid THF.

Comparison with gas-phase measurements in Table 3.2 shows that the vertical ionization potential in the condensed phase is slightly reduced relative to the isolated molecule (gas-phase VIP = 9.70 eV), reflecting the stabilizing effect of the surrounding liquid environment. The overall shape of the e-DOS and the position of the valence band edge also reproduce the experimental spectral features, confirming that the structural organization of THF is closely linked to its electronic properties. These findings demonstrate that the energy landscape of liquid THF can be reliably described and provide a physically meaningful reference for the study of solute–solvent interactions, including the alignment of energy levels for molecular species dissolved in THF.

Table 3.2: Calculated and Experimental Electronic Levels of THF for the Gas and Liquid Phases. All energies are in eV.

	VIP (gas)	VIP (liquid)	$12a'$ peak (liquid)	VEA (liquid)
Theory	9.70	7.94	8.63	-1.20
Expt.	9.71 ± 0.03^a	7.80^b	8.5 ± 0.1^b	-

[a] Photoelectron spectra of THF from Ref. [37] [b] Photoemission spectroscopy measurements from Ref. [113]

3.2.3 Redox potentials and solvent reorganization energy

The solution of THF containing a single NAP molecule was modeled by replacing one THF molecule in the bulk simulation cell with a NAP molecule. MD simulations of this system indicate that the introduction of NAP generates localized states within the THF band gap.

Analysis of the HOMO and LUMO, together with the averaged e-DOS (Figure 3.6), shows that the HOMO of NAP corresponds to a VIP of 7.07 eV relative to vacuum, in close agreement with experimental data ($\pm$ 0.11 eV).[113] The analysis highlights the effect of solvation on energy level alignment: the interaction with the THF matrix stabilizes the frontier orbitals of NAP, providing a reference for subsequent studies of charge transfer and redox processes. Gas-phase calculations confirm that the VIP of NAP increases in isolation (8.05 eV), indicating that the condensed-phase environment lowers the energy required for ionization, consistent with solvent stabilization effects.[34]

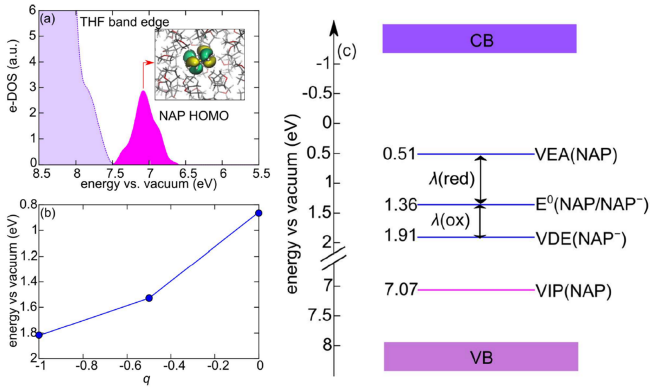

FIGURE 3.6: (a) Electronic density of states (e-DOS) of the occupied energy levels for the liquid THF/NAP atomistic model. The peak relative to the highest occupied molecular orbital of NAP is given in magenta. The isodensity representation (isovalue 0.01) of the HOMO for a structural configuration is shown in the inset. (b) $<\Delta E>_q$ (cf. main text for definition) as a function of the charge q. Values are referred with respect to the vacuum level. (c) Schematic representation of the energy levels associated with the NAP/NAP$^-$ redox couple in THF liquid.

These observations enable the estimation of vertical and adiabatic redox potentials associated with the NAP/NAP$^-$ couple. By considering the relative alignment of the solute's HOMO and LUMO with respect to the THF energy levels, the electronic response of the system to electron addition and removal can be quantified. Such analysis further allows the calculation of the external reorganization energy associated with electron transfer, providing insight into the energetics of redox processes in solution.

Vertical redox potentials of the NAP/NAP$^-$ couple are computed from eqs 3.9-3.10, within the grand-canonical formulation described in Section 3.1. Adiabatic redox potential is computed employing thermodynamic integration of vertical energy gaps averaged over calculations on top of 100 MD configurations equally spaced in time (one each 10 ps) considering the neutral NAP ($q = 0$), its anion ($q = -1$), and a fictitious system in which NAP has a fractional charge of 0.5 e^- (eqs 3.5-3.6). In Figure 3.6 (b) it is clarly shown the deviation from linearity aspected from Marcus approximation of the vertical energy gaps with different qs imposed. This leads to a difference in the calculated adiabatic redox potential. In fact, thermodynamic integration gives $E^0(NAP/NAP^-,\ THF$ vs. vacuum) = 1.36 eV, with a difference of 0.15 eV respect to the Marcus Approximation.

In Table 3.3 are collected, for comparison, the available experimental data in solution together with the calculated and measured gas-phase data. The Table 3.3 shows a difference of approximately 0.8 eV in the redox potential from the experimental estimate. It should be considered that in Ref. [113], the solvated NAP$^-$ species was generated via alkali-metal addition to the solution, implying that the photoemission spectra reflect ion-pair states rather than isolated anions. Comparable electrochemical configurations yield analogous results,[35] indicating that the observed energy shift arises from ion-pair stabilization through Coulombic interactions, which lowers both vertical and adiabatic levels.

Calculation with the PCM models yields E^0 = 1.45 eV, within

Table 3.3: Calculated and measured electronic energy levels and reorganization energies for the NAP/NAP$^-$ redox couple in the gas phase and in THF solution.

Gas phase	Theory	Expt.
VIP(NAP)	8.05	8.15[a]
VEA(NAP)	−0.50	//
VDE(NAP$^-$)	−0.20	−0.18[b]
E^0(NAP/NAP−)	−0.35	−0.19[c]
λ_{int}	0.14	//
THF Solution	**Theory**	**Expt.**
VIP(NAP)	7.07	7.18[d]
VEA(NAP)	0.51	//
VDE(NAP$^-$)	1.91	2.73[e]
E^0(NAP/NAP−)	1.36	2.05[f]-2.21[e]
λ(red)	0.85	//
λ(ox)	0.55	0.52-0.68[g]

[a] Photoemission spectrum of gas-phase NAP from Ref. [34]; [b] Value extrapolated from photoemission measurements performed on clusters in Refs. [139, 98, 150]; [c] Inferred from electron transmission spectra of Ref. [27]; [d] Photoemission spectrum of NAP in THF solution from Ref. [113]; [e] Photoemission spectra of NAP$^-$ in THF solution from Ref. [113], value referred to the ion pair with a metal cation; [f] Voltammetry measurements from Ref. [35] for the NAP$^-$/metal cation pair; [g] Difference between VDE of Ref. [113] and available E^0 estimates, cf. Equation 3.10.

0.1 eV of the MD value confirming that the experimental deviation primarily results from ion-pair formation. The consideration of the free anion is therefore appropriate, as in ET

experiments organic radical anions such as NAP^- are typically generated by pulse radiolysis, a process that effectively suppresses ion-pairing.[33]

Having established the behavior of the redox levels in solution, attention is next directed to the gas-phase electron affinities, which generally present a great challenge for theoretical methods. The reported value of –0.19 eV from electron transmission spectroscopy has been described as adiabatic, despite the inherently vertical nature of the technique.[27] In contrast, vertical detachment energies between –0.18 and –0.20 eV have been obtained by extrapolating photoelectron spectra from molecular clusters.[139, 98, 150] Together, these data imply a nearly negligible internal reorganization energy, λ_{int}. The present calculation yield $E^0(NAP/NAP^-, g) = -0.35$ eV and $VDE(NAP^-, g) = -0.20$ eV, both in good agreement with the experimental range. The resulting λ_{int} = 0.15 ev is consistent wit previous many-body perturbation and coupled-cluster results.[53, 141, 160, 73] This agreement confirms the reliability of the computational approach and provides a solid foundation for the subsequent evaluation of the solvent reorganization energy, λ_{ext}.

From eq. 3.10, the total reorganization energy for oxidation was determined as $\lambda(ox)$ = 0.55 eV. Considering that $\lambda = \lambda_{int} + \lambda_{ext}$, the external contribution for the oxidation is therefore $\lambda_{ext}(ox)$ = 0.40 eV. Similarly, the total reorganization energy for reduction (eq. 3.9) is $\lambda(red)$ = 0.85 eV, giving $\lambda_{ext}(red)$ = 0.70 ev. These results indicate that the solvent reorganization constitutes the dominant contribution to the overall energy

relaxation process.

To further elucidate the microscopic origin of the solvent contribution to the reorganization energy, the solute–solvent interactions were examined from the MD simulations of solvated NAP and NAP^-. The radial distribution functions (RDFs) between the solute center of mass and THF oxygen atoms show a peak at 5.67 Å for the neutral molecule, with a broad shoulder extending to 8.50 Å indicative of weak, disordered solvation. Upon reduction, the peak shifts to 6.37 Å while the coordination shell size remains unchanged, reflecting a solvent reorganization in response to the added negative charge. This corresponds to a rotation of THF molecules in the first solvation shell, with oxygen atoms oriented away from the enhanced electron density of anionic NAP.

Extending the analysis to the RDFs between the centers of mass of solute and solvent molecules (Figure 3.7), a shoulder appears in the first solvation shell of NAP^- approximately 1.5 Å closer than the main peak, corresponding on average to 1.25 THF molecules. This feature exceeds the shift expected from simple electrostatic repulsion and reflects a weak inductive effect, where loosely bound THF molecules are polarized by the anion's electric field and drawn slightly closer. To quantify the contribution of these nearby THF molecules to the external reorganization energy, a representative NAP–THF dimer is extracted from the MD configurations. Constrained structural relaxations are performed by scanning the CM–CM distance from 3.5 to 6 Å yielding a distance-dependent energy profile (Figure 3.8).

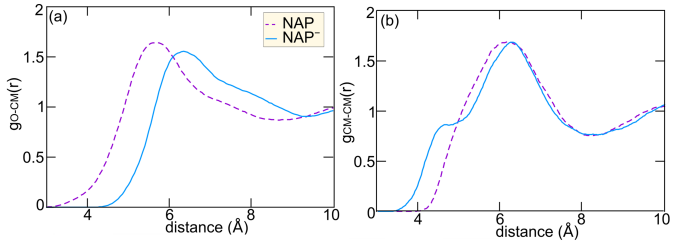

FIGURE 3.7: Radial distribution function between (a) the center of mass (CM) of the solute and the O atoms of THF for NAP and (b) the center of mass of the solute and solvent molecules for NAP and NAP^{-} in liquid THF.

For the anionic dimer, the profile exhibits a minimum at 4.25 Å close to the RDF shoulder, with an energy 0.27 eV lower than the reference configuration at 6 Å. For the neutral dimer, the minimum is shallower, at 4.75 Å, with an energy difference of only 0.13 eV, dominated by vdW interactions. From this analysis, single-molecule polarization contributes roughly 0.27 eV to $\lambda_{ext}(ox)$ and 0.13 eV to $\lambda_{ext}(red)$, representing a substantial fraction of the total external reorganization energy.

The dipolar contribution is further characterized by the orientation of THF dipoles relative to the NAP molecular plane, quantified by the angle θ (Figure 3.9), where positive values indicate dipoles pointing away from the plane. For neutral NAP, the θ distribution is symmetric around 0°, whereas for NAP^{-} it becomes asymmetric and peaks at positive angles, reflecting preferential dipole orientation away from the charged solute. The asymmetry increases when only the nearest solvent molecules are considered, highlighting that the motion and

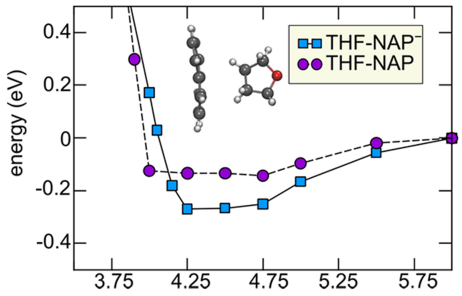

FIGURE 3.8: Energy profile for the THF-NAP and THF-NAP^{-} dimers as a function of the CM-CM distance. For each dimer, energies are referred to those calculated at a distance of 6 Å.

polarization of a few first-shell THF molecules dominate the solvent response and underpin the computed λ_{ext} value.[6, 14, 169]

In conclusion, the combined MD and hybrid DFT protocol provides a robust and efficient framework for quantifying external reorganization energies, capturing both local polarization and dipole–charge contributions. The methodology offers a detailed microscopic understanding of solvent response that goes beyond continuum models. This approach lays the basis for systematic studies of solvation effects and for predicting electron-transfer behavior in more complex molecular system.

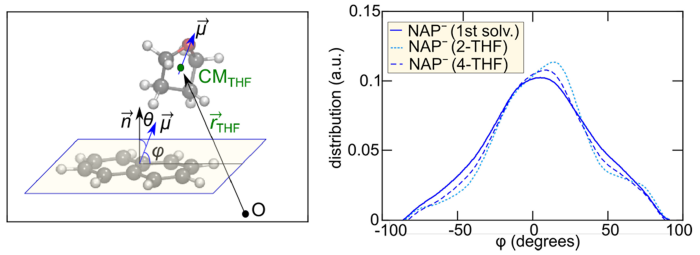

FIGURE 3.9: Left : graphical representation of the ϕ angle between the solute molecular plane and the THF dipole moment. Right : distribution of the angle ϕ between the solute molecular plane and the THF electric dipole moment for neutral NAP and its anion, as calculated for the first solvation shells, evaluated from the respective MD simulations.

3.3 Reorganization and disorder: linking solution and solid-state charge dynamics

Naphthalene and pentacene are selected among stable condensed acene molecules because they are those with the largest (naphthalene) and the smallest (pentacene) reorganization energies,[9] and, therefore, represent the two limiting cases of charge localization and charge mobility.

To preliminary assess charge localization upon hole injection, the electronic structures of the neutral and positively charges systems are compared by analyzing the corresponding electronic DOS, obtained as an average over 50 MD structural configurations sampled at equal time intervals.

Naphthalene, (Figure 3.10(a)) exhibits the emergence of a secondary, small peak in the DOS of the charged system, centered approximately 0.6 eV above the VBM. This feature indicates the presence of a localized state within the band gap, cooresponding to the formation of a hole polaron.

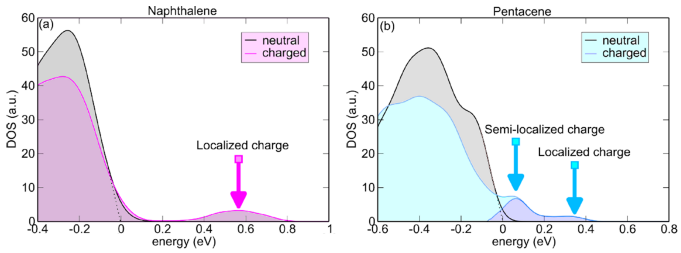

FIGURE 3.10: Electronic DOS near the valence band edge for neutral and positively charged (a) naphthalene and (b) pentacene supercells, as achieved from the average of 50 MD structural configurations.In each panel, energies are referred to that of the VBM. In panel (b) a darker shade is used to highlight the DOS of the lowest unoccupied molecular orbital.

In the case of positively charged pentacene (Figure 3.10(b)), the DOS reveals a broad shoulder in the valence band extending up to roughly 0.4 eV above the VBM. This structure, consisting of a narrow peak near the VBM and a broader component at higher energies, is indicative of the coexistence of semi-localized and more strongly localized electronic states.

It should be noted that no charge localization was reported for the ordered material in Ref. [9], suggesting that structural disorder plays a critical role in promoting polaron formation

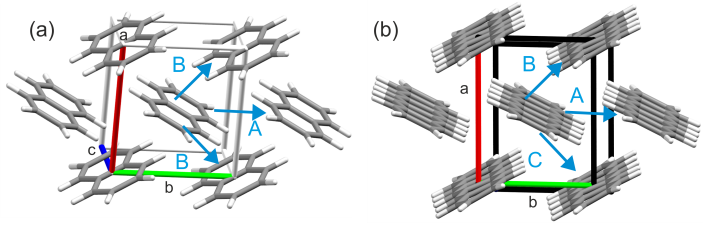

FIGURE 3.11: Structural representation of herringbone structure of (a) naphthalene and (b) pentacene. Unique hole hopping paths (differing by symmetry) are reported as blue arrows and identified by letter A, B and C.

and in modulating the competition between localized and delocalized charge carriers.

Based on the analysis of charge localization and the associated electronic density of states, the calculation of the hole polaron chemical potential, μ in naphthalene and pentacene is performed at room temperature using the theoretical framework described in Section 3.1. For naphthalene, thermal disorder shifts both the vertical and adiabatic charge transition levels upward by ~ 0.18 eV, reflecting the broadening-induced shift of the VBM. In contrast, pentacene shows minimal charge localization in the ordered crystal, but thermal and structural disorder induces partial hole confinement, yielding average adiabatic and vertical levels of 0.09 eV and 0.19 eV, respectively.

The total reorganization energy associated with charge localization, $\lambda = \mu_{red} - \mu_{ad}$ is decomposed into molecular (λ_{int}) and environmental (λ_{ext}) contributions. For both materials, molecular relaxation dominates (λ_{int} = 0.11 eV for naphthalene, 0.06 eV for pentacene), while the surrounding environment also

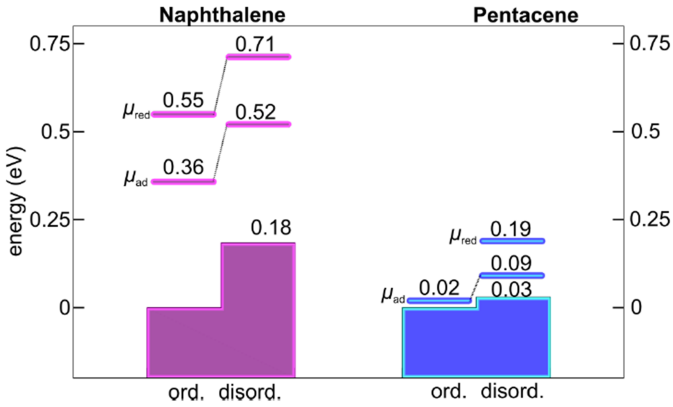

FIGURE 3.12: Schematic representation of the adiabatic hole polaron level and of the vertical reduction energy of the acene cation in crystalline naphthalene and pentacene at room temperature (300 K), as calculated for the ordered crystallographic structure and including disorder from the average value achieved from sampling of MD structural configurations. For each organic semiconductor, energies are referred to that of the VBM of the neutral ordered system.

provides a significant stabilizing effect (λ_{ext}=0.08 eV and 0.04 eV, respectively). These results indicate that, despite the apolar nature of acene crystals, both molecular and environmental reorganization significantly influence μ, enabling a quantitative evaluation of charge localization and polaron stability.

The analysis of acene crystals in the presence of thermal disorder is completed by examining the structural factors contributing to the λ_{ext}. Using MD simulations, the relative positions of a reference molecule (neutral or charged) with respect

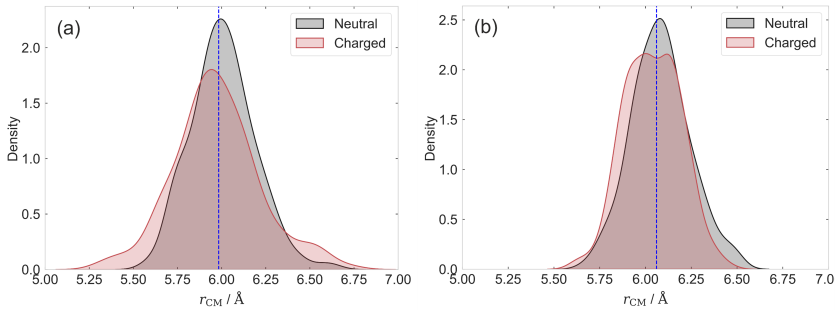

FIGURE 3.13: Distributions of r_{CM} (Å) between the neutral and charged reference molecule and its stacked neighbours for: naphthalene (a) and pentacene (b) crystals at 300 K. The curves are normalized so that the integral over all possible values is 1. The blue vertical dashed line indicates the value in the perfect crystal.

to its six nearest neighbors are characterized in terms of center-of-mass distances (r_{CM}) and Tait-Bryan angles (pitch, roll, yaw) which are a standard notation to describe the orientation of a rigid body with respect to another plane.

The r_{CM} distributions (Figure 3.13) reveal notable differences upon charging: both naphthalene and pentacene exhibit shifts toward shorter distances, reflecting stronger local interactions for stacked neighbors (7–11). Naphthalene displays a $\sim$ 0.1 Å shift and broader distributions, whereas charged pentacene shows two peaks, one matching the neutral structure and another at $\sim$ 0.14 Å shorter. The combination of Figures 3.11, 3.13, and 3.14 provides a clear visualization of the structural origin of the environmental contribution to polaron stabilization and suggests distinct effects of thermal disorder on charge mobility

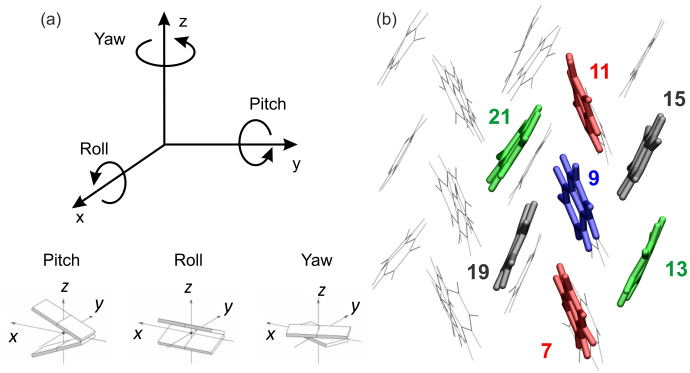

FIGURE 3.14: Molecular Orientation and Nearest-Neighbour Symmetry in Naphthalene and Pentacene. Left: Schematic representation of Tait-Bryan Angles in a cartesian frame. Right: Representation of first-neighbours in naphthalene; each colour identifies symmetry-equivalent neighbours. For pentacene, the numbering is the same.

in naphthalene and pentacene.

The results highlight that thermal disorder shifts the polaronic hole energy levels toward higher energies, thereby stabilizing the localized charge. This effect is particularly significant in pentacene, where room-temperature disorder promotes polaron formation in contrast to the delocalized character predicted for the ordered crystal. The methodology presented in Section 3.1, previously validated for reproducing solvent reorganization effects in liquid THF, successfully captures also the impact of thermal disorder on acene crystals providing a reliable and transferable description of how dynamic disorder and environmental reorganization govern charge localization and transport in organic semiconductors.

Chapter 4

Characterization of Excited-State Relaxation via IC and ISC

Non-radiative transitions, where a molecule in an electronically excited state returns to a lower energy state without the emission of a photon, are fundamental processes in molecular photophysics. Two of the most prominent non-radiative pathways are internal conversion (IC) and intersystem crossing (ISC).

IC involves a radiationless transition between electronic states of the same spin multiplicity, typically facilitated by vibronic coupling, which allows excess electronic energy to be dissipated as vibrational energy within the molecule.

ISC, on the other hand, corresponds to a spin-forbidden transition between states of different multiplicity, usually from a singlet to a triplet state, and is mediated by spin-orbit coupling. Understanding these processes is crucial, as they govern

the excited-state lifetimes, photostability, and photochemical behavior of molecular systems.

Theoretical modeling of IC and ISC provides insights into the mechanisms underlying energy relaxation upon photon absorption and enables the prediction of non-radiative decay rates, which are essential for designing molecules with tailored photophysical properties.

This chapter presents the results obtained with the theoretical model introduced in Chapter 1, focusing on IC and ISC in molecular systems. The analysis begins with small organic molecules, such as azulene and xanthone, which serve as reference systems for exploring the relationship between electronic structure and relaxation dynamics. These molecules provide a reliable framework for assessing the accuracy and predictive capability of the model.

4.1 The photophysics of azulene

All the results, figures and tables presented here are taken from a personal research (Ref. [85]).

Azulene has been extensively studied due to its anomalous photophysical behavior,[162, 38, 127, 61, 159, 52] representing a well-known violation of Kasha's rule. In both the gas phase and in solution, the first excited singlet state (S_1) relaxes rapidly to the ground state (S_0), largely suppressing radiative emission from S_1.[61] While weak S_1 fluorescence has been observed,[132] the strongest emission originates from the second excited singlet state (S_2), since the $S_2 \rightarrow S_1$ IC is slower than radiative

decay.[159, 52, 163, 144] The short S_1 lifetime was initially inferred from the broader vibrational lines of its absorption band compared to S_2,[60, 59] and later confirmed by time-resolved spectroscopy, which showed that S_1 decays directly to S_0 rather than via a triplet state.[61]

Given that IC rates are experimentally known, azulene provides an ideal benchmark for testing the computational approaches described above. The large energy gaps between S_1 and S_0, and between S_2 and S_1, further ensure that numerous final vibrational states contribute to the dynamics, making it particularly suitable for methodological validation. First of all, equilibrium geometry calculations at both TDDFT and MCSCF levels confirm that C_{2v} symmetry is preserved in both excited states, consistent with previous studies.[40] The existence of C_{2v} symmetry restricts vibrational displacements to totally symmetric modes, while non-zero non-adiabatic couplings (NACs) occur only along B_2 modes.

From the calculated optimum geometries of the three electronic states of interest, reported in Table 4.1 , the equilibrium position dispacements (i.e. the **K** vector of eq. 1.61) and the rotation matrix **J** for both the transition S2–>S1 and S1–>S0 have been computed. The results are reported in Table 4.2, limited to the **K** vector, which usually provides the most important contributions to transition rates.

The components of the **K** vector (eq. 1.61) and the NACs projected onto the normal coordinates of the initial state are reported in Table 4.1 for the $S_1 \rightarrow S_0$ and $S_2 \rightarrow S_1$ transitions.

The calculated $F(\Delta E, T)$ functions for the two transitions are

Table 4.1: Wavenumbers (ω, cm^{-1}) of the initial electronic state, equilibrium position displacements (**K**, absolute values, Å x $amu^{1/2}$) and non-adiabatic coupling projected over the normal modes (NAC, $bohr^{-1} \times amu^{1/2}$) for the $S_1 \rightarrow S_0$ and $S_2 \rightarrow S_1$ transitions of azulene. Only normal modes belonging to A_1 and B_2 representation are reported.

$S_1 \rightarrow S_0$			$S_2 \rightarrow S_1$		
ω_1	ω_0	**K**/NAC	ω_2	ω_1	**K**/ NAC
		A_1			
392.11	413.35	-0.13	391.84	392.11	0.06
671.74	680.81	0.13	676.62	671.74	-0.04
878.98	834.26	0.27	848.91	878.98	-0.18
922.35	920.30	-0.08	912.69	922.35	0.01
939.45	963.24	0.0	941.64	939.45	-0.02
1093.89	1083.34	0.02	1043.21	1093.89	-0.06
1225.27	1245.40	-0.04	1196.73	1225.27	0.08
1255.34	1302.11	-0.12	1236.45	1255.34	-0.01
1425.52	1421.93	-0.19	1368.00	1425.52	0.0
1489.99	1490.31	0.07	1398.90	1489.99	0.13
1592.78	1582.86	0.0	1483.33	1592.78	0.09
1604.29	1631.25	-0.11	1546.62	1604.29	-0.04
3132.31	3130.00	0.0	3140.36	3132.31	0.0
3164.84	3140.38	0.0	3152.63	3164.84	0.0
3177.63	3168.22	0.0	3175.31	3177.63	0.0
3205.87	3197.30	0.0	3211.27	3205.87	0.0
3240.79	3224.24	0.0	3235.36	3240.79	0.0
		B_2			
336.13	340.09	0.05	334.58	336.13	-0.043
505.81	499.76	0.18	493.58	505.81	0.12
763.59	747.19	-0.46	746.78	763.59	-0.30
1044.94	1023.75	0.42	1044.67	1044.94	0.08
1084.89	1066.78	-0.08	1075.48	1084.89	-0.42
1169.86	1188.82	0.24	1172.29	1169.86	0.14
1238.80	1243.15	0.001	1247.87	1238.80	-0.22
1276.32	1325.64	-0.08	1284.35	1276.32	-0.29
1359.17	1339.33	-0.27	1380.77	1359.17	0.37
1400.60	1432.13	0.002	1427.83	1400.60	0.40
1466.36	1493.54	-0.01	1465.19	1466.36	-0.12
1537.57	1531.16	-0.30	1474.07	1537.57	-0.18
1689.74	1644.03	-0.12	1593.62	1689.74	-0.35
3135.85	3131.85	-0.004	3148.74	3135.85	-0.03
3166.15	3159.48	0.001	3167.57	3166.15	0.03
3209.82	3215.71	-0.02	3226.76	3209.82	0.02

presented in Figure 4.1 and display notable differences. The $S_1 \rightarrow S_0$ transition exhibits a very broad $F(\Delta E, T)$, extending over more than 15.000 cm^{-1}, whereas $F(\Delta E, T)$ for $S_2 \rightarrow S_1$ is more structured and decays more rapidly. The computed internal conversion rates, summarized in Table 4.2 along with the corresponding energy differences used in the calculations, show good agreement with experimental data and with results obtained from numerical solutions of the time-dependent Schrödinger equation.[85]

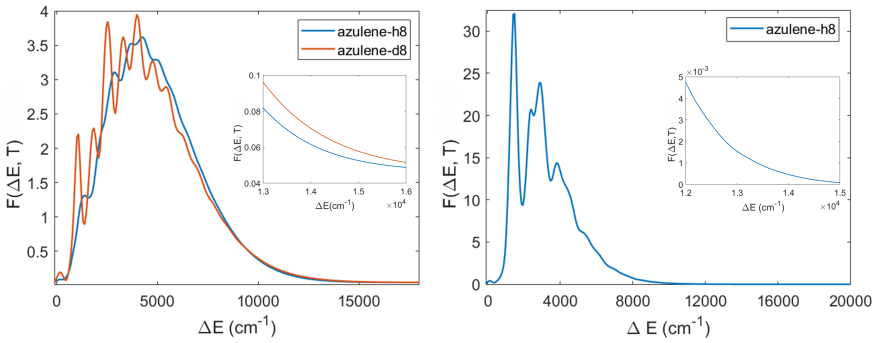

FIGURE 4.1: $F(\Delta E, T)$ at T = 298 K of the $S_1 \rightarrow S_0$ (left) and $S_2 \rightarrow S_1$ (right) internal conversions as a function of the energy difference between the initial and final states. The orange line refers to perdeuterated azulene (azulene-d8). The insets show a magnification of the energy regions where internal conversions occur.

The density of states for the $S_1 \rightarrow S_0$ transition of azulene-d_8 is also reported in Figure 4.1. Consistent with experimental observations, perdeuteration does not significantly affect the internal conversion rate. Likewise, the internal conversion rates are largely temperature-independent, as illustrated in Figure

4.2, which is consistent with the absence of displaced vibrational modes in azulene (see Table 4.1). The $F(\Delta E, T)$ functions

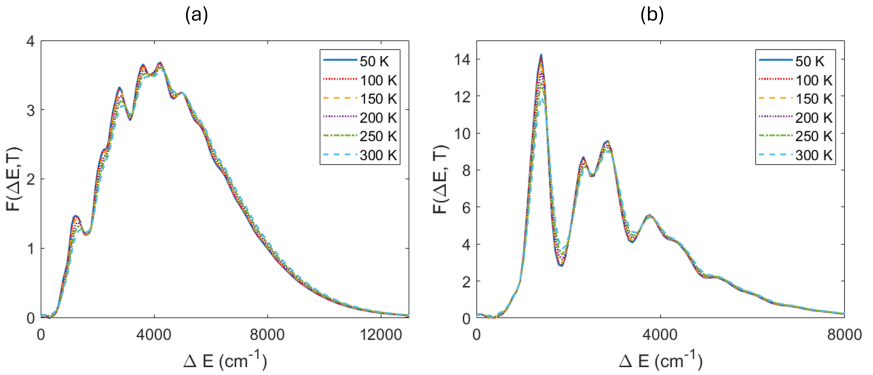

FIGURE 4.2: $F(\Delta E, T)$ at T = 298 K of the $S_1 \rightarrow S_0$ (left) and $S_2 \rightarrow S_1$ (right) internal conversions computed at different temperatures

calculated while neglecting the Duschinsky effect (i.e., setting $\mathbf{J} = \mathbf{I}$, where $\mathbf{I}$ is the identity matrix) are shown in Figure 4.3. The rotation of normal modes upon transition has minimal influence on transition times; it mainly smooths the vibrational progressions at lower ΔE for the $S_1 \rightarrow S_0$ transition and slightly shifts peaks at higher energies for the $S_2 \rightarrow S_1$ transition. These results are consistent with quantum dynamics calculations,[85] where the inclusion of A_2 and B_1 modes, which contribute only via the Duschinsky effect, did not affect the time-dependent populations of the initial and final states.

The pronounced difference in the widths of the $F(\Delta E, T)$ functions can be attributed primarily to the differing components of the $\mathbf{K}$ vectors rather than the calculated NACs. While

the NACs for the two transitions are relatively similar, the equilibrium displacement vectors **K** differ substantially. For the $S_2 \rightarrow S_1$ transition, only two totally symmetric modes, at 868 and 1398 cm^{-1}, exhibit significant displacements. In contrast, the $S_1 \rightarrow S_0$ transition involves at least six modes with large displacements, spanning a broad wavenumber range from 400 to 1600 cm^{-1}. These displaced modes broaden the density of states sufficiently to enable the $S_1 \rightarrow S_0$ transition to occur on short timescales.

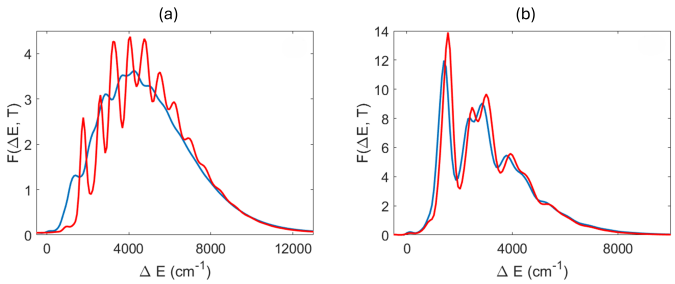

FIGURE 4.3: $F(\Delta E, T)$ at T = 298 K of the $S_1 \rightarrow S_0$ (left) and $S_2 \rightarrow S_1$ (right) internal conversions calculated with (blue curves) and without (red curves) including Duschinsky's effects.

The predicted IC rates are extremely different each other. While the $S_1 \rightarrow S_0$ transition is predicted to be fast, on the timescale of a few picoseconds, the other one is much slower of the order of nanoseconds. As shown in Table 4.2, where the predicted rate constants have been reported together with the available experimental data, the theoretical rate constants are in excellent agreement with the experimental ones, for both transitions.

Table 4.2: Energy difference (ΔE, eV) from Ref. [159], calculated IC rate (s^{-1}) in the gas phase, and experimental rates in different environments: gas phase, Ref. [61]; solid state, Ref. [159]; and solution, Ref. [52].

		Rate			
Transition	ΔE	Gas phase	Solid state	Solution	Theory
$S_1 \rightarrow S_0$	1.77	2.5×10^{11}	1.2×10^{11}	5×10^{11}	7.1×10^{10}
$S_2 \rightarrow S_1$	1.73	-	7×10^{8}	6×10^{8}	6.6×10^{8}

Since the theoretical procedure outlined in Chapter 1 is original, as well as the implementation of computer codes, the excellent agreement with the experimental results alone is not a sufficient test for assessing the correctness of the theoretical procedure of Chapter 1 and of the relative computer codes. A second check has been therefore carried out by performing quantum dynamics calculations by numerically solving the time dependent Schrödinger equation, using of course the same input data that have been employed in the FGR calculations, i.e. the data reported in Table 4.2. The details of those check computations, in particular the reduction of the vibronic space to a manageable size, have been reported in Ref.[85] and will not be discussed further. The results of quantum dynamics calculations are reported in Figure 4.4, where the population of the final states as a function of the time is reported.

In quantum dynamics the rate constants is a function of the time, the computed average rate constants are reported in Table 4.3; the predicted average values are in excellent agreement

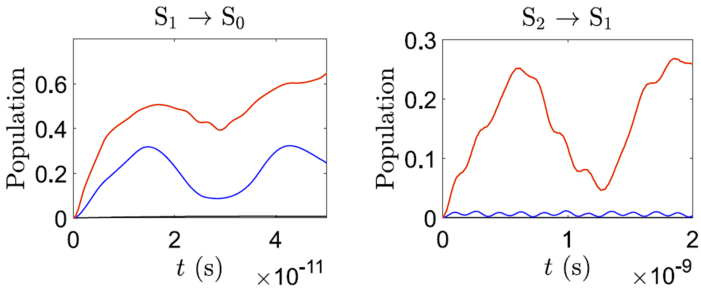

FIGURE 4.4: Total population of the final electronic state as a function of time for $S_1 \rightarrow S_0$ (left) and $S_2 \rightarrow S_1$ (right) transitions, for different subspaces included in dynamics.

with FGR results, being as expected slightly lower than FGR ones. Indeed, as discussed in Chapter 1, FGR neglects the quantum coherence, thus providing always larger rates compared to those obtained by the numerical solution of the Schrödinger equation.

4.2 Intersystem crossing of xanthone

Among small organic molecules, aromatic ketones have emerged as prototypical system exhibiting efficient ISC without the need for heavy atoms. The efficient ISCs occurring in these molecules is largely attributed to the presence of carbonyl groups, which introduce low lying $n \rightarrow \pi$ states that enhance SOC. Indeed, El Sayed selection rules state that ISC is more efficient when the transition involves a change in the type of molecular orbital involved. For instance, ISC involving a $n \longrightarrow \pi^*$ transition

Table 4.3: Energy difference (ΔE, eV) from Ref. [159], calculated IC rate (s^{-1}) from time-dependent perturbation theory (FGR), and from numerical solution of time-dependent Schrödinger equation (QD).

		Rate	
Transition	ΔE	FGR	QD
$S_1 \rightarrow S_0$	1.77	7.1×10^{10}	6.2×10^{10}
$S_2 \rightarrow S_1$	1.73	6.6×10^{8}	6.3×10^{8}

should be characterized by a higher SOC than a $\pi \longrightarrow \pi^*$. The situation is schematized in Figure 4.5.

Benzophenone and xanthone often serve as reference compounds in studying photophysical processes, as ISC dynamics, phosphorescence, and triplet-triplet energy transfer. Here attention will be focused on xanthone molecules, which exhibits high ISC quantum yield, often approaching unity under certain conditions.[137] The efficient ISC is facilitated by El-Sayed's rule, because of a presence of a several triplet states which are at lower energy than S1 one.[41] For this reason, triplet states (T_1 and higher) in xanthone have been extensively characterized, showing long lifetimes (microseconds to milliseconds)[36] suitable for electronic applications and photocatalysis.

Experimentally, xanthone is characterized by extremely efficient ISC: most of the excitation energy funneled into singlet states is converted into triplet population, often with minimal prompt fluorescence yield.[130, 170] In many solvents, the fluorescence quantum yield is vanishingly small ($\sim 10^{-4}$), pointing

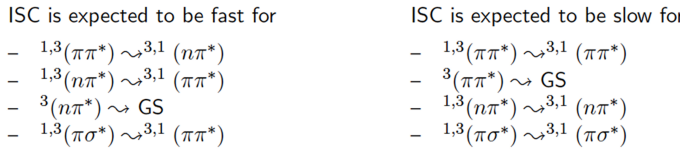

FIGURE 4.5: Schematic representation of El-Sayed rule

to dominant nonradiative channels. Interestingly, in aqueous solution, xanthone shows a markedly enhanced fluorescence output, attributable to a delayed fluorescence component that likely involves reverse processes from the triplet manifold back to the singlet manifold.[36, 125, 137, 31, 54, 64]

Given these remarkable features, xanthone offers an ideal system to for testing the reliability of state of art quantum mechanical approaches to non-adiabatic dynamics. Theoretical studies are of fundamental importance for understanding the photophysics of xanthone, providing essential information about energy position and electronic character of the singlet and triplet excited states, spin-orbit couplings among them, and finally even transition rates for comparing competitive decay pathways.[129, 106, 7]

TDDFT calculations indicate that xanthone nuclear geometry exhibits C_{2v} symmetry, and this symmetry is preserved in both its singlet and triplet excited states. The first excited singlet state of xanthone (S_1) is the dark $^1A_2$ state with a $n\pi^*$ characther, due to the promotion of a non-bonded electron from the oxygen to the antibonding π^* state. The second excited single S_2 is the light $^1A_1$ state with $\pi\pi^*$ character. The first and

second triplet states, T_1 and T_2, exhibit a similar ordering and character as their corresponding singlet states.

Table 4.4: Total SOC (cm^{-1}) between the S_2 and S_1 states and the first four triplet excited states, and energy difference between the corresponding single states (ΔE , eV) and each triplet state.

	S_2			
	T_1	T_2	T_3	T_4
SOC	20.265264	0.000000	0.000000	1.396763
ΔE	1.29	1.11	0.61	0.41
	S_1			
	T_1	T_2	T_3	T_4
SOC	0.000000	60.676860	14.681863	2.174148
ΔE	0.62	0.44	0.12	0.32

Under normal condition, xanthone is not a fluorescent molecule.[54, 129] This suggests that the relaxation of S_2 state proceeds entirely through non-radiative decay pathways. The depopulation of S_2 can occur via: IC to the lower-lying singlet state S_1, or ISC to one of the triplet manifold (T_n). As indicated by the SOC values summarized in Table 4.4, ISC from S_2 to the first triplet state (T_1) is, in principle, possible. However, the substantial energy gap between these two electronic states significantly reduces the probability of this transition, rendering it an inefficient deactivation route.

In contrast, the IC process from S_2 to S_1 is energetically more favorable, making it the dominant relaxation pathway. Based on

the methodology outlined in Chapter 1, the rate constant for this IC process is 1.6×10^{-12} s, whereas the ISC process has a much lower rate constant of 1.5×10^{-10} s. These findings indicate that internal conversion significantly outcompetes intersystem crossing during the deactivation of the S_2 state, leading to rapid population of S_1 before any substantial triplet formation occurs. From the S_1 state, ISC to the T_2 state proceeds rapidly, with a

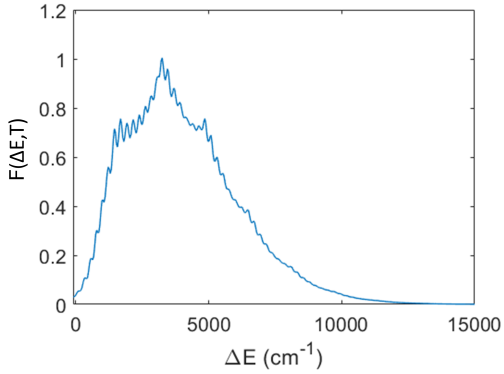

FIGURE 4.6: $F(\Delta E, T)$ (eq. 1.43) at T= 298 K of the $S_2 \rightarrow S_1$ internal conversion as a function of energy difference between the initial and final state of gas-phase xanthone. $F(\Delta E, T)$ is obtained via inverse Fourier transform (IFFT) of $f(\lambda)$ in eq. 1.102 (see Appendix C).

rate constant $k_{ISC} = 5.7 \times 10^{-11}$ s. Subsequently, the population of the T_1 state occurs via IC from T2, with a rate constant $k_{IC} = 1.7 \times 10^{-13}$ s.

The IC between the two triplet states is found to be significantly faster than the corresponding singlet transition. Consequently, the experimentally observed triplet-state formation,

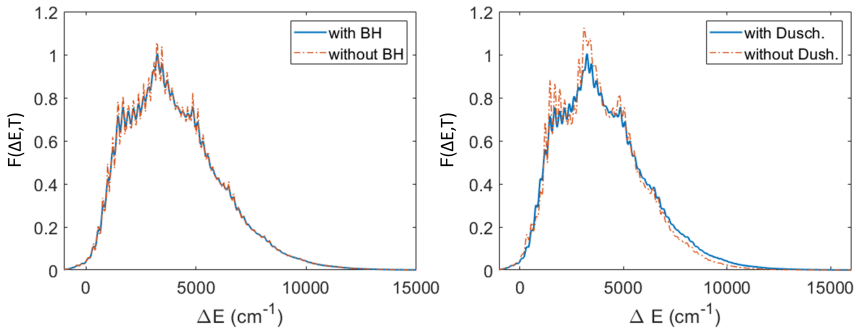

FIGURE 4.7: $F(\Delta E, T)$ as in Figure 4.6. Here are shown : (right) the negligible Duschinsky's effect where the $F(\Delta E, T)$ computed by posing $\mathbf{J} = \mathbf{I}$, whit $\mathbf{I}$ is the identity matrix; (left) the negligible effect of the Blackman-Harris window function used in the sampling of $f(\lambda)$ (eq. 1.102)

monitored through time-resolved triplet excited-state absorption spectroscopy [31], is more accurately attributed to the formation of T_2, as the ISC rate from S_1 is the rate-determining step. Consequently, the overall population of the triplet state follows a sequential mechanism: an initial IC from S_2 to S_1, followed by ISC from S_1 to T_2.

This two-step process ($S_2 \rightarrow S_1 \rightarrow T_2$) represents the dominant pathway leading to triplet formation in xanthone, consistent with its experimentally observed ultrafast ISC and negligible fluorescence yield.[54, 7] The efficiency of this mechanism underscores the strong electronic coupling and favorable energetic alignment that promote rapid non-radiative transitions, ultimately resulting in the near-instantaneous population of the triplet manifold after photoexcitation.

Table 4.5: Wavenumbers (ω, cm^{-1}) of the initial electronic state, equilibrium position displacements (**K**, absolute values, Å x $amu^{1/2}$) and non-adiabatic coupling projected over the normal modes (NAC, $bohr^{-1} \times amu^{1/2}$) for the $S_2 \rightarrow S_1$ and $T_2 \rightarrow T_1$ transitions of xanthone

$\mathbf{S_2 \longrightarrow S_1}$			$\mathbf{T_2 \longrightarrow T_1}$		
ω_2	**K**	NAC	ω_2	**K**	NAC
229.8222	-0.4824	-0.0048	223.0685	-0.1860	0.0017
442.1212	0.0090	-0.0898	393.5265	-0.0404	0.0177
518.6209	-0.1965	-0.0046	503.3441	-0.0298	-1.246e-06
697.8248	-0.1694	-0.0020	644.0867	0.0697	-0.0432
705.1256	0.0716	0.0354	694.3709	-0.0216	-0.0015
841.95125	0.0478	0.0079	817.7266	0.0499	0.0002
1053.0450	0.0772	0.0081	926.4843	0.0871	-0.0010
1123.3832	0.0236	0.0100	1051.1471	-0.0091	0.0002
1192.4883	0.0288	0.0231	1130.5506	-0.0156	0.0351
1220.6347	-0.0600	-0.0292	1176.1201	0.0134	-0.0404
1242.0174	0.0083	-0.0197	1215.6089	0.0042	-0.0681
1304.9577	0.0490	0.0371	1279.1787	0.0153	-0.0043
1361.9002	0.0484	-0.0098	1405.5059	-0.0047	0.0051
1450.7422	-0.0236	0.0351	1496.8199	-0.0018	0.1315
1490.1678	0.0135	0.0202	1506.8813	-0.0067	-0.0001
1598.6306	0.0520	0.0691	1585.0487	-0.0034	0.0161
1605.06260	-0.0258	0.0077	1625.2985	-0.0193	0.2055

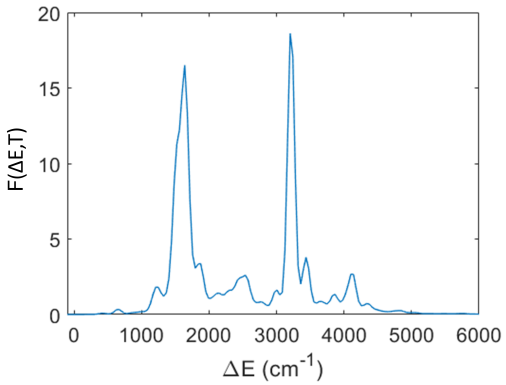

FIGURE 4.8: $F(\Delta E, T)$ (eq. 1.43) at T= 298 K of the $T_2 \rightarrow T_1$ internal conversion as a function of energy difference between the initial and final state of gas-phase xanthone.

Importantly, the theoretical determination of the kinetic constants for both non-radiative processes (IC and ISC) using the model proposed in Chapter 1 shows excellent agreement with experimental observations, reinforcing the reliability and predictive capability of the adopted methodology. In particular, the calculated k_{IC} value (1.6×10^{-12} s) of singlet excited states ${}^1\pi\pi^* \rightarrow {}^1 n\pi^*$ closely reproduce the experimental values reported by Cavaleri and coworkers of 2.3×10^{-12} s. Similarly, k_{ISC} (${}^1n\pi^* \rightarrow {}^3 \pi\pi^*$) = 5.7×10^{-11} are in excellent agreement with the experimental rate ($\sim 1 \times 10^{-11}$).[31] This strong correspondence between theoretical and experimental data confirms that the computational framework accurately captures the fundamental photophysical behavior of xanthone and validates its applicability for describing excited-state dynamics in related aromatic carbonyl systems.

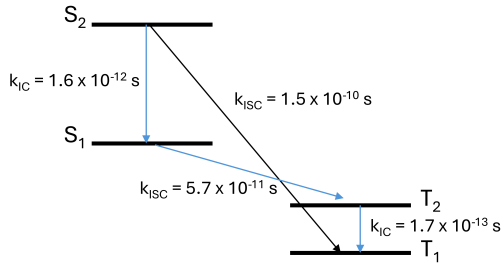

FIGURE 4.9: Non radiative decays between singlet and triplet states of xanthone molecule in gas phase.

Chapter 5

Computational Details

5.1 Computational details for Chapter 3 and Chapter 5

All quantum chemical calculations were performed using the Gaussian 16 package [48] and the Q-Chem program [140]. Ground-state geometries and harmonic frequencies were optimized at the density functional theory (DFT) level [56] using the B3LYP functional [15, 89] with the 6-31+G(d,p) basis set. For larger molecular systems, the CAM-B3LYP long-range corrected functional [171] was employed with the same basis set to provide an improved description of charge-transfer and Rydberg states.

Excited-state calculations were carried out using time dependent DFT (TDDFT) under the same computational conditions. When appropriate, solvent effects were included through the polarizable continuum model (PCM) [157] to account for dielectric stabilization of electronic states.

Non-adiabatic coupling (NAC) elements were computed at the TDDFT level with the same functional and basis set

using Q-Chem,[140] following standard linear-response formalism.[93] Spin–orbit couplings (SOC) were evaluated analogously within the same framework, adopting the mean-field one-electron spin–orbit operator.

Franck-Condon weighted densities of states have been computed by using a development version of MolFC package, available on request. The set of coupled ODEs has been solved by using the Dormand-Price method of order 4, a member of the Runge-Kutta family of ODE solvers, as implemented in the MATLAB package.[63]

5.2 Computational details for Chapter 4

Classical MD simulation were performed with a QM-derived force filed[80, 117, 82] on an atomistic model of liquid solvent using the GROMACS 2020.5 software.[1] For the liquid THF was considered a cubic supercell with side a = 20 Å containing 60 THF molecules (780 atoms), corresponding to the density at room temperature of 0.88 g/cm^3. To refer the electronic structure of liquid THF with respect to the vacuum level, the simulation cell was expanded in one direction to include 40 Å of vacuum ($a = b$ = 20 Å and c = 60 Å). When NAP was inserted, it was placed in the center of the supercell and one THF molecule was removed to acomodate the solute and preserve solvent density. For each MD simulation, was performed an initial steepest descent minimization, followed by a slow NVT heating procedure to 298 K. After equilibrating the system at the target temperature in NVT conditions for 0.5 ns, were

carried out production runs in NPT conditions for liquid THF and in NVT conditions for the solutions with NAP. MD runs lasted for 2 ns. The same procedure was adopted also for the acenes considering a cubic cell 2 x 2 x 2. The electronic-structure calculations were performed at the hybrid DFT level on top a set of 100 MD structural configurations equally spaced in time, one each 10 ps of simulation. It was adopted the Koopmann's compliant density functional theory (FC-DFT) derived from the PBE0 hybrid functional. [2, 124] To determine the proper Fock exchange (α_K) a fluorine atom was inserted in a MD-structural configuration of the atomistic model for liquid THF, thus introducing a localized state in the energy gap of the liquid. Then, it was computed the single-particle energy level for the neutral system (F) and for the negative system upon vertical injection of an electron (F^-) at the PBE level of theory with different value of α. α_K was found by intersaction between the linear evolution of the single-particle energy levels for the neutral and anionic system producing α_K = 52 %. Non local dispersions were included via the self-consisten rVV10 method.[164, 134] All the calculations were performed with the CP2K suite of programs,[161] using MOLOPT double-zeta polarized basis set.

The electronic finite size corrections $E_{\text{corr}}(-1, R_{-1})$ and $E_{\text{corr}}(-1, R_0)$ were evaluated via the scheme first developed by Freysoldt, Neugebauer, and Van de Walle (FNV).[47, 74, 42] The first term features two contributions: (i) the Madelung energy, accounting for the monopole charge subject to periodic boundary conditions and screened by the static dielectric constant ϵ_0 of the bulk medium ; (ii) an alignment-like term due

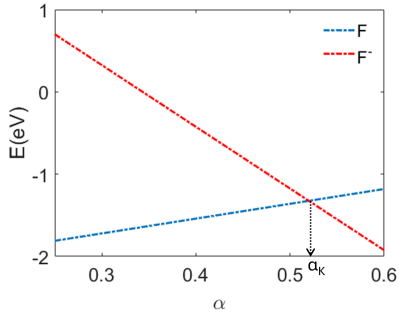

FIGURE 5.1: Intersection between linear evolution of the single-particle energy levels for the neutral (blue) and anionic (red) system for the determination of α_K.

to the finite extent of the charge distribution.[47, 74, 42]. The term $E_{\text{corr}}(-, R_0)$ corrects the energy of the vertically charged supercell after injection of an electron into neutral NAP (R_0). In this case, the charge is considered to be screened by the high-frequency dielectric constant ϵ_∞ of THF. Finally, $E_{\text{corr}}(0, R_-)$ corrects the total energy of neutral supercell achieved upon vertical removal of an electron.

DFT calculations for NAP nad NAP^- with an implicit description of the solvent were carried out with the Gaussian16 software employing the B3LYP functional with the 6-31+G(d,p) basis set.Dielectric effects were included in the computations by using the polarizable continuum model (PCM). Solvent reorganization energy was evaluated using the non-equilibrium PCM methods, as implemented in Gaussian16.

Chapter 6

Concluding Remark

The research presented in this thesis establishes a comprehensive and quantitatively rigorous theoretical framework for describing both radiative and non-radiative processes in molecular systems, integrating advanced electron transfer theory, quantum dynamics, and explicit solvent modeling. At its core, the work extends the generating function formalism to compute transition rates via Fermi's Golden Rule, providing a unified treatment of radiative and non radiative processes. This approach explicitly accounts for the coupling between electronic states and nuclear vibrations, enabling mechanistically transparent and quantitatively accurate predictions of exciton relaxation pathways. The model reproduces experimental observables across diverse molecular configurations, highlighting its predictive reliability and versatility.

A novel aspect of this work concerns the context of electron transfer reactions. Semiclassical Marcus theory, though widely used, is inherently limited by its classical nuclear treatment and its reliance on a single harmonic reaction coordinate, which together restrict its ability to describe ultrafast or strongly

quantum-mechanical regimes. Because it neglects quantum effects, the model is unable to reproduce the temperature dependence of electron-transfer rates and can predict rates that deviate by orders of magnitude from experimental measurements. A central and novel contribution of this thesis is the development of a multistep model for electron transfer that is fundamentally based on the adiabatic separation of solvent and nuclear motions. Unlike previous approaches, this framework explicitly leverages the distinct time scales of the two motions to justify a stepwise description of the reaction: the faster solvent reorganizes around fixed nuclear coordinates to create an energetically favorable configuration for electron tunneling, followed by electron transfer driven by nuclear motion, and concluded by the adiabatic relaxation of the solvent to the product equilibrium configuration. This innovative use of solvent and nuclear motion separation as the guiding principle not only provides a mechanistic understanding of electron transfer dynamics but also enables accurate predictions of activation barriers, reorganization energies, and electronic couplings, bridging molecular-level theory with experimental kinetics in a way that traditional semiclassical or single-step models cannot.

Application of the model to a diverse set of experimental systems demonstrates quantitative agreement with measured electron transfer rates and their temperature dependence, validating both its robustness and predictive power. Unlike traditional semiclassical or single-step theories, which can fail under certain conditions, the framework provides mechanistic insight

into the influence of donor-acceptor energetics, vibrational coupling, and solvent reorganization on charge transfer efficiency. The cases studied encompass regimes that often challenge other models, including strongly exergonic reactions, wide temperature ranges, solvents with varying dielectric constants, and both fast and slow reactions, and in all instances, the proposed model accurately reproduces experimental trends, demonstrating its broad applicability and generality.

The predictive capability of the model facilitates a more rigorous exploration of structure–property relationships, guiding the design of molecules and polymers with tailored photophysical and electronic properties. It provides a computationally tractable yet physically rigorous methodology to interpret experimental observations and to anticipate the behavior of novel molecular motifs, and donor-acceptor combinations prior to synthesis. This capacity is particularly relevant for the development of next-generation optoelectronic devices, including OLEDs with enhanced quantum yields, organic solar cells with minimized recombination losses, and flexible or large-area devices where molecular packing and environmental interactions play a decisive role.

By enabling the rational tuning of radiative and non-radiative pathways, this work lays the foundation for the accelerated discovery, design, and optimization of organic materials that combine efficiency, stability, and tunability, addressing key challenges in the development of advanced optoelectronic technologies.

Looking ahead, the multistep electron transfer framework

developed in this thesis offers a powerful platform for the rational design and optimization of donor-acceptor systems and charge-transfer materials. By linking mechanistic understanding of solvent and nuclear dynamics with predictive modeling, this approach can guide the development of high-performance, stable, and tunable materials. These advances demonstrate the potential of combining rigorous theoretical modeling with molecular design principles to enable next-generation energy conversion, catalysis, and optoelectronic technologies.

Appendix A

First Order Time Dependent Perturbation Theory (TDPT)

Let $|\psi_i\rangle$ the wavefunction describind the system in a certain initial condition and $|\psi_f\rangle$ the wavefunction describing the system after a certain time t. Let $|\Psi(t)\rangle$ be the representation of the wavefunction at time t, according to the superposition principle we can write :

$$|\Psi(t)\rangle = \sum_j c_j(t)\,|\psi_j(t)\rangle \tag{A.1}$$

where $|\psi_j(t)\rangle$ represents the set of stationary states of unperturbed hamiltonian $\hat{\mathcal{H}}^0$, with time dependence given by:

$$|\psi_j(t)\rangle = e^{-E_j^0 t/\hbar}\,|\psi_j\rangle \tag{A.2}$$

and $|\psi_j\rangle$ the spatial wavefunction. $|\Psi(t)\rangle$ must of course statisfied the time dependent Schrödinger equation, so that

$$i\hbar\frac{\partial}{\partial t}\Big[\sum_j c_j(t)e^{-E_j^0 t/\hbar}\,|\psi_j\rangle\Big] = \Big(\hat{\mathcal{H}}^0 + \hat{\mathcal{H}}'\Big)\Big[\sum_j c_j(t)e^{-E_j^0 t/\hbar}\,|\psi_j\rangle\Big] \tag{A.3}$$

and so

$$\begin{aligned} i\hbar\Big[\sum_j \frac{\partial}{\partial t}c_j(t)e^{-E_j^0 t/\hbar}\left|\psi_j\right\rangle + \sum_j c_j(t)\frac{\partial}{\partial t}e^{-E_j^0 t/\hbar}\left|\psi_j\right\rangle\Big] = \\ \hat{\mathcal{H}}^0\Big[\sum_j c_j(t)e^{-E_j^0 t/\hbar}\left|\psi_j\right\rangle\Big] + \hat{\mathcal{H}}'\Big[\sum_j c_j(t)e^{-E_j^0 t/\hbar}\left|\psi_j\right\rangle\Big] \end{aligned} \tag{A.4}$$

Since

$$\frac{\partial}{\partial t}e^{-E_j^0 t/\hbar} = -\frac{iE_j^0}{\hbar}e^{-E_j^0 t/\hbar} \tag{A.5}$$

$$\begin{aligned} i\hbar\sum_j \dot{c}_j(t)e^{-iE_j^0 t/\hbar}\left|\psi_j\right\rangle + i\hbar\sum_j c_j(t) - \frac{iE_j^0}{\hbar}e^{-iE_j^0 t/\hbar}\left|\psi_j\right\rangle = \\ = \sum_j c_j(t)e^{-iE_j^0 t/\hbar}\hat{\mathcal{H}}^0\left|\psi_j\right\rangle + \sum_j c_j(t)e^{-iE_j^0 t/\hbar}\hat{\mathcal{H}}'\left|\psi_j\right\rangle \end{aligned} \tag{A.6}$$

$$\begin{aligned} i\hbar\sum_j \dot{c}_j(t)e^{-iE_j^0 t/\hbar}\left|\psi_j\right\rangle + \sum_j c_j(t)E_j^0 e^{-iE_j^0 t/\hbar}\left|\psi_j\right\rangle = \\ = \sum_j c_j(t)e^{-iE_j^0 t/\hbar}\hat{\mathcal{H}}^0\left|\psi_j\right\rangle + \sum_j c_j(t)e^{-iE_j^0 t/\hbar}\hat{\mathcal{H}}'\left|\psi_j\right\rangle \end{aligned} \tag{A.7}$$

but $\hat{\mathcal{H}}^0\left|\psi_j\right\rangle = E_j^0\left|\psi_j\right\rangle$ so we can simplify the quantities $\sum_j c_j(t)E_j^0 e^{-iE_j^0 t/\hbar}\left|\psi_j\right\rangle$ to the first and second sides of the eq.A.7 which becomes:

$$i\hbar\sum_j \dot{c}_j(t)e^{-iE_j^0 t/\hbar}\left|\psi_j\right\rangle = \sum_j c_j(t)e^{-iE_j^0 t/\hbar}\hat{\mathcal{H}}'\left|\psi_j\right\rangle \tag{A.8}$$

Multiply both sides of eq. A.8 by $\langle\psi_f|$ and using the eigenstates orthonormality, $\langle\psi_f|\psi_j\rangle = \delta_{f,j}$,

$$i\hbar \sum_j \sum_f \dot{c}_j(t) e^{-iE_j^0 t/\hbar} \delta_{f,j} = \sum_j \sum_f c_j(t) e^{-iE_j^0 t/\hbar} \langle\psi_f| \hat{\mathcal{H}}' |\psi_j\rangle \tag{A.9}$$

$$i\hbar \dot{c}_f(t) e^{-iE_f^0 t/\hbar} = \sum_j c_j(t) e^{-iE_j^0 t/\hbar} \langle\psi_f| \hat{\mathcal{H}}' |\psi_j\rangle \tag{A.10}$$

$$\dot{c}_f(t) = -\frac{i}{\hbar} \sum_j c_j(t) e^{-i(E_j^0 - E_f^0)t/\hbar} \langle\psi_f| \hat{\mathcal{H}}' |\psi_j\rangle \tag{A.11}$$

Setting

$$\frac{E_f^0 - E_j^0}{\hbar} = \omega_{f,j} \tag{A.12}$$

$$\dot{c}_f(t) = -\frac{i}{\hbar} \sum_j c_j(t) e^{i\omega_{f,j} t} \langle\psi_f| \hat{\mathcal{H}}' |\psi_j\rangle \tag{A.13}$$

Upon condition that $\langle\psi_f| \hat{\mathcal{H}}' |\psi_j\rangle << |E_f - E_i|$, it is possible to afford an iterative solution. At zero order, that is no perturbation :

$$\dot{c}_f(t) \equiv \dot{c}_f(t)^{(0)} = 0 \tag{A.14}$$

which means $c_f^{(0)}(t)$ is constant. To order greater than zero, assume tat at time $t = 0$ the system is in initial state $|\psi_i\rangle$, thus

$$c_i^{(0)} = 1; \qquad c_j^{(0)} = 0 \qquad k \neq i \tag{A.15}$$

By substituting the zero order solution of eq. A.15 in eq. A.13 :

$$\frac{\partial}{\partial t} c_f^{(1)}(t) = -\frac{i}{\hbar} H'_{f,i} e^{i\omega_{f,i} t} \tag{A.16}$$

whose solution is

$$c_f^{(1)}(t) = -\frac{i}{\hbar}\int_{t=0}^{t} \hat{\mathcal{H}}'_{f,i} e^{i\omega_{f,i}t} dt = -\frac{i}{\hbar}\hat{\mathcal{H}}'_{f,i}\frac{e^{i\omega_{f,i}t}}{i\omega_{f,i}} = \frac{\hat{\mathcal{H}}'_{f,i}}{\hbar\omega_{f,i}}(1 - e^{i\omega_{f,i}t}) \tag{A.17}$$

$c_f^{(1)}(t)$ represents the probability amplitude that the system from the state $|\psi_i\rangle$ at time $t = 0$ is in $|\psi_f\rangle$ after a time t as a result of a perturbation $\hat{\mathcal{H}}'$, so the probability P is:

$$P_{i->f} = |c_f^{(1)}(t)|^2 = \left|\frac{\hat{\mathcal{H}}'_{f,i}}{\hbar\omega_{f,i}}(1 - e^{i\omega_{f,i}t})\right|^2 = \left|\frac{\hat{\mathcal{H}}'_{f,i}}{\hbar\omega_{f,i}}\right|^2 2[1 - \cos(\omega_{f,i}t)] \tag{A.18}$$

From the cosin duplication formula we can write

$$P_{i->f} = 4\left|\frac{\hat{\mathcal{H}}'_{f,i}}{\hbar\omega_{f,i}}\right|^2 \sin^2(\omega_{f,i}t/2) \tag{A.19}$$

Multiply and divide for t the second member:

$$P_{i->f} = 4\left|\frac{\hat{\mathcal{H}}'_{f,i}}{\hbar}\right|^2 t\frac{\sin^2(\omega_{f,i}t/2)}{\omega_{f,i}^2 t} \tag{A.20}$$

For $t \to \infty$, the function $\frac{\sin^2(\omega_{f,i}t/2)}{\omega_{f,i}^2 t}$ assumes its maximum value for $\omega_{f,i} = 0$ and vanishes for $\omega_{f,i} \neq 0$, a typical behavior of Dirac's delta function. So:

$$P_{i->f} = 4\left|\frac{\hat{\mathcal{H}}'_{f,i}}{\hbar}\right|^2 t\delta(\omega_{f,i}) \tag{A.21}$$

Note that $P_{i->f} \neq 0 \iff \omega_{f,i} \simeq 0$ and so $E_f^0 \simeq E_i^0$. This result indicates that the transition is possible if and only if the two states are approximately degenerate as required by the principle of energy conservation.
If there is a manifold of final states $|\psi_f\rangle$, the probability is written in term of the density of states ($\rho(\Delta E_{f,i})$), i.e

$$\sum_f P_{f\leftarrow i} = \int P_{f\leftarrow i}\rho(\Delta E_{f,i})d\Delta E_{f,i} \tag{A.22}$$

Since $d\Delta E_{f,i} = \hbar d\omega_{f,i}$

$$\begin{aligned} &\int P_{f\leftarrow i}\rho(\Delta E_{f,i})d\Delta E_{f,i} \\ &= \frac{4}{\hbar^2}\int |\hat{\mathcal{H}}'_{f,i}|^2 t\frac{\sin^2(\omega_{f,i}t/2)}{\omega_{f,i}^2 t}\rho(\omega_{f,i})\hbar d\omega_{f,i} \\ &= \frac{4}{\hbar}|\hat{\mathcal{H}}'_{f,i}|^2\rho(\omega_{f,i})\int \frac{\sin^2(\omega_{f,i}t/2)}{\omega_{f,i}^2}d\omega_{f,i} \end{aligned} \tag{A.23}$$

wherin we assume $\hat{\mathcal{H}}'_{f,i}$ indipendent of time.
In the equation above two important assumption have been made :

- $\rho(\Delta E_{f,i})$ varies slowly with frequency ($\hbar\omega_{f,i} << t$) and there is a continuum of final state ;

- $\hat{\mathcal{H}}'_{f,i}$ is invariant across the final states

The integral in eq.A.23 can be solved with a change of variable:

$$\frac{\omega_{f,i}t}{2} = u \qquad d\omega_{f,i} = \frac{2}{t}du \tag{A.24}$$

$$\begin{aligned}\int P_{f\longleftarrow i}\rho(\Delta E_{f,i})d\Delta E_{f,i} = \frac{4}{\hbar}|\hat{\mathcal{H}}'_{f,i}|^2\rho(\omega_{f,i})\int\frac{\sin^2(u)}{4u^2}t^2\frac{2}{t}du = \\ = \frac{2}{\hbar}|\hat{\mathcal{H}}'_{f,i}|^2\rho(\omega_{f,i})t\int\frac{\sin^2(u)}{u^2}du = \\ \frac{2\pi}{\hbar}|\hat{\mathcal{H}}'_{f,i}|^2\rho(\omega_{f,i})t\end{aligned} \tag{A.25}$$

where we have used the identity :

$$\int\frac{\sin^2(u)}{u^2}du = \pi \tag{A.26}$$

The rate of transition is defined as the time derivative of P and thus, we finally arrive to the Fermi's Golden Rule (FGR),

$$K_{f\longleftarrow i} = \frac{2\pi}{\hbar}|\hat{\mathcal{H}}'_{f,i}|^2\rho(\omega_{f,i}) \tag{A.27}$$

Appendix B

Gaussian Integrals

Let $\mathbf{x}$ a $n \times 1$ vector and $\mathbf{A}$ a n x n symmetric matrix. Let the integral Z defined as :

$$Z = \int_{\Re^n} d^n\mathbf{x} \exp\Big[-\frac{1}{2}\mathbf{x}^T\mathbf{A}\mathbf{x}\Big] \tag{B.1}$$

with

$$\mathbf{x} = \begin{pmatrix} x_1 \\ x_2 \\ \vdots \\ x_n \end{pmatrix} \tag{B.2}$$

$\det(\mathbf{A}) \neq 0$, and $\mathbf{A} = \mathbf{A}^T \in \Re^{n\times n}$ thus $\mathbf{A}$ has eigenvalues $\lambda_i \in \Re$ and can be diagonalized in a matrix D=diag($\lambda_1, \lambda_2, ...,$) by an ortogonal matrix $\mathbf{O}$, i.e

$$\mathbf{D} = \mathbf{O}\mathbf{A}\mathbf{O}^T = \begin{pmatrix} \lambda_1 & 0 & 0 & \cdots \\ 0 & \lambda_2 & 0 & \cdots \\ \vdots & & & \\ 0 & 0 & \cdots & \lambda_n \end{pmatrix} \tag{B.3}$$

The integral Z can be written as :

$$\begin{aligned} \int d^n x \exp\Big[-\frac{1}{2}x^T \mathbf{A} x\Big] = \\ \int d^n x \exp\Big[-\frac{1}{2}x^T \mathbf{O}^T \mathbf{D} \mathbf{O} x\Big] = \\ \int d^n x \exp\Big[-\frac{1}{2}(\mathbf{O}x)^T \mathbf{D} (\mathbf{O}x)\Big] \end{aligned} \tag{B.4}$$

The integration can be performed with a change of variables. Putting

$$\begin{aligned} \mathbf{y} &= \mathbf{O}\mathbf{x} \\ d^n \mathbf{y} &= \det\Big(\frac{d\mathbf{y}}{d\mathbf{x}}\Big) d^n \mathbf{x} \\ d^n \mathbf{x} &= \frac{1}{\det(\mathbf{O})} d^n \mathbf{y} \end{aligned} \tag{B.5}$$

the integral Z becomes

$$\begin{aligned} \int d^n \mathbf{y} \frac{1}{\det(\mathbf{O})} \exp\Big[-\frac{1}{2}\mathbf{y}^T \mathbf{D} \mathbf{y}\Big] = \\ \int d^n \mathbf{y} \frac{1}{\det(\mathbf{O})} \exp\Big[\sum_{i=1}^{n} \lambda_i y_i^2\Big] = \\ \frac{1}{\det(\mathbf{O})} \prod_{i=1}^{n} \int_{-\infty}^{+\infty} dy_i \exp\Big[-\frac{1}{2}\lambda_i y_i^2\Big] \end{aligned} \tag{B.6}$$

Note that

$$\int_{-\infty}^{+\infty} \exp\Big[-\frac{\alpha}{2}x\Big] dx = \sqrt{\frac{2\pi}{\alpha}} \tag{B.7}$$

Z is

$$\begin{aligned} Z = \frac{1}{\det(\mathbf{O})} \prod_{i=1}^{n} \sqrt{\frac{2\pi}{\lambda_i}} = \\ \frac{1}{\det(\mathbf{O})} \frac{(2\pi)^{n/2}}{\sqrt{\det(\mathbf{D})}} = \\ \frac{(2\pi)^{n/2}}{\sqrt{\det(\mathbf{O}^T\mathbf{D}\mathbf{O})}} = \\ \frac{(2\pi)^{n/2}}{\sqrt{\det(\mathbf{A})}} \end{aligned} \tag{B.8}$$

If I is a multidimensional integral of the form :

$$I_{ij} = \int_{\Re^n} d^n\mathbf{x} x_i x_j \exp\Big[-\frac{1}{2}\mathbf{x}^T\mathbf{A}\mathbf{x}\Big] \tag{B.9}$$

we can use the generating function $Z[J]$:

$$Z[J] = \int d^n\mathbf{x} \exp\Big[-\frac{1}{2}\mathbf{x}^T\mathbf{A}\mathbf{x} + \mathbf{x}^T\mathbf{J}\Big] \tag{B.10}$$

and compute I as :

$$I_{ij} = \frac{\partial^2 Z[J]}{\partial J_i \partial J_j}\Big|_{J=0} \tag{B.11}$$

with

$$J = \begin{pmatrix} J_1 \\ J_2 \\ \vdots \\ J_n \end{pmatrix} \tag{B.12}$$

Completing the square

$$Z[J] = \int d^n\mathbf{x} \exp\Big[-\frac{1}{2}(\mathbf{x}-\mathbf{A}^{-1}\mathbf{J})^T\mathbf{A}(x-\mathbf{A}^{-1}\mathbf{J}) + \frac{1}{2}\mathbf{J}^T\mathbf{A}^{-1}\mathbf{J}\Big] \tag{B.13}$$

change the variable:

$$\begin{aligned} \mathbf{y} &:= \mathbf{x} - \mathbf{A}^{-1}\mathbf{J} \\ Z[J] &= \int d^n\mathbf{y} \exp\Big[-\frac{1}{2}\mathbf{y}^T\mathbf{A}\mathbf{y} + \frac{1}{2}\mathbf{J}^T\mathbf{A}^{-1}\mathbf{J}\Big] \\ &\exp\Big[\frac{1}{2}\mathbf{J}^T\mathbf{A}^{-1}\mathbf{J}\Big] \int d^n\mathbf{y} \exp\Big[-\frac{1}{2}\mathbf{y}^T\mathbf{A}\mathbf{y}\Big] \\ &\exp\Big[\frac{1}{2}\mathbf{J}^T\mathbf{A}^{-1}\mathbf{J}\Big] \frac{(2\pi)^{n/2}}{\sqrt{\det(\mathbf{A})}} \end{aligned} \tag{B.14}$$

but

$$I_{ij} = \frac{\partial^2 Z[J]}{\partial J_i \partial J_j}\Big|_{J=0} \tag{B.15}$$

so

$$I = \frac{(2\pi)^{n/2}}{\sqrt{\det(\mathbf{A})}} \frac{\partial^2}{\partial J_i \partial J_j} \exp\Big[\frac{1}{2}\mathbf{J}^T\mathbf{A}^{-1}\mathbf{J}\Big]\Big|_{J=0} \tag{B.16}$$

Since

$$\mathbf{J}^T\mathbf{A}^{-1}\mathbf{J} = \sum_{k=1}^{n}\sum_{l=1}^{n}(A^{-1})_{lk}J_kJ_l \tag{B.17}$$

and

$$Z_0 := Z[0] = \frac{(2\pi)^{n/2}}{\sqrt{\det(\mathbf{A})}} \tag{B.18}$$

thus

$$
\begin{aligned}
I_{ij} &= Z_0 \frac{\partial^2}{\partial J_i \partial J_j} \exp\Big[\frac{1}{2}\sum_{k=1}^{n}\sum_{l=1}^{n}(A^{-1})_{lk}J_kJ_l\Big]\Big|_{J=0} \\
&= Z_0 \frac{\partial}{\partial J_j}\Big\{\Big(\frac{1}{2}\sum_{a=1}^{n}(A^{-1})_{ai}J_a + \frac{1}{2}\sum_{b=1}^{n}(A^{-1})_{ib}J_b\Big) \\
&\qquad \times \exp\Big[\frac{1}{2}\sum_{k=1}^{n}\sum_{l=1}^{n}(A^{-1})_{kl}J_kJ_l\Big]\Big\}\Big|_{J=0} \\
&= Z_0 \frac{\partial}{\partial J_j}\Big\{\sum_{a=1}^{n}(A^{-1})_{ia}J_a \exp\Big[\frac{1}{2}\sum_{k=1}^{n}\sum_{l=1}^{n}(A^{-1})_{kl}J_kJ_l\Big]\Big\}\Big|_{J=0} \\
&= Z_0\Big\{(A^{-1})_{ij} + \sum_{a=1}^{n}(A^{-1})_{ia}J_a\Big(\frac{1}{2}\sum_{b=1}^{n}(A^{-1})_{bj}J_b + \frac{1}{2}\sum_{c=1}^{n}(A^{-1})_{jc}J_c\Big)\times \\
&\qquad \exp\Big[\frac{1}{2}\sum_{k=1}^{n}\sum_{l=1}^{n}(A^{-1})_{kl}J_kJ_l\Big]\Big\}\Big|_{J=0} \\
&= Z_0\Big[(A^{-1})_{ij} + \sum_{a=1}^{n}(A^{-1})_{ia}J_a\sum_{b=1}^{n}(A^{-1})_{bj}J_b\Big]\exp\Big[\frac{1}{2}\mathbf{J}^T\mathbf{A}^{-1}\mathbf{J}\Big]\Big|_{J=0} \\
&= Z_0(A^{-1})_{ij}
\end{aligned}
\tag{B.19}
$$

Appendix C

Numerical calculation of $F(\Delta E, T)$

Continuous functions describing molecular properties often need to be represented in a discrete form for numerical evaluation or further analysis. Proper sampling of these functions is essential to accurately capture their behavior and to prevent distortions, such as aliasing, that can occur if the sampling resolution is insufficient.

Let $F(s)$ be a function defined in the Laplace domain. For numerical evaluation of its time-domain representation, it is advantageous to exploit the relationship between the Laplace and Fourier transforms. Specifically, by evaluating $F(s)$ along the imaginary axis ($s = j\omega$), one obtain the Fourier transform of the function:

$$F(j\omega) = F(s)|_{s=j\omega} \tag{C.1}$$

This is particularly convenient because the resulting frequency-domain samples can be directy handled using efficient discrete algorithms such as the Fast Fourier Transform (FFT) and its

inverse (IFFT). In this way, the discrete set of values can be treated as a Fourier spectrum, which allows the time-domain function to be reconstructed numerically with the IFFT.
According to the Nyquist–Shannon sampling theorem, if the maximum significant frequency component of $F(s)$ is f_{max}, the sampling frequency f_s must satisfy:

$$f_s \geq 2f_{max} \tag{C.2}$$

to ensure accurate reconstruction. The corresponding discrete-time samples of the function in the frequency domain are:

$$F[n] = F(j\omega_n), \qquad \omega_n = n\Delta\omega, \qquad n = 0, 1, ..., N-1 \tag{C.3}$$

where $\Delta\omega$ is the frequency increment and N is the total numeber of sampled points. For efficient computation using FFT and IFFT algorithms, it is advantageous to choose N as a power of two, i.e., $N = 2^n$, since this maximizes the performance of the FFT routine in numerical environments.
Truncate a sampled spectrum to a finite number of points can introduce spectral leakage, particularly when performing inverse transformations. To mitigate this effect, a window function $w[n]$ can be applied to the discrete samples:

$$f_w[n] = F[n] \cdot w[n], \qquad n = 0, 1, ..., N-1 \tag{C.4}$$

The application of a window function smooths the edges of the sampled interval, reducing artifacts in the reconstructed time-domain signal.

Once the discrete and windowed spectrum $F_w[n]$ is obtained, the corresponding time-domain sequence can be computed efficiently using the IFFT. Thus, by carefully selecting the sampling frequency, the numerical inversion yields an accurate reconstruction of the time-domain signal. In this way the $F(\Delta E, T)$ of Section 1.3 is obtained.

Bibliography

[1] Mark James Abraham et al. "GROMACS: High Performance Molecular Simulations Through Multi-Level Parallelism from Laptops to Supercomputers". In: *SoftwareX* 1-2 (2015), pp. 19–25. DOI: 10.1016/j.softx.2015.06.001.

[2] Carlo Adamo and Vincenzo Barone. "Toward Reliable Density Functional Methods without Adjustable Parameters: The PBE0 Model". In: *J. Chem. Phys.* 110.13 (1999), pp. 6158–6170. DOI: http://dx.doi.org/10.1063/1.478522.

[3] Christopher Adriaanse et al. "Aqueous redox chemistry and the electronic band structure of liquid water". In: *J. Phys. Chem. Lett.* 3.23 (2012), pp. 3411–3415.

[4] Christopher Adriaanse et al. "The electron attachment energy of the aqueous hydroxyl radical predicted from the detachment energy of the aqueous hydroxide anion". In: *J. Am. Chem. Soc.* 131.17 (2009), pp. 6046–6047.

[5] Damian Aherne, Vu Tran, and Benjamin J Schwartz. "Nonlinear, nonpolar solvation dynamics in water: the roles of electrostriction and solvent translation in the

breakdown of linear response". In: *The Journal of Physical Chemistry B* 104.22 (2000), pp. 5382–5394.

[6] Damian Aherne, Vu Tran, and Benjamin J Schwartz. "Nonlinear, nonpolar solvation dynamics in water: the roles of electrostriction and solvent translation in the breakdown of linear response". In: *J. Phys. Chem. B* 104.22 (2000), pp. 5382–5394.

[7] Marc Alías-Rodríguez, Coen de Graaf, and Miquel Huix-Rotllant. "Ultrafast Intersystem Crossing in Xanthone from Wavepacket Dynamics". In: *Journal of the American Chemical Society* 143.51 (2021). PMID: 34905690, pp. 21474–21477. DOI: 10.1021/jacs.1c07039. eprint: https://doi.org/10.1021/jacs.1c07039. URL: https://doi.org/10.1021/jacs.1c07039.

[8] Francesco Ambrosio, Giacomo Miceli, and Alfredo Pasquarello. "Redox levels in aqueous solution: Effect of van der Waals interactions and hybrid functionals". In: *The Journal of chemical physics* 143.24 (2015).

[9] Francesco Ambrosio et al. "Charge Localization in Acene Crystals from Ab Initio Electronic Structure". In: *J. Phys. Chem. Lett.* 14.13 (2023), pp. 3343–3351.

[10] Francesco Ambrosio et al. "External Reorganization Energy upon Charge Transfer Reactions in Mildly Polar Media: The Case of Naphthalene in Tetrahydrofuran". In: *The Journal of Physical Chemistry Letters* 16 (2025), pp. 6734–6744.

[11] Francesco Ambrosio et al. "Quantum Chemical Insights into DNA Nucleobase Oxidation: Bridging Theory and Experiment". In: *Journal of Chemical Theory and Computation* 20.21 (2024), pp. 9708–9719.

[12] Ainhoa Atxabal et al. "Tuning the charge flow between Marcus regimes in an organic thin-film device". In: *Nature Communications* 10.1 (2019), p. 2089.

[13] Erik R Barthel, Ignacio B Martini, and Benjamin J Schwartz. *How does the solvent control electron transfer? Experimental and theoretical studies of the simplest charge transfer reaction*. 2001.

[14] Erik R Barthel, Ignacio B Martini, and Benjamin J Schwartz. "How does the solvent control electron transfer? Experimental and theoretical studies of the simplest charge transfer reaction". In: *J. Phys. Chem. B* 105.49 (2001), pp. 12230–12241.

[15] Axel D Becke. "Density-functional thermochemistry. III. The role of exact exchange". In: *The Journal of chemical physics* 98.7 (1993), pp. 5648–5652.

[16] Michael J Bedard-Hearn, Ross E Larsen, and Benjamin J Schwartz. "The role of solvent structure in the absorption spectrum of solvated electrons: Mixed quantum/classical simulations in tetrahydrofuran". In: *The Journal of chemical physics* 122.13 (2005).

[17] Michal Ben-Nun and Todd J Martínez. "Ab initio quantum molecular dynamics". In: *Advances in chemical physics* 121 (2002), pp. 439–512.

[18] M Bixon and Joshua Jortner. "Electron transfer: from isolated molecules to biomolecules". In: *Advances in Chemical Physics*. Vol. 106. Wiley Online Library, 1999, pp. 35–202.

[19] M Bixon and Joshua Jortner. "Non-Arrhenius temperature dependence of electron-transfer rates". In: *The Journal of Physical Chemistry* 95.5 (1991), pp. 1941–1944.

[20] Max Born and Kun Huang. *Dynamical theory of crystal lattices*. Oxford university press, 1996.

[21] Raffaele Borrelli, Mariangela Di Donato, and Andrea Peluso. "Role of intramolecular vibrations in long-range electron transfer between pheophytin and ubiquinone in bacterial photosynthetic reaction centers". In: *Biophysical journal* 89.2 (2005), pp. 830–841.

[22] Raffaele Borrelli and Andrea Peluso. "Elementary electron transfer reactions: from basic concepts to recent computational advances". In: *Wiley Interdisciplinary Reviews: Computational Molecular Science* 3.6 (2013), pp. 542–559.

[23] Raffaele Borrelli and Andrea Peluso. "The temperature dependence of radiationless transition rates from ab initio computations". In: *Physical Chemistry Chemical Physics* 13.10 (2011), pp. 4420–4426.

[24] Arthur E Bragg and Benjamin J Schwartz. "The ultrafast charge-transfer-to-solvent dynamics of iodide in tetrahydrofuran. 1. Exploring the roles of solvent and solute electronic structure in condensed-phase charge-transfer

reactions". In: *The Journal of Physical Chemistry B* 112.2 (2008), pp. 483–494.

[25] Arthur E Bragg and Benjamin J Schwartz. "Ultrafast charge-transfer-to-solvent dynamics of iodide in tetrahydrofuran. 2. Photoinduced electron transfer to counterions in solution". In: *The Journal of Physical Chemistry A* 112.16 (2008), pp. 3530–3543.

[26] Hugo Bronstein et al. "The role of chemical design in the performance of organic semiconductors". In: *Nature Reviews Chemistry* 4.2 (2020), pp. 66–77.

[27] PD Burrow, JA Michejda, and KD Jordan. "Electron transmission study of the temporary negative ion states of selected benzenoid and conjugated aromatic hydrocarbons". In: *J. Chem. Phys.* 86.1 (1987), pp. 9–24.

[28] Ivo Cacelli and Giacomo Prampolini. "Parametrization and Validation of Intramolecular Force Fields Derived from DFT Calculations". In: *J. Chem. Theory Comput.* 3 (2007), pp. 1803–1817. DOI: 10.1021/ct700113h.

[29] S Califano and JC Decius. *Vibrational States*. 1977.

[30] Amedeo Capobianco et al. "The Charge-Transfer Band of an Oxidized Watson-Crick Guanosine-Cytidine Complex". In: *Angewandte Chemie-German Edition* 121.50 (2009), p. 9690.

[31] Joseph J Cavaleri, Katherine Prater, and Robert M Bowman. "An investigation of the solvent dependence on

the ultrafast intersystem crossing kinetics of xanthone". In: *Chemical physics letters* 259.5-6 (1996), pp. 495–502.

[32] Jun Cheng et al. "Redox potentials and acidity constants from density functional theory based molecular dynamics". In: *Acc. Chem. Res.* 47.12 (2014), pp. 3522–3529.

[33] GL Closs et al. "Distance, stereoelectronic effects, and the Marcus inverted region in intramolecular electron transfer in organic radical anions". In: *The Journal of Physical Chemistry* 90.16 (1986), pp. 3673–3683.

[34] Martin CR Cockett et al. "Vibronic coupling in the ground cationic state of naphthalene: a laser threshold photoelectron [zero kinetic energy (ZEKE)-photoelectron] spectroscopic study". In: *The Journal of chemical physics* 98.10 (1993), pp. 7763–7772.

[35] Neil G Connelly and William E Geiger. "Chemical redox agents for organometallic chemistry". In: *Chem. Rev.* 96.2 (1996), pp. 877–910.

[36] Robert E Connors and William R Christian. "Origin of the unusual triplet-state properties of xanthones". In: *The Journal of Physical Chemistry* 86.9 (1982), pp. 1524–1528.

[37] Marcin Dampc et al. "Threshold photoelectron spectra of tetrahydrofuran over the energy range 9–29 eV". In: *Chemical Physics* 359.1-3 (2009), pp. 77–81.

[38] Juan Carlos Del Valle and Javier Catalán. "Kasha's rule: a reappraisal". In: *Physical Chemistry Chemical Physics* 21.19 (2019), pp. 10061–10069.

[39] RR Dogonadze, A_M Kuznetsov, and MA Vorotyntsev. "On the theory of nonradiative transitions in polar media I. Processes without "mixing" of quantum and classical degrees of freedom". In: *physica status solidi (b)* 54.1 (1972), pp. 125–134.

[40] David Dunlop et al. "Excited-state (anti) aromaticity explains why azulene disobeys Kasha's rule". In: *Journal of the American Chemical Society* 145.39 (2023), pp. 21569–21575.

[41] MA El-Sayed. "Spin—orbit coupling and the radiationless processes in nitrogen heterocyclics". In: *The Journal of Chemical Physics* 38.12 (1963), pp. 2834–2838.

[42] Stefano Falletta, Julia Wiktor, and Alfredo Pasquarello. "Finite-size corrections of defect energy levels involving ionic polarization". In: *Phys. Rev. B* 102 (4 2020), p. 041115. DOI: 10.1103/PhysRevB.102.041115. URL: https://link.aps.org/doi/10.1103/PhysRevB.102.041115.

[43] Richard Phillips Feynman. "Forces in molecules". In: *Physical review* 56.4 (1939), p. 340.

[44] GR Fleming, JL Martin, and J Breton. "Rates of primary electron transfer in photosynthetic reaction centres and their mechanistic implications". In: *Nature* 333.6169 (1988), pp. 190–192.

[45] S. Fratini et al. "A Map of High-Mobility Molecular Semiconductors". In: *Nat. Mater.* 16.10 (2017), pp. 998–1002. ISSN: 14764660. DOI: 10.1038/nmat4970.

[46] Daan Frenkel and Berend Smit. *Understanding Molecular Simulation: From Algorithms to Applications*. Academic Press, 2002.

[47] Christoph Freysoldt, Jörg Neugebauer, and Chris G Van de Walle. "Fully ab initio finite-size corrections for charged-defect supercell calculations". In: *Physical review letters* 102.1 (2009), p. 016402.

[48] M. J. Frisch et al. *Gaussian~16 Revision C.01*. Gaussian Inc. Wallingford CT. 2016.

[49] Jiehao Fu et al. "Rational molecular and device design enables organic solar cells approaching 20% efficiency". In: *Nature communications* 15.1 (2024), p. 1830.

[50] H_J Geise, WJ Adams, and Lawrence S Bartell. "Electron diffraction study of gaseous tetrahydrofuran". In: *Tetrahedron* 25.15 (1969), pp. 3045–3052.

[51] Samuele Giannini et al. "JOYCE3. 0: A General Protocol for the Specific Parametrization of Accurate Intramolecular Quantum Mechanically Derived Force Fields". In: *J. Chem. Theory Comput.* 21.6 (2025), pp. 3156–3175.

[52] Klaus Gustav and Michael Storch. "Non-radiative deactivation of molecules. II. Theoretical study of the internal conversion rates in azulene". In: *International journal of quantum chemistry* 38.1 (1990), pp. 1–10.

[53] Balazs Hajgató et al. "A benchmark theoretical study of the electron affinities of benzene and linear acenes". In: *J. Chem. Phys.* 129.8 (2008).

[54] B Heinz et al. "On the unusual fluorescence properties of xanthone in water". In: *Physical Chemistry Chemical Physics* 8.29 (2006), pp. 3432–3439.

[55] Hans Hellmann. "Einführung in die Quantenchemie". In: *Hans Hellmann: Einführung in die Quantenchemie: Mit biografischen Notizen von Hans Hellmann jr.* Springer, 1937, pp. 19–376.

[56] Pierre Hohenberg and Walter Kohn. "Inhomogeneous electron gas". In: *Physical review* 136.3B (1964), B864.

[57] Richard A Holroyd and John R Miller. "Rate versus free energy change for attaching highly mobile electrons to molecules in nonpolar liquids". In: *The Journal of Physical Chemistry B* 123.43 (2019), pp. 9206–9211.

[58] JJ Hopfield. "Electron transfer between biological molecules by thermally activated tunneling". In: *Proceedings of the National Academy of Sciences* 71.9 (1974), pp. 3640–3644.

[59] GR Hunt, EF McCoy, and IG Ross. "Excited states of aromatic hydrocarbons: Pathways of internal conversion". In: *Australian Journal of Chemistry* 15.4 (1962), pp. 591–604.

[60] Graham R Hunt and Ian G Ross. "Spectrum of azulene: Part II. The 7000-A and 3500-A absorption systems". In: *Journal of Molecular Spectroscopy* 9 (1962), pp. 50–78.

[61] Dan Huppert, Joshua Jortner, and PM Rentzepis. "Azulene Revisited: Picosecond Decay of the S1 State in the Gas Phase and in Solution". In: *Israel Journal of Chemistry* 16.4 (1977), pp. 277–282.

[62] Jenn Kang Hwang and Arieh Warshel. "Microscopic examination of free-energy relationships for electron transfer in polar solvents". In: *Journal of the American Chemical Society* 109.3 (1987), pp. 715–720.

[63] The MathWorks Inc. *MATLAB version: 21.1.0.2628055 (R2024a)*. Natick, Massachusetts, United States, 2022. URL: https://www.mathworks.com.

[64] Takao Itoh. "Fluorescence and phosphorescence from higher excited states of organic molecules". In: *Chemical reviews* 112.8 (2012), pp. 4541–4568.

[65] H. H. Jaffe and Albert L. Miller. "The fates of electronic excitation energy". In: *Journal of Chemical Education* 43.9 (1966), p. 469. DOI: 10.1021/ed043p469. eprint: https://doi.org/10.1021/ed043p469. URL: https://doi.org/10.1021/ed043p469.

[66] H. Jaffé and M. Orchin. "Theory and Appplications of Ultraviolet Spectroscopy". In: (1962).

[67] Chienyu F Jen and Arieh Warshel. "Microscopic based density matrix treatments of electron-transfer reactions in condensed phases". In: *The Journal of Physical Chemistry A* 103.51 (1999), pp. 11378–11386.

[68] Joshua Jortner and Mordechai Bixon. "Intramolecular vibrational excitations accompanying solvent-controlled electron transfer reactions". In: *The Journal of chemical physics* 88.1 (1988), pp. 167–170.

[69] Neil R Kestner, Jean Logan, and Joshua Jortner. "Thermal electron transfer reactions in polar solvents". In: *The Journal of Physical Chemistry* 78.21 (1974), pp. 2148–2166.

[70] Gregory King and Arieh Warshel. "Investigation of the free energy functions for electron transfer reactions". In: *The Journal of Chemical Physics* 93.12 (1990), pp. 8682–8692.

[71] Christine Kirmaier, Dewey Holten, and William W. Parson. "Temperature and detection-wavelength dependence of the picosecond electron-transfer kinetics measured in Rhodopseudomonas sphaeroides reaction centers. Resolution of new spectral and kinetic components in the primary charge-separation process". In: *Biochimica et Biophysica Acta (BBA)-Bioenergetics* 810.1 (1985), pp. 33–48.

[72] D Kleinfeld, MY Okamura, and George Feher. "Electron-transfer kinetics in photosynthetic reaction centers cooled to cryogenic temperatures in the charge-separated state: evidence for light-induced structural changes". In: *Biochemistry* 23.24 (1984), pp. 5780–5786.

[73] Joseph W Knight et al. "Accurate ionization potentials and electron affinities of acceptor molecules III: a benchmark of GW methods". In: *J. Chem. Theory Comput.* 12.2 (2016), pp. 615–626.

[74] Hannu-Pekka Komsa, Tapio T Rantala, and Alfredo Pasquarello. "Finite-size supercell correction schemes for charged defect calculations". In: *Physical Review B—Condensed Matter and Materials Physics* 86.4 (2012), p. 045112.

[75] H Köuppel, Wolfgang Domcke, and Lorenz S Cederbaum. "Multimode molecular dynamics beyond the Born-Oppenheimer approximation". In: *Advances in chemical physics* (1984), pp. 59–246.

[76] Ryogo Kubo and Yutaka Toyozawa. "Application of the method of generating function to radiative and non-radiative transitions of a trapped electron in a crystal". In: *Progress of Theoretical Physics* 13.2 (1955), pp. 160–182.

[77] Takayoshi Kubo et al. "Suppressing molecular vibrations in organic semiconductors by inducing strain". In: *Nat. Commun.* 7.1 (2016), p. 11156. DOI: 10.1038/ncomms11156. URL: https://doi.org/10.1038%2Fncomms11156.

[78] Lev Davidovich Landau and Evgenii Mikhailovich Lifshitz. *Quantum mechanics: Non-Relativistic Theory*. Vol. 3. Elsevier, 2013.

[79] Alessandro Landi, Amedeo Capobianco, and Andrea Peluso. "Coherent Effects in Charge Transport in Molecular Wires: Toward a Unifying Picture of Long-Range

Hole Transfer in DNA". In: *The Journal of Physical Chemistry Letters* 11.18 (2020), pp. 7769–7775.

[80] Alessandro Landi and Daniele Padula. "Multiple Charge Separation Pathways in New-Generation Non-Fullerene Acceptors: a Computational Study". In: *J. Mater. Chem. A* 9.44 (2021), pp. 24849–24856. DOI: 10.1039/d1ta05664f.

[81] Alessandro Landi, Daniele Padula, and Andrea Peluso. "Fast Nonradiative Decay Paths in Organic Solar Cells: Implications for Designing More Efficient Photovoltaic Systems". In: *ACS Applied Energy Materials* 7.2 (2023), pp. 707–714.

[82] Alessandro Landi, Daniele Padula, and Andrea Peluso. "Fast Nonradiative Decay Paths in Organic Solar Cells: Implications for Designing More Efficient Photovoltaic Systems". In: *ACS Appl. Energy Mater.* 7.2 (2024), pp. 707–714. DOI: 10.1021/acsaem.3c02790. eprint: https://doi.org/10.1021/acsaem.3c02790. URL: https://doi.org/10.1021/acsaem.3c02790.

[83] Alessandro Landi et al. "Efficient charge dissociation of triplet excitons in bulk heterojunction solar cells". In: *ACS Applied Energy Materials* 5.9 (2022), pp. 10815–10824.

[84] Alessandro Landi et al. "Simulation of polymeric mixed ionic and electronic conductors with a combined classical and quantum mechanical model". In: *J. Mater. Chem. C* 11.24 (2023), pp. 8062–8073. DOI: 10.1039/d2tc05103f. URL: https://doi.org/10.1039%2Fd2tc05103f.

[85] Alessandro Landi et al. "The rates of non-adiabatic processes in large molecular systems: Toward an effective full-dimensional quantum mechanical approach". In: *The Journal of Chemical Physics* 160.17 (2024).

[86] Alessandro Landi et al. "Toward Efficient Modeling of Nonradiative Decay in Extended INVEST: Overcoming Computational Challenges in Quantum Dynamics Simulations". In: *J. Phys. Chem. Lett.* 15.44 (Oct. 2024), 11042–11050. ISSN: 1948-7185. DOI: 10.1021/acs.jpclett.4c02713. URL: http://dx.doi.org/10.1021/acs.jpclett.4c02713.

[87] Alessandro Landi et al. "Transient and enduring electronic resonances drive coherent long distance charge transport in molecular wires". In: *The Journal of Physical Chemistry Letters* 10.8 (2019), pp. 1845–1851.

[88] Melvin Lax. "The Franck-Condon principle and its application to crystals". In: *The Journal of chemical physics* 20.11 (1952), pp. 1752–1760.

[89] Chengteh Lee, Weitao Yang, and Robert G Parr. "Development of the Colle-Salvetti correlation-energy formula into a functional of the electron density". In: *Physical review B* 37.2 (1988), p. 785.

[90] Anna Leo and Andrea Peluso. "Electron transfer rates in polar and non-polar environments: a generalization of Marcus' theory to include an effective treatment of tunneling effects". In: *The Journal of Physical Chemistry Letters* 13.39 (2022), pp. 9148–9155.

[91] Anna Leo et al. "Electron Transfer Rates in Solution: Toward a Predictive First Principle Approach". In: *Chemistry* 5.1 (2023), pp. 97–105.

[92] VG Levich. "Present state of the theory of oxidation-reduction in solution (bulk and electrode reactions)". In: *Adv. Electrochem. Electrochem. Eng* 4 (1966), pp. 249–371.

[93] Benjamin G Levine et al. "Conical intersections and double excitations in time-dependent density functional theory". In: *Molecular Physics* 104.5-7 (2006), pp. 1039–1051.

[94] N. Liang, J.R. Miller, and G.L. Closs. "Correlating temperature dependence to free-energy dependence of intramolecular long-range electron transfers". In: *Journal of the American Chemical Society* 111.23 (1989), pp. 8740–8741.

[95] Nong Liang, John R Miller, and Gerhard L Closs. "Temperature-independent long-range electron transfer reactions in the Marcus inverted region". In: *Journal of the American Chemical Society* 112.13 (1990), pp. 5353–5354.

[96] Kai Liu et al. "Advances in flexible organic field-effect transistors and their applications for flexible electronics". In: *npj Flex. Electron.* 6 (Jan. 2022), p. 1. DOI: 10.1038/s41528-022-00133-3. URL: https://doi.org/10.1038%2Fs41528-022-00133-3.

[97] Kai Liu et al. "Advances in flexible organic field-effect transistors and their applications for flexible electronics". In: *npj Flex. Electron.* 6.1 (Jan. 2022). ISSN: 2397-4621. DOI:

10.1038/s41528-022-00133-3. URL: http://dx.doi.org/10.1038/s41528-022-00133-3.

[98] Svetlana A Lyapustina et al. "Solvent-induced stabilization of the naphthalene anion by water molecules: A negative cluster ion photoelectron spectroscopic study". In: *J. Chem. Phys.* 112.15 (2000), pp. 6643–6648.

[99] B. H. Mahan. "Microscopic Reversibility and Detailed Balance". In: *J. Chem. Educ.* 52 (1975), pp. 299–302.

[100] Irena Majerz. "Weak interactions in furan dimers". In: *Journal of Computer-Aided Molecular Design* 32.11 (2018), pp. 1247–1258.

[101] R. Maksimenka et al. "Femtosecond Dynamics of Electron Transfer in a Neutral Organic Mixed-Valence Compound". In: *J. Chem. Phys.* 347 (2008), pp. 436–445.

[102] RA Marcus. "Nonadiabatic processes involving quantum-like and classical-like coordinates with applications to nonadiabatic electron transfers". In: *The Journal of chemical physics* 81.10 (1984), pp. 4494–4500.

[103] Rudolph A Marcus. "Electron transfer reactions in chemistry: theory and experiment (Nobel lecture)". In: *Angewandte Chemie International Edition in English* 32.8 (1993), pp. 1111–1121.

[104] Rudolph A Marcus. "Exchange reactions and electron transfer reactions including isotopic exchange. Theory of oxidation-reduction reactions involving electron transfer. Part 4.—A statistical-mechanical basis for treating

contributions from solvent, ligands, and inert salt". In: *Discussions of the Faraday Society* 29 (1960), pp. 21–31.

[105] Rudolph A Marcus. "On the theory of oxidation-reduction reactions involving electron transfer. I". In: *The Journal of chemical physics* 24.5 (1956), pp. 966–978.

[106] Christel M Marian. "Understanding and controlling intersystem crossing in molecules". In: *Annual review of physical chemistry* 72.1 (2021), pp. 617–640.

[107] Eva Åkesson, Gilbert C Walker, and Paul F Barbara. "Dynamic solvent effects on electron transfer rates in the inverted regime: Ultrafast studies on the betaines". In: *The Journal of chemical physics* 95.6 (1991), pp. 4188–4194.

[108] Donald J Metz and Althea Glines. "Density, viscosity, and dielectric constant of tetrahydrofuran between-78 and 30. degree." In: *The Journal of Physical Chemistry* 71.4 (1967), pp. 1158–1158.

[109] Hans-Dieter Meyer, Fabien Gatti, and Graham A Worth. *Multidimensional quantum dynamics: MCTDH theory and applications*. John Wiley & Sons, 2009.

[110] John R Miller, James V Beitz, and R Kurt Huddleston. "Effect of free energy on rates of electron transfer between molecules". In: *Journal of the American Chemical Society* 106.18 (1984), pp. 5057–5068.

[111] John R Miller, LT Calcaterra, and GL Closs. "Intramolecular long-distance electron transfer in radical anions.

The effects of free energy and solvent on the reaction rates". In: *J. Am. Chem. Soc.* 106.10 (1984), pp. 3047–3049.

[112] Afshan Mohajeri and Maryam Farmani. "Toward more efficient organic semiconductors: The relationship between morphology, charge transport, and photophysical properties". In: *ACS Applied Electronic Materials* 4.1 (2022), pp. 246–258.

[113] Tatiana Nemirovich et al. "Stability and Reactivity of Aromatic Radical Anions in Solution with Relevance to Birch Reduction". In: *Journal of the American Chemical Society* 146.12 (2024), pp. 8043–8057.

[114] Yingli Niu et al. "Theory of excited state decays and optical spectra: application to polyatomic molecules". In: *The Journal of Physical Chemistry A* 114.30 (2010), pp. 7817–7831.

[115] Timothy F. O'Connor et al. "Wearable organic solar cells with high cyclic bending stability: Materials selection criteria". In: *Sol. Energy Mater. Sol. Cells* 144 (2016), pp. 438–444. DOI: 10.1016/j.solmat.2015.09.049. URL: https://doi.org/10.1016%2Fj.solmat.2015.09.049.

[116] Oksana Ostroverkhova. "Organic Optoelectronic Materials: Mechanisms and Applications". In: *Chem. Rev.* 116.22 (2016), 13279–13412. ISSN: 1520-6890. DOI: 10.1021/acs.chemrev.6b00127. URL: http://dx.doi.org/10.1021/acs.chemrev.6b00127.

[117] Daniele Padula, Alessandro Landi, and Giacomo Prampolini. "Assessing alkyl side chain effects on electron transport properties of Y6-derived non-fullerene acceptors". In: *Energy Adv.* 2.8 (2023), pp. 1215–1224. DOI: 10.1039/d3ya00149k. URL: https://doi.org/10.1039%2Fd3ya00149k.

[118] Daniele Padula et al. "Towards a fast machine-learning-assisted prediction of the mechanoelectric response in organic crystals". In: *J. Mater. Chem. C* 11.36 (2023), pp. 12297–12306. DOI: 10.1039/d3tc02235h. URL: https://doi.org/10.1039%2Fd3tc02235h.

[119] Sung Man Park et al. "Conformational structures of the tetrahydrofuran cation determined using one-photon mass-analyzed threshold ionization spectroscopy". In: *Phys. Chem. Chem. Phys.* 19.45 (2017), pp. 30362–30369.

[120] William W Parson. "Effects of free energy and solvent on rates of intramolecular electron transfer in organic radical anions". In: *The Journal of Physical Chemistry A* 121.38 (2017), pp. 7297–7306.

[121] William W Parson and Arieh Warshel. "A density-matrix model of photosynthetic electron transfer with microscopically estimated vibrational relaxation times". In: *Chemical physics* 296.2-3 (2004), pp. 201–216.

[122] Bryan D. Paulsen et al. "Organic Mixed Ionic-Electronic Conductors". In: *Nat. Mater.* 19 (2020), pp. 13–26. ISSN: 14764660. DOI: 10.1038/s41563-019-0435-z. URL: https://doi.org/10.1038/s41563-019-0435-z.

[123] Andrea Peluso, Raffaele Borrelli, and Amedeo Capobianco. "Photoelectron Spectrum of Ammonia, a Test Case for the Calculation of Franck- Condon Factors in Molecules Undergoing Large Geometrical Displacements upon Photoionization". In: *The Journal of Physical Chemistry A* 113.52 (2009), pp. 14831–14837.

[124] John P. Perdew, Matthias Ernzerhof, and Kieron Burke. "Rationale for Mixing Exact Exchange with Density Functional Approximations". In: *J. Chem. Phys.* 105.22 (1996), pp. 9982–9985. DOI: http://dx.doi.org/10.1063/1.472933.

[125] Henry J Pownall and J Robert Huber. "Absorption and emission spectra of aromatic ketones and their medium dependence. Excited states of xanthone". In: *Journal of the American Chemical Society* 93.24 (1971), pp. 6429–6436.

[126] E. B. Priestley and A. Haug. "Phosphorescence Spectrum of Pure Crystalline Naphthalene". In: *The Journal of Chemical Physics* 49.2 (July 1968), pp. 622–629. ISSN: 0021-9606. DOI: 10.1063/1.1670118. eprint: https://pubs.aip.org/aip/jcp/article-pdf/49/2/622/18858028/622_1_online.pdf. URL: https://doi.org/10.1063/1.1670118.

[127] Antonio Prlj et al. "Semiclassical approach to photophysics beyond kasha's rule and vibronic spectroscopy beyond the condon approximation. The case of azulene". In: *Journal of chemical theory and computation* 16.4 (2020), pp. 2617–2626.

[128] JW Rabalais et al. "Analysis of vibrational structure and Jahn-Teller effects in the electron spectrum of ammonia". In: *The Journal of Chemical Physics* 58.8 (1973), pp. 3370–3372.

[129] Vidisha Rai-Constapel, Mihajlo Etinski, and Christel M Marian. "Photophysics of xanthone: a quantum chemical perusal". In: *The Journal of Physical Chemistry A* 117.19 (2013), pp. 3935–3944.

[130] Vidisha Rai-Constapel, Susanne Salzmann, and Christel M Marian. "Isolated and solvated thioxanthone: a photophysical study". In: *The Journal of Physical Chemistry A* 115.31 (2011), pp. 8589–8596.

[131] Víctor M Rayón and Jose A Sordo. "Pseudorotation motion in tetrahydrofuran: An ab initio study". In: *J. Chem. Phys.* 122.20 (2005).

[132] PM Rentzepis. "Emission from the lowest singlet and triplet states of azulene". In: *Chemical Physics Letters* 3.9 (1969), pp. 717–720.

[133] Julien Robert-Paganin et al. "Force generation by myosin motors: a structural perspective". In: *Chemical reviews* 120.1 (2019), pp. 5–35.

[134] Riccardo Sabatini, Tommaso Gorni, and Stefano de Gironcoli. "Nonlocal van der Waals Density Functional Made Simple and Efficient". In: *Phys. Rev. B* 87 (4 2013), p. 041108. DOI: 10.1103/PhysRevB.87.041108.

[135] Amin Salehi et al. "Recent advances in OLED optical design". In: *Advanced Functional Materials* 29.15 (2019), p. 1808803.

[136] Fabrizio Santoro et al. "Effective method for the computation of optical spectra of large molecules at finite temperature including the Duschinsky and Herzberg–Teller effect: The Qx band of porphyrin as a case study". In: *The Journal of chemical physics* 128.22 (2008).

[137] JC Scaiano. "Solvent effects in the photochemistry of xanthone". In: *Journal of the American Chemical Society* 102.26 (1980), pp. 7747–7753.

[138] Craig C Schenck et al. "Temperature dependence of electron transfer between bacteriopheophytin and ubiquinone in protonated and deuterated reaction centers of Rhodopseudomonas sphaeroides". In: *Biophysical Journal* 36.3 (1981), pp. 479–489.

[139] J Schiedt et al. "Microsolvation of similar-sized aromatic molecules: Photoelectron spectroscopy of bithiophene–, azulene–, and naphthalene–water anion clusters". In: *J. Chem. Phys.* 113.21 (2000), pp. 9470–9478.

[140] Yihan Shao et al. "Advances in molecular quantum chemistry contained in the Q-Chem 4 program package". In: *Molecular Physics* 113.2 (2015), pp. 184–215.

[141] Sahar Sharifzadeh et al. "Quantitative molecular orbital energies within a G 0 W 0 approximation". In: *Eur. Phys. J. B* 85 (2012), pp. 1–5.

[142] Zhigang Shuai et al. "Applying Marcus theory to describe the carrier transports in organic semiconductors: Limitations and beyond". In: *The Journal of Chemical Physics* 153.8 (2020).

[143] Zhigang Shuai et al. "From charge transport parameters to charge mobility in organic semiconductors through multiscale simulation". In: *Chemical Society Reviews* 43.8 (2014), pp. 2662–2679.

[144] Jerome W Sidman and Donald S McClure. "Electronic and vibrational states of azulene". In: *The Journal of Chemical Physics* 24.4 (1956), pp. 757–763.

[145] W Siebrand. "Radiationless transitions in polyatomic molecules. I. Calculation of Franck—Condon factors". In: *The Journal of Chemical Physics* 46.2 (1967), pp. 440–447.

[146] J. D. Simon. "Time-Resolved Studies of Solvation in Polar Media". In: *Res. Chem. Acc.* 21 (1988), pp. 128–134.

[147] Petr Slavicek et al. "Ionization energies of aqueous nucleic acids: Photoelectron spectroscopy of pyrimidine nucleosides and ab initio calculations". In: *Journal of the American Chemical Society* 131.18 (2009), pp. 6460–6467.

[148] Henry J Snaith. "Perovskites: the emergence of a new era for low-cost, high-efficiency solar cells". In: *The journal of physical chemistry letters* 4.21 (2013), pp. 3623–3630.

[149] Ebru Kondolot Solak and Erdal Irmak. "Advances in organic photovoltaic cells: a comprehensive review of materials, technologies, and performance". In: *RSC Adv.* 13.18 (2023), 12244–12269. ISSN: 2046-2069. DOI: 10.1039/d3ra01454a. URL: http://dx.doi.org/10.1039/D3RA01454A.

[150] Jae Kyu Song et al. "Photoelectron spectroscopy of naphthalene cluster anions". In: *J. Chem. Phys.* 116.11 (2002), pp. 4477–4481.

[151] Massimo Sparpaglione and Shaul Mukamel. "Adiabatic vs. nonadiabatic electron transfer and longitudinal solvent dielectric relaxation: beyond the Debye model". In: *Journal of Physical Chemistry* 91.15 (1987), pp. 3938–3943.

[152] Philipp Sulzer et al. "Dissociative electron attachment to furan, tetrahydrofuran, and fructose". In: *The Journal of chemical physics* 125.4 (2006).

[153] Hitoshi Sumi and RA Marcus. "Dynamical effects in electron transfer reactions". In: *The Journal of chemical physics* 84.9 (1986), pp. 4894–4914.

[154] Norman Sutin. "Electron transfer reactions in solution: A historical perspective". In: *Advances in Chemical Physics: Electron Transfer—from Isolated Molecules to Biomolecules. Part 1* 106 (1999), pp. 7–33.

[155] Christopher Sutton, Chad Risko, and Jean-Luc Brédas. "Noncovalent Intermolecular Interactions in Organic Electronic Materials: Implications for the Molecular Packing vs Electronic Properties of Acenes". In: *Chemistry*

of Materials 28.1 (2016), pp. 3–16. DOI: 10.1021/acs.chemmater.5b03266. eprint: https://doi.org/10.1021/acs.chemmater.5b03266. URL: https://doi.org/10.1021/acs.chemmater.5b03266.

[156] Mira Todorova and Jörg Neugebauer. "Extending the concept of defect chemistry from semiconductor physics to electrochemistry". In: *Physical Review Applied* 1.1 (2014), p. 014001.

[157] Jacopo Tomasi, Benedetta Mennucci, and Roberto Cammi. "Quantum mechanical continuum solvation models". In: *Chemical reviews* 105.8 (2005), pp. 2999–3094.

[158] John C Tully. "Molecular dynamics with electronic transitions". In: *The Journal of Chemical Physics* 93.2 (1990), pp. 1061–1071.

[159] NJ Turro et al. "The effect of wavelength on organic photoreactions in solution. Reactions from upper excited states". In: *Chemical Reviews* 78.2 (1978), pp. 125–145.

[160] Michiel J Van Setten et al. "GW 100: Benchmarking G_0W_0 for molecular systems". In: *J. Chem. Theory Comput.* 11.12 (2015), pp. 5665–5687.

[161] Joost VandeVondele et al. "Quickstep: Fast and Accurate Density Functional Calculations Using a Mixed Gaussian and Plane Waves Approach". In: *Comput. Phys. Commun.* 167.2 (2005), pp. 103 –128. DOI: 10.1016/j.cpc.2004.12.014.

[162] Koen Veys and Daniel Escudero. "Computational protocol to predict anti-Kasha emissions: The case of Azulene derivatives". In: *The Journal of Physical Chemistry A* 124.36 (2020), pp. 7228–7237.

[163] Gorthi Viswanath and Michael Kasha. "Confirmation of the anomalous fluorescence of azulene". In: *The Journal of Chemical Physics* 24.3 (1956), pp. 574–577.

[164] Oleg A. Vydrov and Troy Van Voorhis. "Nonlocal van der Waals Density Functional: The Simpler the Better". In: *J. Chem. Phys.* 133.24 (2010), p. 244103. DOI: http://dx.doi.org/10.1063/1.3521275.

[165] Chris G Van de Walle and Jörg Neugebauer. "First-principles calculations for defects and impurities: Applications to III-nitrides". In: *Journal of applied physics* 95.8 (2004), pp. 3851–3879.

[166] Xue-Bin Wang, Hin-Koon Woo, and Lai-Sheng Wang. "Vibrational cooling in a cold ion trap: vibrationally resolved photoelectron spectroscopy of cold C60- anions". In: *The Journal of chemical physics* 123.5 (2005).

[167] Arieh Warshel. "Role of the chlorophyll dimer in bacterial photosynthesis". In: *Proceedings of the National Academy of Sciences* 77.6 (1980), pp. 3105–3109.

[168] Morteza M Waskasi et al. "Marcus bell-shaped electron transfer kinetics observed in an Arrhenius plot". In: *Journal of the American Chemical Society* 138.29 (2016), pp. 9251–9257.

[169] Devon R Widmer and Benjamin J Schwartz. "Solvents can control solute molecular identity". In: *Nat. Chem.* 10.9 (2018), pp. 910–916.

[170] Dominik Wöll et al. "On the mechanism of intramolecular sensitization of photocleavage of the 2-(2-nitrophenyl) propoxycarbonyl (NPPOC) protecting group". In: *Journal of the American Chemical Society* 129.40 (2007), pp. 12148–12158.

[171] Takeshi Yanai, David P Tew, and Nicholas C Handy. "A new hybrid exchange–correlation functional using the Coulomb-attenuating method (CAM-B3LYP)". In: *Chemical physics letters* 393.1-3 (2004), pp. 51–57.

[172] Chou-Hsun Yang et al. "Non-Negligible Outer-Shell Reorganization Energy for Charge Transfer in Nonpolar Systems". In: *Journal of Chemical Theory and Computation* 20.16 (2024), pp. 6981–6991.

[173] Huifeng Yao and Jianhui Hou. "Recent advances in single-junction organic solar cells". In: *Angewandte Chemie International Edition* 61.37 (2022), e202209021.

[174] Kunta Yoshikawa et al. "Silicon Heterojunction Solar Cell with Interdigitated Back Contacts for a Photoconversion Efficiency over 26%". In: *Nat. Ener.* 2 (2017), p. 17032. DOI: 10.1038/nenergy.2017.32.

[175] Saravanan Yuvaraja et al. "Organic field-effect transistor-based flexible sensors". In: *Chemical Society Reviews* 49.11 (2020), pp. 3423–3460.

[176] Da-Wei Zhang, Meng Li, and Chuan-Feng Chen. "Recent advances in circularly polarized electroluminescence based on organic light-emitting diodes". In: *Chemical Society Reviews* 49.5 (2020), pp. 1331–1343.

[177] Leonid D. Zusman. "Outer-Sphere Electron Transfer in Polar Solvents". In: *Chemical Physics* 49.2 (1980), pp. 295–304.